Development of Redox Organics for Aqueous Flow Batteries

HARVARD UNIVERSITY

Graduate School of Arts and Sciences

DISSERTATION ACCEPTANCE CERTIFICATE

The undersigned, appointed by the

Harvard John A. Paulson School of Engineering and Applied Sciences
have examined a dissertation entitled:

"Development of Redox Organics for Aqueous Flow Batteries"

presented by: Min Wu

Signature _____
Typed name: Professor R. Gordon

Signature _____
Typed name: Professor M. Aziz

Signature _____
Typed name: Professor X. Li

April 29, 2021

Development of Redox Organics for Aqueous Flow Batteries

A dissertation presented

by

Min Wu

To

The Department of Engineering & Applied Science

in partial fulfillment of the requirements

for the degree of

Doctor of Philosophy

in the subject of

Engineering Science

Harvard University

Cambridge, Massachusetts

April 2021

Development of Redox Organics for Aqueous Flow Batteries

Abstract

The cost of solar and wind electricity has dropped so precipitously that the main barrier to their widespread adoption is their intrinsic intermittency. Aqueous organic redox flow batteries (AORFBs) provide a potentially cost-effective energy storage option to this end. However, many challenges remain in advancing AORFBs, particularly the synthetic cost and long-term stability of redox-active organic molecules.

Starting from inexpensive precursor, we developed a new synthetic route for extremely stable anthraquinone negative electrolyte (negolyte) active species. Furthermore, we demonstrated that high pH suppresses the decomposition of anthraquinone negolyte, leading to a capacity fade rate of 0.7%/year, representing one of the lowest capacity fade rates, in the absence of rebalancing techniques, of any flow battery ever published – organic or inorganic. Additionally, we reported an in-situ electrochemical oxidation method to decrease the synthetic cost.

To further address the cost challenge, we developed a one-pot, green, and scalable approach to synthesize a highly water-soluble and potentially low-cost anthraquinone. By a simple functionalization, the volumetric capacity and cycle life of this anthraquinone improved more than one order of magnitude. Additionally, simulation regarding state of charge, cut-off voltage, and cut-off current density provides guidance on how to measure

the capacity fade rate more accurately.

In the final part, we developed the first anthraquinone negolyte species with a low capacity fade rate and a redox potential below -0.6 V vs. SHE at pH 14. The anthraquinone was synthesized from inexpensive precursors with a one-step *N*-alkylation method. Therefore, the mass production cost might be very low. The anthraquinone exhibited a high capacity fade rate of 2.6%/day at neutral pH, but the capacity fade rate decreased to 0.025%/day at pH 14, making it one of the most stable redox organic molecules ever reported. The substantial difference in anthraquinone cycling stability at different pH values was explained with thermodynamics.

Table of Contents

Chapter 1 Introduction 1

1.1 Renewable energy and energy storage 1

1.2 Aqueous Redox Flow Batteries (ARFB) 6

1.2.1 Performance Parameters for ARFB 8

1.2.2 Vanadium redox flow batteries (VRFB) 12

1.2.3 Iron-based flow batteries 14

1.2.4 Zinc based flow batteries 19

1.2.5 Sulfur based flow batteries 21

1.2.6 Aqueous Organic Redox Flow Batteries (AORFB) 23

Chaper 2. Decadal Lifetime Anthraquinone Redox Flow Batteries Enabled by High pH and the *In-situ* Electrochemical Synthesis 24

Authorship 24

2.1 Introduction 25

2.2 Experiment section: 28

2.2.1 Synthesis of 3,3'-(anthracene-diyl)bis(3-methylbutanoic acid) (DPivOHAC) 29

2.2.2 Synthesis of DPivOHAQ 30

2.2.3 4,4'-(9,10-dihydroanthracene-diyl)bis(4-oxobutanoic acid).. 30

2.2.4 Synthesis of 4,4'-(9,10-dihydroanthracene-diyl)dibutanoic acid (DBDHAC)

..... 31

2.2.5 Synthesis of DBAQ..... 33

2.3 Results and discussion 34

2.4 In situ electrosynthesis anthraquinone 57

2.5 Conclusions..... 67

Chapter 3. Potentially Low-Cost, Stable Anthraquinone Electrolytes for Aqueous Redox Flow Batteries 68

Authorship..... 68

3.1 Introduction..... 68

3.2 Experimental section..... 70

3.2.1 Synthesis of DCDHAQ..... 70

3.2.2 Synthesis of 1,4-dihydroxy-2-carboxymethyl-9,10-anthraquinone (1,4-CDHAQ) 72

3.2.3 Full cell measurements 73

3.3 Results and Discussion 74

3.3.1 Estimation of cost of electrolytes..... 88

3.3.2 1,4-CDHAQ results..... 89

3.4 Conclusions..... 91

Chapter 4 A Highly Stable Low Redox Potential Quinone for Aqueous Flow Batteries . 92

4.1 Introduction..... 92

4.2. Experimental section 94

4.2.1 Synthesis of 2,6-N-TSAQ 95

4.2.2 Synthesis of 2,6-O-DPSAQ 96

4.2.3 Synthesis of 2,6-DPSAQ 97

4.2.4 Full cell measurements 98

4.3 Results and Discussion 100

4.4 Conclusion 113

References 114

Table of Figures

Figure 1.1 Normalized energy demand and power supply from renewable energy in 500 hours…….3

Figure 1.2 Schematic of a redox flow battery…….7

Figure 1.3 Pourbaix diagram of iron in uncomplexed media……16

Figure 1.4 Pourbaix diagram of Zinc at 25 °C……...20

Figure 2.1 ^{1}H NMR spectrum of DPivOHAC……...29

Figure 2.2 ^{1}H NMR spectrum of DPivOHAQ……...30

Figure 2.3 ^{1}H NMR spectrum of DOBDHAC……...31

Figure 2.4 ^{1}H NMR spectrum of DBDHAC……..32

Figure 2.5 ^{1}H NMR spectrum of DBAQ……33

Figure 2.6 ^{1}H NMR spectra of thermo stability results……..37

Figure 2.7 DPivOHAQ synthesis and electrochemistry……38

Figure 2.8 DPivOHAQ reduction kinetics in RDE……39

Figure 2.9 Solubiltiy test of DPivOHAQ……...41

Figure 2.10 Polarization measurements of DPivOHAQ/ferrocyanide……...43

Figure 2.11 Cycling Performance of DPivOHAQ at pH 12 and 14……...45

Figure 2.12 Pourbaix diagram of anthraquinone, anthrahydroquinone, and anthrone……50

Figure 2.13 ^{1}H NMR spectra of the reduced and aerated DPivOHAQ……..52

Figure 2.14 LC-MS results from the reduced DPivOHAQ samples stored for 238

days……..…...53

Figure 2.15 DBAQ Synthesis and Electrochemistry…….55

Figure 2.16 RDE test for DBAQ……56

Figure 2.17 Preparation of DPivOHAQ and the corresponding flow battery……... 58

Figure 2.18 Comparison of DPivOHAQ synthetic methods……..59

Figure 2.19 Electrosynthesis and characterization of DPivOHAQ…….64

Figure 2.20 ^{1}H NMR spectra of DBDHAC, and DBAQ synthesized from chemical and in-situ electrochemical oxidation method……...66

Figure 3.1 ^{1}H NMR spectrum of DCDHAQ……...71

Figure 3.2 ^{1}H NMR spectrum of 1,4-CDHAQ……...72

Figure 3.3 Physical and electrochemical properties of 1,8-DHAQ and DCDHAQ…....77

Figure 3.4 Simulations for a cell with a capacity-limiting negolyte and a posolyte comprising one-electron redox molecules……..81

Figure 3.5 Electrochemistry of DCDHAQ…….83

Figure 3.6 ^{1}H NMR spectra of DCDHAQ before and after cycle……..87

Figure 3.7 Proposed electrochemical synthesis method for DCDHAQ…….88

Figure 3.8 Physical and electrochemical properties of 1,4-CDHAQ…….90

Figure 4.1 ^{1}H NMR spectrum of 2,6-N-TSAQ……..……95

Figure 4.2 LC-MS traces of the synthesized 2,6-N-TSAQ……..……..96

Figure 4.3 ^{1}H NMR spectrum of 2,6-O-DPSAQ…….97

Figure 4.4 ^{1}H NMR spectrum of 2,6-DPSAQ…….98

Figure 4.5 Synthetic routes for three different anthraquinones……101

Figure 4.6 Electrochemical and physical properties of three different anthraquinones 2,6-DPSAQ, 2,6-N-TSAQ, and 2,6-O-DPSAQ…….……102

Figure 4.7 Pourbaix diagram of 2,6-N-TSAQ……..104

Figure 4.8 Polarization experiments of 2,6-N-TSAQ……..106

Figure 4.9 Cell performance of 0.1 M 2,6-N-TSAQ/ferrocyanide cell, 2,6-N-TSAQ as the capacity limiting side……107

Figure 4.10 Energy efficiency and capacity contribution percentage versus cycle number of the 2,6-N-TSAQ/ferrocyanide cell in 1 M NaCl solution……109

Figure 4.11 ^{1}H NMR spectra of 2,6-N-TSAQ……..109

Figure 4.12 Thermodynamic analysis of anthraquinone disproportionation……112

Lists of Tables

Table 2.1 Lab-scale cost for raw materials of four stable anthraquinones……35

Table 2.2 Anodic, cathodic, and overall reactions for electrochemical oxidation…….62

Table 3.1 Properties of potentially low-cost redox-active organics for aqueous redox flow batteries……..85

Table 3.2 Electrochemical, physical properties, and estimated lab-scale cost comparison between 1,8-DHAQ, 2,6-DHAQ, DCDHAQ, 1,4-DHAQ…….91

Acknowledgement

I would first like to thank my Ph.D. advisor Professor Roy Gordon, whose expertise was invaluable in formulating the research questions and methodology. Roy is my role model, I learned not only science, but also social communication from him. He often brings cookies and desserts when we have group meeting, sends us flowers, and reminds us to enjoy the good weather. Roy is also very supportive in my professional development when I selected courses, attended conferences and applied for a postdoc. I cannot express my gratitude enough for Roy's supervision and support in the past 4 years.

I would also like to thank my secondary advisor Professor Michael Aziz for his extensive guidance and strong support. I learned a tremendous amount of electrochemistry from him. I admire his talent in naming scientific and daily activity. He improved my ability to pay attention to details which otherwise will plague me the rest of my life. Also, I want to especially thank Mike for his support for my career development. He sent lots of reference letter to my potential postdoc advisors with penitence and strong support.

I would also like to thank my thesis committee member Professor Xin Li, who served as a committee professor for both my qualify exam and dissertation defense exam. I learned a lot from his feedback and the discussion with him. I also like to thank Professor Cynthia Friend, who provided lots of valuable feedback during my qualify exam.

I would also like to thank Patricia McGarry, who is the lab administer in the Gordon group. Patricia provided lots of help for me. When we purchase order, she always approve

it very efficiently, saving us a lot of time. She also introduced me lots of volunteer opportunity to me, which enriched my life greatly. I would also like to thank Ann Greaney-Williams, who provided lots of help for my course plan and also kindly prepared the invitation letter for my parents to visit me.

Among all the brilliant researchers that I collaborated with, I want to especially thank Dr. Yan Jing from the Gordon group and Dr. Zhijiang Tang from the Aziz group for teach me organic synthesis and flow batteries assembly. I also want to thank my groupmates Dr. Yunlong Ji, Dr. Liuchuan Tong, Martin Jin, Emily Kerr, Daniel Pollack, Jinxu Gao, Dr. Tatsuhiro Tsukamoto, Xian Gong, Robert Gustafson, Eliza Spear, Dr. Meisam Bahari, Dr. Andrew Wong, Eric Fell, Dr. Diana de Porcellinis, Dr. Marc-Antoni Goulet, Jordan Sosa, Tommy George, Anton Graf for their valuable discussion and feedback for my research. Without their kindness and patience, I would not have been able to make such meaningful progress in my research.

Most importantly, I want to thank my wife Dr. Lingling Xia. We have been together since year 2011, a journey that is much longer than my Ph.D. Lingling provided fabulous emotional support, made my life much more enjoyable and memorable. She cheered me with any small achievement I made and encouraged me when I had tough days. I cannot be more grateful for her company in my life.

I want to thank my Mom and Dad for their always support. Pursing higher education in the US is a huge decision for me, I cannot be more grateful to have their support

whenever I needed them to help me through the tough days. It is comforting to know that they are always there and love is always there.

Min Wu

April 2021

Chapter 1 Introduction

1.1 Renewable energy and energy storage

Global climate has changed throughout history. The last 800,000 years have witnessed eight cycles of glacial advance and retreat, with the sudden end of the last ice age around 15,000 years ago.[1] Most of these climate changes are ascribed to tiny variations in Earth's orbit that change the amount of solar energy it receives. The current global warming trend, however, is mainly results from increased release of greenhouse gases from human activity since the first Industrial Revolution.[2] The greenhouse gases absorb and emit infrared energy cumulatively, increasing the average temperature of earth. Among the greenhouse gases, carbon dioxide (CO_2) is of particular importance because its high contribution to entrap thermal radiation in the atmospheric gas and the rapid growing rate in atmospheric concentration. The rapid growth of atmospheric CO_2 is attributed to anthropogenetic emissions from burning fossil fuels. In 2021, the Mauna Loa Observatory in Hawaii recorded an atmospheric CO_2 concentration exceeding 416 parts per million (ppm), a more than 30% increase since the first measurement in 1958.[3] Without immediate and dramatic changes in the global energy consumption patterns, CO_2 emissions will continue to rise precipitously, increasing the average surface temperature of our planet.

To address the climate change issue, representatives from 196 countries and regions made an agreement known as Paris Agreement in December 2015 to limit the temperature

rise to less than 2 °C above pre-industrial levels. This should be done by reducing emissions of CO_2 and other greenhouse gases as soon as possible. Like most other countries, the electricity generation in United States mainly comes from the combustion of fossil fuel, which accounts for most greenhouse gas emission. The US. Energy Information Administration reported that US electricity generation in 2020 was 66% from fossil fuels and 25% from renewable energy source.[4]

Despite a small proportion in energy production, the renewable electricity is developing in a tremendously fast pace. The electricity came from renewable source increased from 114 million kilowatts in 2000 to 284 million kilowatts in 2020, and its overall percentage in electricity manufacture increased from 14% to 25%. This has largely benefited from the booming of solar electricity and wind electricity that have grown about 120 times and 60 times, respectively, in the last 20 years, driven by the precipitous cost reduction from technical advancement and policy support. The momentum of renewable energy development is truly irresistible. Therefore, it is much anticipated that with continuing technological innovation, manufacturing capacity increasing and cost reduction, renewable energies will become the dominant sources for electricity production eventually.

The deep penetration of solar and wind power, however, is hindered by their intrinsically intermittency. The sun does not always shine, and the wind does not always blow, whereas the developed world has become accustomed to reliable, on-demand electricity (Figure 1.1). To tackle this challenge, efficient and inexpensive electrical energy

storage (EES) technology at grid scale is a viable solution.[5] In the short term, they store electricity when solar and wind power are in excess supply and release them when the demand is high. In the future when gigawatt hour electricity can be stored on a daily basis, solar and wind energy will become truly dispatchable.

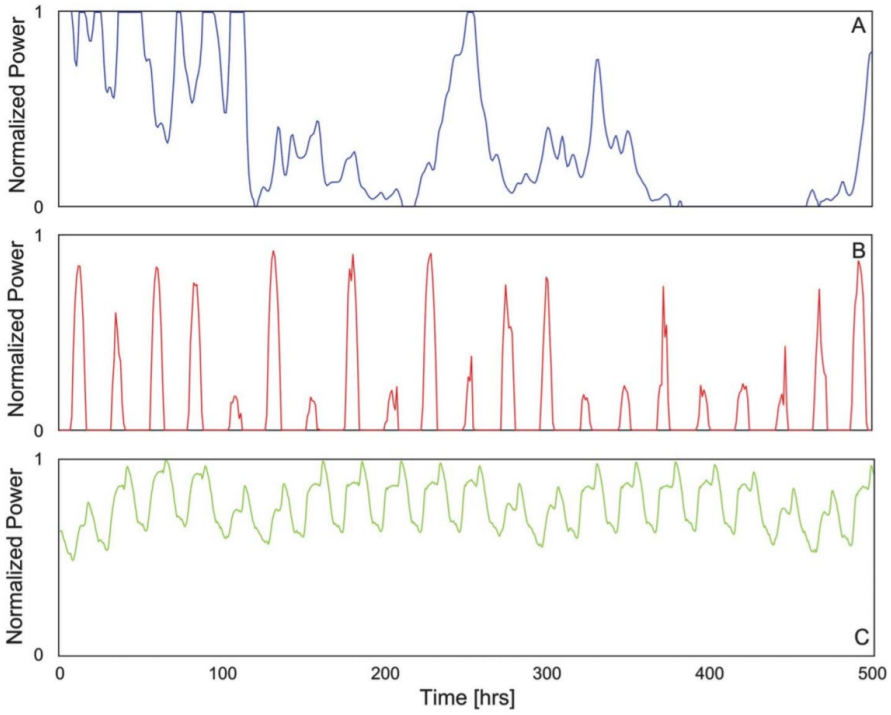

Figure 1.1 Normalized energy demand and power supply from renewable energy in 500 hours. A) normalized wind power in Netherlands; B) normalized solar power output in January in Boston, MA, USA; C) normalized electricity demand in the UK. Figure from reference 5.

When consider a grid-scale EES technology, two performance parameters are important: system power ratings (module size) and discharge time at a rated power.[6] The multiplication of the two terms leads to the total energy storage capacity. Typically, for renewable energy storage, the discharge time should be in the hours range, and module size

should be at least around MW. Among all current EES technologies, pumped hydroelectric energy storage (PHES) stands as the most established and largest-capacity option of storing bulk electricity.

PHES consists of two water reservoirs at different elevations that can generate power as water travels down through a turbine; this consumes power when it pumps water to the upper reservoir. It contributed a total power capacity of 21.9 GW and energy storage capacity of 553 GWh in United State in 2019, which accounted for 93% of utility-scale storage power capacity (GW) and more than 99% of electrical energy storage (GWh).[7] It continues to be the preferred least cost technology option for 4–16 hours duration storage. However, PHES is limited by the geological limitation, the construction of artificial water reservoirs and other infrastructures claim very high investment costs. Additionally, the potential site-specific negative environmental and ecological impacts are also big concerns.[8]

Electrochemical batteries represent a large group of technologies available for energy storage. Compared to PHES, electrochemical batteries have much higher volumetric energy density and round-trip energy efficiency, thus batteries can have a much smaller footprint, allowing them to be installed with greater flexibility, fewer geographical restrictions, and less impact on the surrounding environment. Two battery technologies of particular interest for EES are lithium-ion batteries (LIB) and aqueous redox flow batteries (ARFB).

LIB, first commercially introduced by Sony in the early 1990s, is a key technology enabling the rapid growth of portable electronic devices and electric vehicles. As the technological advancement and cost reduction in manufacturing over the past decades, many energy storage power plants based on LIB systems have been constructed or under construction. For instance, in 2014, Southern California Edison completed an 8 MW and 32 MWh EES based on LIB in Tehachapi California. Now the world's largest Li-ion battery EES is Moss Landing Energy Storage Facility in Moss Landing (California) with a 300 MW and 1200 MWh capacity.[9] It will grow to be a grid battery storage of over 567 MW/2,270 MWh when completed.

LIB EES systems will continue deployment at a high rate and be the dominant choice for batteries EES in the short term. However, many believe that less expensive battery technologies designed specifically for grid level EES will likely replace LIB in the future. LIB, like other solid-state batteries, are costly for long during energy storage because the battery power and energy are coupled to each other: increasing the battery capacity by increasing the volume of cathode and anode, will also enlarge their electrode size and increase the battery power. Consequently, for a long-during grid service, the power cost for LIB could be very high. Furthermore, to achieve high energy storage capability, thousands of individual cells are assembled together, increasing the difficulty for cell management and also safety concern.

1.2 Aqueous Redox Flow Batteries (ARFB)

Unlike the solid-state batteries, ARFB are particularly suitable for long-duration energy storage because of their technological merits of high power performance, decoupled energy and power, scalability, and safety features.[6, 10-12] The central components of redox-flow batteries are an electrochemical cell, two reservoirs, and pumps as shown in Figure 1.2. The electrochemical cell contains two porous carbon electrodes and a separator (mostly an ion exchange membrane). The chemical energy is stored in the two redox-active materials, which are dissolved or suspended in an electrolyte of the reservoirs. The electrolyte containing the lower redox potential species is called negative electrolyte or "negolyte", whereas the higher redox potential electrolyte is called positive electrolyte or "posolyte". The negolyte and posolyte flow through the electrochemical cell simultaneously by the pumps to proceed with electrochemical reactions. The separator is permeable to the charge carriers (conducting ions), but impermeable to the redox-active species. The energy capacity scales with the electrolyte volume, concentrations of redox-active species, and the cell potential; whereas the power scales primarily with the active area of porous carbons in the electrochemical cell. This enables energy and power to be scaled independently, making it highly modular and flexible to regulate energy and power generation. Therefore, for a long duration energy storage, i.e., a large energy-to-power ratio, the system cost per kWh of stored energy is mainly dependent on the cost of the electrolytes, rather than the cost of the electrochemical cell, making it less expensive than solid state

batteries.

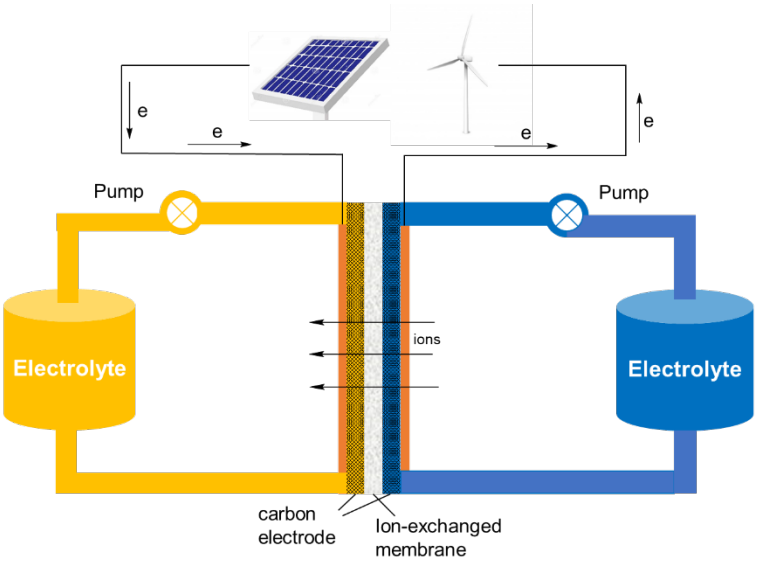

Figure 1.2 Schematic of a redox flow battery.

Redox flow batteries (RFBs) can be divided into two categories: 1) true redox flow batteries, where active species dissolved in the electrolyte all the time. All vanadium redox flow battery (VRFB) is a true redox flow battery; 2) hybrid redox flow batteries, where at least one chemical species is plated as a solid in the electrochemical cells during cycling. Zinc-based redox flow batteries are hybrid redox flow batteries. True RFBs achieve the complete separation of power and energy, along with other full advantages such as high power density and high energy efficiency. In hybrid RFBs, complete separation of power and energy is not achieved, because the energy is stored in the metal which is plated in the electrochemical stack during charge. Larger energy storage capacity requires a larger stack, so the distinction of the hybrid RFB from solid state batteries is only partly achieved.

1.2.1 Performance Parameters for ARFB

The four most important battery performance parameters of an ARFB are cycling stability, energy density, power density, and system cost. Previously, the cycling stability of ARFB was evaluated as an average capacity fade rate per cycle. However, recent studies showed that capacity fade rate per cycle cannot effectively reflect the cycling stability of ARFB.[13, 14] Fast cycling of a small volume of electrolyte will give a low-capacity fade rate per cycle; however, it masks the side reaction and crossover effect, which are the two main reasons for the capacity decay in ARFBs. Since both crossover of redox species and electrolyte lifetime are time dependent, it is more accurate to characterize the battery cycling stability with capacity fade per time or capacity retention per time, [13, 14] which is less dependent on cycling conditions.

Energy density E_d (Wh/L) measures how much energy can be stored in a unit volume of posolyte and negolyte. It is the product of battery voltage U and theoretical capacity (Ah/L) of ARFB system. The battery voltage U is determined by the difference in redox potential of the negolyte and posolyte, which stands for the highest driving force that a battery can supply. The theoretical capacity C_{ap} (Ah/L) of an ARFB is defined as the amount of charge that stored in a battery system, as described in equation 1.1

$$C_{ap} = n \times C \times F / 3600 / \mu_v = n \times C \times 26.8 / \mu_v \quad (1.1)$$

where n is the number of electrons participating in the redox process, C is the concentration of redox active species in the capacity limiting side with a unit of mol/L, F is Faraday's

constant with a unit of C/mol, and μ_v is the volume factor. The volume factor $\mu_v = 1 + V'/V$ of which V and V′ are the volume of capacity-limiting-side (posolyte or negolyte with the smaller capacity) and non-capacity-limiting side, respectively. The theoretical energy density E_d is calculated using equation 1.2

$$E_d = C_{ap} \times U = n \times C \times 26.8 \times U / \mu_v \quad (1.2)$$

The actual achieved energy density could be calculated simply by dividing the total electrolyte volume into actual delivered energy.

The power density describes power per unit area that the battery can supply, and the most commonly used unit is W/cm^2. It is calculated by equation 1.3.

$$P = U_d \times I_d / A \quad (1.3)$$

Where I_d is the discharge current, U_d is the discharge voltage, and A is the geometric surface area of electrodes. The factors that influence the power density are more complicated than those of the volumetric capacity and energy density. Apart from the battery voltage, the power density of an ARFB also affected by the conductivities of the electrolytes, membrane resistance, electrodes, kinetics of redox molecules, and also operating factors such as temperature, flow rate, and flow fields, which will influence the overpotential η of the ARFB at a given current density. The overpotential mainly consists of ohmic overpotential η_{ohm}, activation overpotential η_a and concentration overpotential η_c. The ohmic overpotential η_{ohm} is, as its name suggested, determined by the pure ohm's law and can be represented as equation 1.4:

$$\eta_{ohm} = R_{cell} I \quad (1.4)$$

The cell resistance R_{cell} include the electrolyte resistance from membrane resistance, electronic resistance from electrodes and current collector, and contact resistance of all cell components. The membrane resistance contributes a large proportion of cell resistance, thus, using a high ionic conductivity membrane raises the power density. The activation overpotential η_a is a result of resistance to electrochemical reaction kinetics occurring in the anode and cathode. Increasing the electrochemical kinetic rate constants k^0 of redox molecules could greatly decrease the activation overpotential. Concentration overpotential, η_c, is caused by the concentration gradient of the reactants or products in the bulk electrolyte and on the electrode surface, due to the limitation of mass transport as the redox reaction proceeds. This overpotential occurs when cell reaction is sufficiently fast and the mass transport is relatively slow. Redox active species with high diffusion coefficients contributed to a low concentration overpotential. In a redox flow battery, the mass transport is enhanced by pumping the electrolyte, thus the concentration overpotential could be minimized. Overall, by utilizing redox pairs with fast kinetics and low resistance membrane decrease the cell overpotential, therefore, improving the power density.

When considering the potential for practical application, the system cost of ARFB is one of the most important parameters but is also one of the most difficult ones to assess for a new redox chemistry. For instance, scientists at Massachusetts Institute of Technology invented a sulfur air redox flow battery for grid-level energy storage application.[15] The cost

of both sulfur and air are indeed pretty low, however, the high-cost of platinum and iridium oxide electrocatalyst as well as expensive solid electrolyte membrane increase the system cost. The long-term stability of ceramic membrane in alkaline condition is another big concern for long-term application, if unstable, then it will greatly increase the maintenance cost. The extremely low power density of 3.4 mW/cm^2 representing a high-power cost of the system. Therefore, the low cost of sulfur and air may not represent sulfur air redox flow battery has a strong competitivity even for the system cost.

Coulombic efficiency (CE), and energy efficiency are also important parameters for ARFBs. CE, also known as Faradaic efficiency or current efficiency, is the ratio of electrons delivered in the discharge process and electrons applied in the charging procedure, representing the reversibility of the redox system. Irreversible side reactions and crossover of the redox molecules will lead to a low CE (e.g., < 99%), eventually leading to a capacity imbalance and fast capacity decay. Round-trip voltage efficiency (VE) is the ratio of the average discharge voltage and the average charge voltage, which is mainly affected by the cell voltage, cell resistance, operational current density and electrochemical kinetics of redox molecules. The difference between average charge voltage and average discharge voltage is caused by the overpotential existed when a current is applied. Round-trip energy efficiency (EE), the product of CE and VE, is the ratio of the output energy in a discharge process and the input energy in a charge process. Apparently, a high energy efficiency is always desired, which can be achieved with a high ionic conductivity membrane, fast

kinetic redox molecules with a high battery voltage at an appropriate current density.

The redox-active material is important in determining the electrochemical performance of an ARFB. Many different redox-active materials have been investigated for ARFBs since its first invention in the 1970s. To date, the most investigated and well-established ARFB is an all-vanadium redox flow battery.

1.2.2 Vanadium redox flow batteries (VRFB)

VRFB was first introduced by University of New South Wales in the late 1980s.[16] It stores energy by employing vanadium redox couples in both negative and positive sides (V^{2+}/V^{3+} in the negolyte and VO^{2+}/VO_2^+ in the posolyte). These active species are fully dissolved in strong acid electrolyte solutions. The cell voltage of a VRFB at standard condition is 1.26 V. Its nominal cell voltage ranges from 1.15 to 1.55 V in acidic electrolytes because the posolyte redox potential is pH-dependent. During the discharge cycle, V^{2+} is oxidized to V^{3+} in the negative half-cell and VO_2^+ get reduced to VO^{2+} in the positive half-cell. Protons are shuttled between the two half-cells to maintain charge neutrality. To improve the solubility and stability of vanadium cations, mixed acid electrolyte was employed. With a mixture of hydrochloric acid and sulfuric acid, the stable temperature window increases to -10 to 50 °C with a high concentration of 2.5 M (energy density 40 Wh/L).[17] This is because the addition of Cl^- lead to the formation of chloride-complex V (V), preventing V_2O_5 formation and precipitation of low-valent vanadium species (II, III, IV) at low temperature.

Due to the small radius and positive charge, vanadium active species could diffuse

across the membrane. The cross-diffusion results in direct capacity and energy loss for that cycle. However, in VRFB, vanadium crossover does not result in permanent capacity loss, as both sides of electrolytes are the same element. One can simply mix the cycled posolyte and negolyte to recover the lost capacity.[18] However, the cross-diffusion of vanadium ions is still a big challenge as the expensive ion-exchange membranes is vulnerable to fouling, wherein vanadium ions become irreversibly trapped in the membrane and increase the cell resistance.[19] Therefore, low-cost membranes with high selectivity are highly desired.

All vanadium redox flow battery is now widely investigated in the pilot-phase scale. The world's largest VRFB, a 200 MW/800 MWh system, has been constructed by Rongke Power to peak shave about 8% of the city Dalian's expected load. The vanadium precursors for VRB electrolytes are either $VOSO_4$ or V_2O_5. V_2O_5 is cheaper than $VOSO_4$ but exhibits ten times lower solubility than $VOSO_4$.[20] To prepare the vanadium electrolyte, chemical or electrochemical methods are applicable and require a pre-charge step from a symmetric cell to obtain the desired vanadium electrolytes. The market price of vanadium as V_2O_5 is quite volatile. The high-cost of vanadium precursor is the major challenge for large-scale adoption of VRFBs. The system cost was estimated to be $330/kWh for a 10 MW/40 MWh VRFB reported by scientists at Pacific Northwest National Laboratory in December 2020,[21] which is significantly higher than the cost target of $100/kWh for energy storage set by the U.S. Department of Energy (DOE).[22]

1.2.3 Iron-based flow batteries

Iron-based electrolytes are promising candidates for ARFB owing to the natural abundance and low-cost of iron. Various redox molecules based on iron have been developed for flow batteries range from the negolyte to posolyte. The first iron-based flow battery is iron-chromium redox flow batteries (ICRFB), which were studied extensively by NASA in the 1970s[23] — 1980s and by Mitsui in Japan[24]. Both iron and chromium are low-cost and earth abundant, the system cost of ICRFB is expected to be much lower than that of VRFB. The negolyte contains a Cr^{2+}/Cr^{3+} species with a standard electrode potential $E° = -0.41$ V vs. SHE. Pairing with Fe^{2+}/Fe^{3+} ($E°$ = 0.77 V vs. SHE) in acid condition, it enabled an overall cell voltage of 1.18 V. In early implementations of the iron-chromium RFB, the diffusion of the iron and chromium ions across the separator created a capacity imbalance between the positive and negative electrolytes, resulting in an irreversible capacity loss. Later, researchers developed a mixed iron/chromium electrolyte to use for both sides to eliminate the irreversible loss. The capacity decay during a long-term operation can be somewhat recovered by simply mixing the positive and negative electrolytes.[25] The issues of ICRFB are the sluggish electrochemical kinetics of Cr^{2+}/Cr^{3+} redox reaction and the occurrence, on the negative side, of the hydrogen evolution reaction (HER). Hydrogen evolution not only reduces the energy efficiency, but also causes the state of charge (SOC) of positive and negative electrolytes to be imbalanced, ultimately triggering capacity decay. To tackle these challenges, Bi and Au–Tl electrocatalysts have been developed to enhance

the electrochemical kinetics of the Cr^{2+}/Cr^{3+} redox reaction, and suppress hydrogen evolution.[26, 27] In a comparative study of ICRFB and VRFB, though the system cost is estimated to be lower for ICRFB, the capacity decay was much faster in ICRFB applying mixed iron/chromium electrolytes and Bi catalysts than that of VRFB.[28]

Recently, ligands have been used to manipulate the redox chemistry of Cr(II)/Cr(III) in terms of redox potential, solubility, and redox kinetics.[29-32] Chromium ethylenediaminetetraacetic acid complex (Cr-EDTA) has been shown to shift the redox potential of Cr(II)/Cr(III) from -0.41 to -0.99 V vs. SHE at neutral pH and increase the redox kinetics by more than 10^5.[32] More recently, Marshak's group developed a chelated chromium 1,3-propylenediaminetertaacetic acid (Cr-PDTA) negolyte for high-voltage aqueous redox flow battery at near neutral pH. The redox potential of Cr-PDTA further shifts to -1.1 V vs. SHE. Meanwhile, it greatly enhanced the redox kinetics as well as suppressed the hydrogen evolution side reaction.[33] Pairing with ferrocyanide posolyte, it enables a full cell voltage of 1.6 V and a high peak power density of 0.515 W/cm^2. However, the cell cycling performance was not presented, only the energy efficiency and coulombic efficiency versus cycle number over 26 hours were exhibited.

Other iron-based flow batteries have also been proposed. Hybrid all-iron redox flow batteries feature low toxicity and low material cost. The negative electrolyte redox pair is Fe/Fe^{2+} (-0.44 V vs. SHE), while the positive electrolyte is Fe^{2+}/Fe^{3+} (0.77 V vs. SHE). The standard cell voltage is 1.21 V. This battery features a high energy density of 76 Wh L^{-1},

nevertheless, the power and energy are not completely decoupled, as the negative side involves the solid states. More importantly, the hybrid all-iron RFBs were thermodynamically unstable at the selected pH range. As shown in the Pourbaix diagram in Figure 1.3, the redox potential and the type of the most stabilized Fe-containing species were dependent on the pH of the aqueous electrolytes. The redox potential of Fe^{2+}/Fe is much lower than that of HER at pH 0, which makes the HER side reaction thermodynamically favorable in acidic Fe-based RFB systems. Moreover, metal iron is going to react with protons chemically, inducing a low coulombic efficiency and capacity imbalance. Furthermore, Fe^{3+} easily underwent hydrolysis when pH > 2, making it less attractive when paired with Fe^{2+}/Fe.

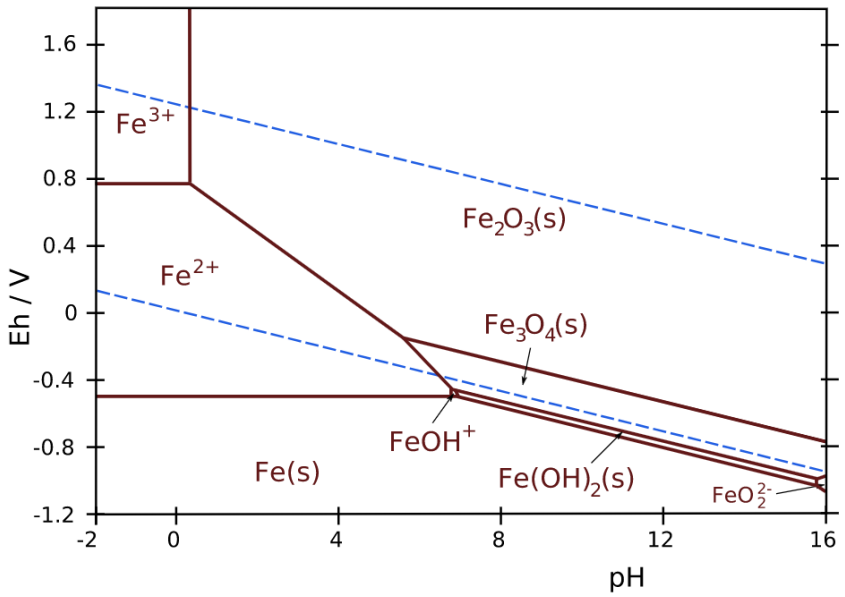

Figure 1.3 Pourbaix diagram of iron in uncomplexed media. Iron concentration 1 mM/L. Temperature 25 °C. The two blue dashed lines are oxygen evolution reaction and hydrogen evolution reaction.

Additionally, iron complex has also been developed. Yushan Yan *et al.* developed an all-soluble all-iron aqueous redox flow battery.[34] Compared to the hybrid all iron flow battery, this is a true flow battery as both negolyte and posolyte are fully dissolved in the electrolyte. The iron complex iron–triethanolamine (Fe-TEOA) has a low redox potential of -0.88 V vs. SHE. Pairing with ferrocyanide, it formed a full cell of 1.34 V, which is pretty good for an aqueous redox flow battery. At 70% SOC, the cell gave out a peak power density of 160 mW/cm^2. However, the large amounts of free ligands indicate that the Fe-TEOA is not very stable. The crossover of free TEOA ligand caused a low coulombic efficiency, as TEOA ligand could be oxidized by ferricyanide, leading to the shift of SOC of the system and eventually capacity decay.

The stability of metal complex is determined by the formation constant of metal cation with ligands. A high formation constant represents the strong coordination ability with metal and ligands. Among all the common ligands, CN^- has the largest formation constant K_f with both Fe(II) ($10^{\wedge 35}$) and Fe(III) ($10^{\wedge 42}$), therefore, ferrocyanide and ferricyanide are the two most stable metal complexes. The extreme stability of ferro/ferricyanide is the reason why they have low toxicity. Ferrocyanide has been widely used as a posolyte in neutral to alkaline condition, while in acid condition it releases toxic hydrogen cyanide to the solution. The redox potential is 0.47 V vs. SHE at all pH. The water solubility of ferrocyanide is 0.76 M (potassium form) and 0.56 M (sodium form) at pH 7, while ferricyanide has a much higher water solubility.[35] The water solubility of ferrocyanide

could improve to 1.5 M with a mixed Na^+/K^+ cations.[36] Leo Liu *et al.* discovered that with the ammonium (NH_4^+) cation, ferrocyanide solubility is greatly boosted to 1.6 M, thus doubling the volumetric capacity of ferro-/ferricyanide posolyte.[35] In an early report, ferrocyanide was thought to be unstable in alkaline as it was thought to undergo a hydrolysis reaction with hydroxide.[37] A more thorough study reveals that ferro-/ferricyanide are intrinsically chemically stable in alkaline condition and that the capacity decay is due to the shift of SOC of the system because ferricyanide gets reduced in basic conditions.[38] The extreme stability of ferro/ferricyanide in base media agree with the fact that the formation constant of iron and cyanide is much larger than that of iron and water/hydroxide. However, the low water solubility of ferrocyanide at high pH could be a concern for its extensive application in alkaline flow battery.

Recently, ferrocene derivatives have been studied for ARFBs. Ferrocene undergo a one-electron redox reaction with a redox potential around 0.4 V vs. SHE. Due to the remarkably reversible redox behavior, it has been used as a reference electrode in organic systems. Compared to ferrocyanide, ferrocene has the advantages of tuning ability in terms of redox potential and water solubility. Different ferrocene derivatives have been developed for ARFBs with a redox potential range from 0.37—0.63 V vs. SHE.[39-41] For example, Leo Liu *et al.* introduced a hydrophilic electron-withdrawing substituent to form FcNCl.[39] The redox potential of ferrocene increased to 0.61 V vs SHE. The water solubility is up to 4 M in deionized water and 3 M in 2 M sodium chloride. However, the electron withdrawing

group decreased the coordination ability of cyclopentadiene to the iron (III) center, making the ferrocenium less stable. Beh *et al.* introduced a lower redox potential ferrocene BTMAP-Fc.[40] The redox potential is 0.37 V vs SHE, which is similar to that of the unmodified ferrocene. Compared to FcNCl, BTMAP-Fc show much improved cycling stability. Recently, Qing Wang *et al.* developed a negative charged ferrocene Fc-SO_3Na by introducing two –$(CH_2)_3SO_3Na$ groups.[41] Fc-SO_3Na has a redox potential around 0.36 V vs. SHE, and it exhibited an extremely stable cycling performance. The decomposition of ferrocene posolyte is mainly via two routes. One route is two ferrocenium reacts with an oxygen molecule to generate a dimeric complex with a –O–O– bridge, which is unstable and further decompose to form iron (III) ion, iron (III) oxide, cyclopendiene, and Cp peroxide.[22] That's the reason why BTMAP-Fc showed fast decomposition when cycled in air and stable performance in nitrogen atmosphere.[40] Therefore, it is important to exclude O_2 for ferrocene cycling. The irreversible ligand exchange reaction between ferrocenium and nucleophilic reagents is another decomposition route for ferrocene posolyte. Because the ligand exchange reaction was coupled to a set of irreversible reduction reactions and Cp radical transformations, ferrocenium could be decomposed by weak ligands such as Cl^-, Br^-, H_2O. This is the main reason for the capacity decay of a ferrocene-based flow battery when operated under nitrogen.[22]

1.2.4 Zinc based flow batteries

Zinc is an attractive anode material that has been widely investigated in aqueous Zn-

ion,[42] and Zn-based hybrid flow batteries.[43] The intrinsic merits of the zinc anode for flow batteries include: 1) low chemical cost; 2) high volumetric capacity (e.g., ZnI_2 is 249 Ah L^{-1} and around 38 Ah L^{-1} for $[Zn(OH)_4)]^{2-}$)[44]; and 3) low redox potential. The redox potential of zinc is dependent on the pH of the aqueous electrolytes. The Pourbaix diagram of Zn (10^{-6} M Zn^{2+}) in Figure 1.4 indicates that the Zn/Zn^{2+} redox pair is stable at pH only between 6 and 8. When pH < 6, the hydrogen evolution reaction is favored. When the pH value is between 8 and 10, the main reactions were electrochemical and chemical deposition of the insoluble $Zn(OH)_2$. When pH above 10, insoluble $Zn(OH)_2$ begins to dissolve in the form of zincate ions (i.e., $HZnO^{2-}$ or $[Zn(OH)_4)]^{2-}$). Increasing the pH to beyond 13 will stabilize zincate ions at −1.2 V vs. SHE.

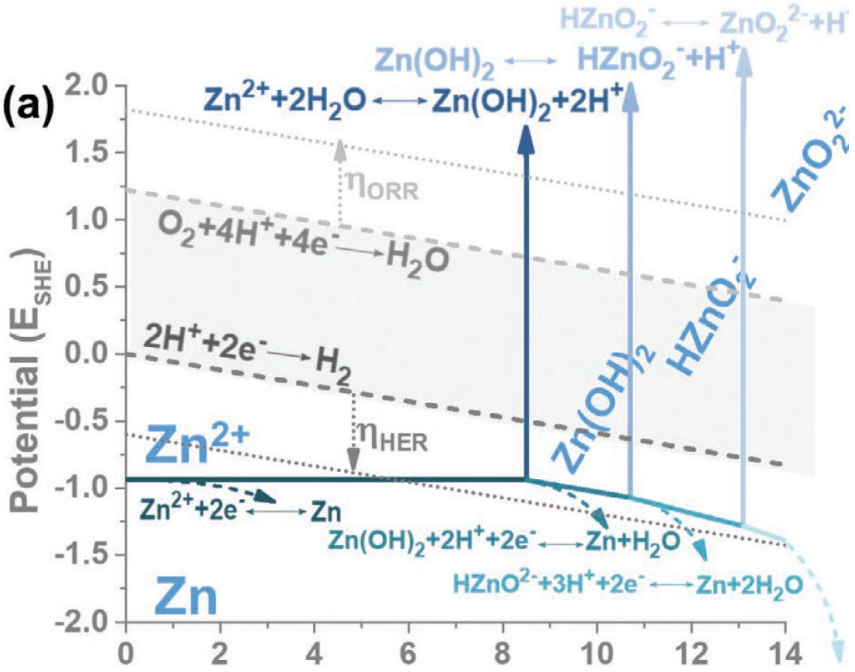

Figure 1.4 Pourbaix diagram of Zinc at 25 °C (Zn^{2+} = 10^{-6} M). Figure obtained from reference 44.

Because the ultra-low redox potential of zinc/zincate and high-water solubility of zincate, zinc/zincate often pairs with other redox pairs, such as I^-/I_3^-,[45] Fe^{2+}/Fe^{3+},[46] ferro/ferricyanide,[47, 48] and "frog quinone"[49] to form a high voltage (1.7—2 V) hybrid flow battery. However, many of these works ignore the poor compatibility between the two redox pairs, i.e., the posolyte is stable only in an acidic or neutral condition, while the zinc/zincate is stable only in strong base. Since no ion exchange membrane can eliminate hydroxide crossover, pairing zinc/zincate with I^{3-}/I^-, Fe^{2+}/Fe^{3+}, and frog quinone is intrinsically unstable in the long term. Apart from the crossover of zinc species, the growth of zinc dendrite is another issue for zinc-based hybrid flow batteries. The major disadvantages of dendrite formation are the low coulombic efficiency and possible short-circuiting due to dendrite penetration of the membrane. To suppress dendrite failure of Zn-based ARFB, multiple strategies have been applied: 1) mitigating the concentration gradient of zinc ion around dendrites by increasing the mass transfer; 2) increasing the mechanical or chemical stability of the membrane; 3) applying functional additive I^{3-} to react with the formed dendrite.[50]

1.2.5 Sulfur based flow batteries

Sulfur, owing to its extremely low cost and earth abundance as well as the high water solubility of alkali metal sulfide and polysulfides, has attracted tremendous interest for redox flow batteries application.[51] The standard redox potential of sulfide/polysulfide is

around -0.45 V vs. SHE. Different posolytes such as ferrocyanide, iodide, bromide, and oxygen have been applied for sulfur-based flow batteries.[15, 52-55] One drawback of the sulfur negolyte is the very sluggish kinetics, thus an effective electrocatalyst is needed. For example, Wang *et al.* developed a cobalt modified carbon electrode to increase the electrochemical kinetic of sulfur redox reaction for a polysulfide/ferrocyanide flow battery.[52] And Cai *et al.* developed a CoS_2/CoS electrocatalyst to improve the electrochemical kinetics of sulfur redox chemistry. However, the power density is still low with a peak value of 0.086 W/cm^2. Moreover, the long-term stability of these electrocatalysts is barely investigated. Another major issue with sulfur-based flow batteries is the fast crossover of sulfur species due to their small radius. When sulfide/polysulfides shuttle to the positive side, they get oxidized to form insoluble elemental sulfur, increasing the cell resistance and decreasing the electrochemical kinetics. Recently, Yichun Lu's group developed a carbon-coated Nafion membrane to address this issue: the interlayer structure suppressed the sulfide/polysulfides crossover. However, after 2.9 months operation, the resistance increased and capacity began to decrease,[56] indicating the crossover effect is only slightly suppressed, and it's far from a year-long operating system. One potential drawback ignored by researchers is the strong alkalinity of polysulfide solution, and sulfide/polysulfides are stable only at high pH. When the pH drops below 10, it should begin to release toxic hydrogen sulfide gas. Therefore, it is not good to be paired with a neutral or acidic posolyte. Additionally, I^-/I^{3-} is stable in acidic to neutral conditions and

become unstable when the pH rises above 12.[57] Therefore, a sulfur-based negolyte is not a good redox pair with an iodide posolyte in long-term cycling unless applying a perfect membrane that eliminates hydroxide and sulfide crossover. There is a similar requirement for a bromide posolyte, which is even less stable than iodide at high pH.

1.2.6 Aqueous Organic Redox Flow Batteries (AORFB)

The past decade has seen a boom of research on aqueous organic redox flow batteries (AORFB).[44] Redox-active organic molecules are promising candidates for novel ARFB due to their earth abundance and high tunability through functionalization. Their physical and electrochemical properties such as water solubility, molecular net charge, chemical stability, and redox potential can be tuned with different functional groups. Additionally, redox organics usually have large molecular sizes, thus the notorious crossover effect in inorganic active species is not a big challenge in redox organics. Many redox organics tend to have fast electrochemical kinetics, which contribute to a high power density.

In Chapter 2 of the thesis, two anthraquinone-based negolytes that could potentially last for decades are reported. The pH effect on anthraquinone stability is studied. An in-situ electrochemical synthesis is introduced to decrease the synthetic cost. Chapters 3 introduces a potential low cost and stable anthraquinone negolyte species for AORFB. Chapter 4 introduces a very low redox potential anthraquinone negolyte with an outstanding AORFB cycling performance at pH 14.

Chaper 2. Decadal Lifetime Anthraquinone Redox Flow Batteries Enabled by High pH and the *In-situ* Electrochemical Synthesis

Authorship: The following work has been largely adapted from the publication "Extremely Stable Anthraquinone Negolytes Synthesized from Common Precursors" written by Min Wu, Dr. Yan Jing, Dr. Andrew A. Wong, Eric M. Fell, Shijian Jin, Dr. Zhijiang Tang, Prof. Roy G. Gordon, Prof. Michael J. Aziz, published in *Chem* in 2020. Wu designed and synthesized the molecules, conducted the chemical stability and solubility tests, performed full cell tests, and wrote the manuscript draft except for the HPLC section which was written by Jing. And partly from the publication "In situ Electrosynthesis of Anthraquinone Electrolytes in Aqueous Flow Batteries" written by Dr. Yan Jing, Min Wu, Dr. Andrew A. Wong, Eric M. Fell, Shijian Jin, Daniel A. Pollack, Emily F. Kerr, Prof. Roy G. Gordon, and Prof. Michael J. Aziz, published in *Green Chemistry* in 2020. Wu synthesized the anthracene precursor, proposed the in-situ electrochemical oxidation method after Jing designed the electrochemical oxidation method, and compared the three different oxidation methods.

2.1 Introduction

The cost of solar and wind electricity has dropped so precipitously that the main barrier to widespread implementation is their intrinsic intermittency.[16, 10, 12] A safe, low-cost, large-scale electrical energy storage system could enable grid-scale adoption of renewables. Among the numerous proposed technologies, redox flow batteries (RFBs) have been recognized as a potentially viable strategy to address the intermittency of renewable energy.[10-12] Compared to conventional stationary rechargeable batteries (*e.g.*, lithium-ion batteries and lead–acid batteries), RFBs use redox-active materials dissolved in liquid supporting electrolytes that are stored in external tanks and separated from the power generation stack. This separation allows for the decoupling of energy capacity from maximum power output, thereby providing the possibility of low-cost long-duration discharge.[10-12]

Aqueous redox flow batteries featuring non-flammable electrolytes, are particularly suitable for storing massive amount of electricity. Aqueous vanadium RFBs are the most widely studied and adopted systems, but are hindered by the high cost of vanadium.[11, 12, 17] In contrast, redox-active organic molecules comprising earth abundant elements such as C, H, O, and N have the potential to be inexpensive alternatives to vanadium.[40, 58-63] Additionally, the structural diversity and tunability of organics enable chemists to design molecules with essential properties such as high aqueous solubility, high chemical stability, fast kinetics, and appropriate redox potential.[39, 40, 60-64]

Recently, water soluble anthraquinones 4,4'-((9,10-anthraquinone-2,6-diyl)dioxy)dibutyrate (2,6-DBEAQ) and (((9,10-dioxo-9,10-dihydroanthracene-2,6-diyl)bis(oxy))bis(propane-3,1-diyl))bis(phosphonic acid) (2,6-DPPEAQ) in mildly alkaline solutions have demonstrated extremely low temporal fade rates in flow batteries paired with $K_4Fe(CN)_6$.[65-67] These quinones are chemically synthesized from 2,6-dihydroxyanthraquinone (2,6-DHAQ) by industry-compatible methods. However, 2,6-DHAQ and 2,7-DHAQ are always co-produced and are costly to separate. Furthermore, our previous research showed that the molecular lifetimes of anthraquinone-based electrolytes can differ by two orders of magnitude depending on the positions of their functional groups (e.g., 1,8- and 2,6-anthraquinones).[65, 68] Therefore, it is important to quantify the stabilities of organic molecules with a mixture of isomers. Additionally, 2,6-DHAQ and 2,7-DHAQ are synthesized from 9,10-anthraquinone-2,6-disulfonic acid and 9,10-anthraquinone-2,7-disulfonic acid, respectively, in strong alkaline solution for 35 hours at high temperature (180 °C) with a moderate yield, which is energy-intensive and costly.[69] Thus, designing low-cost and chemically stable anthraquinones is of vital importance for the commercialization of aqueous organic redox flow batteries.

Because of the inherent chemical stability of the parent structure, the addition of side chains to an anthraquinone core is usually accomplished by a stepwise procedure *via* anthraquinone derivatives (e.g., hydroxylated anthraquinone or chlorinated anthraquinone).[65, 66, 68, 70] Here, we report a new synthetic route for water-soluble

anthraquinones starting from a potentially inexpensive anthracene derivative, 9,10-dihydroanthracene, which can be readily produced from anthracene with a yield of almost 100%.[71] Anthracene, a component of coal tar, is one of the major resources for large-scale anthraquinone production.[72] The first step is a Friedel-Crafts alkylation or acylation to render dihydroanthracene/anthracene water-soluble; the last step is an oxidation to produce the corresponding redox-active anthraquinones, *i.e.*, 3,3'-(9,10-anthraquinone-diyl)bis(3-methylbutanoic acid) (DPivOHAQ) and 4,4'-(9,10-anthraquinone-diyl)dibutanoic acid (DBAQ).

Both molecules exhibit high water solubility and chemical stability at pH 12. The DBAQ has a water solubility of 1.0 M, corresponding to a volumetric capacity of 53.6 Ah/L for the negolyte; when paired with potassium ferrocyanide, a full cell exhibited a capacity fade rate of 0.0084%/day or 3.1%/year. DPivOHAQ has a solubility of 0.74 M; when paired with potassium ferrocyanide, a full cell exhibited a capacity fade rate of 0.014%/day or 5.1%/year. Additionally, we demonstrated that the DPivOHAQ negolyte species is even more stable in strong base, exhibiting a capacity fade rate of 0.0018%/day or 0.66%/year at pH 14. Furthermore, we demonstrated that the capacity fade is due to formation of anthrone, which can convert back to anthraquinone through air exposure and can also be suppressed at high pH. Thus, these findings suggest that, through a combination of increased pH and periodic air exposure, both DPivOHAQ and DBAQ offer the

possibility of decadal lifetimes in aqueous RFBs. In the following section we report methods and results, first for DPivOHAQ and then for DBAQ.

2.2 Experiment section:

9,10-dihydroanthracene (97%), 3,3-dimethylacrylic acid (97%), and anhydrous dichloromethane were purchased from Sigma Aldrich. Anhydrous aluminum chloride (95%) was purchased from Alfa Aesar. All chemicals were used as received.

2.2.1 Synthesis of 3,3'-(anthracene-diyl)bis(3-methylbutanoic acid) (DPivOHAC):

13.32 g (99.93 mmol) of $AlCl_3$ was suspended in ~200 mL of anhydrous CH_2Cl_2. A solution of 6.67 g (66.62 mmol) of 3,3-dimethylacrylic acid in ~20 mL of anhydrous CH_2Cl_2 was added by syringe and the mixture stirred at room temperature for 0.5 hour under nitrogen. Subsequently, a solution of 5.00 g (27.74 mmol) of 9,10-dihydroanthracene in ~15 mL of anhydrous CH_2Cl_2 was added to the above mixture and stirred for 48 hours at room temperature. Following that, the solvent was quenched with 200 mL of 1 M aqueous HCl and stirred overnight. The organic layer was then removed and the remaining solution was filtered to afford the pale-yellow product. Yield: 95%.

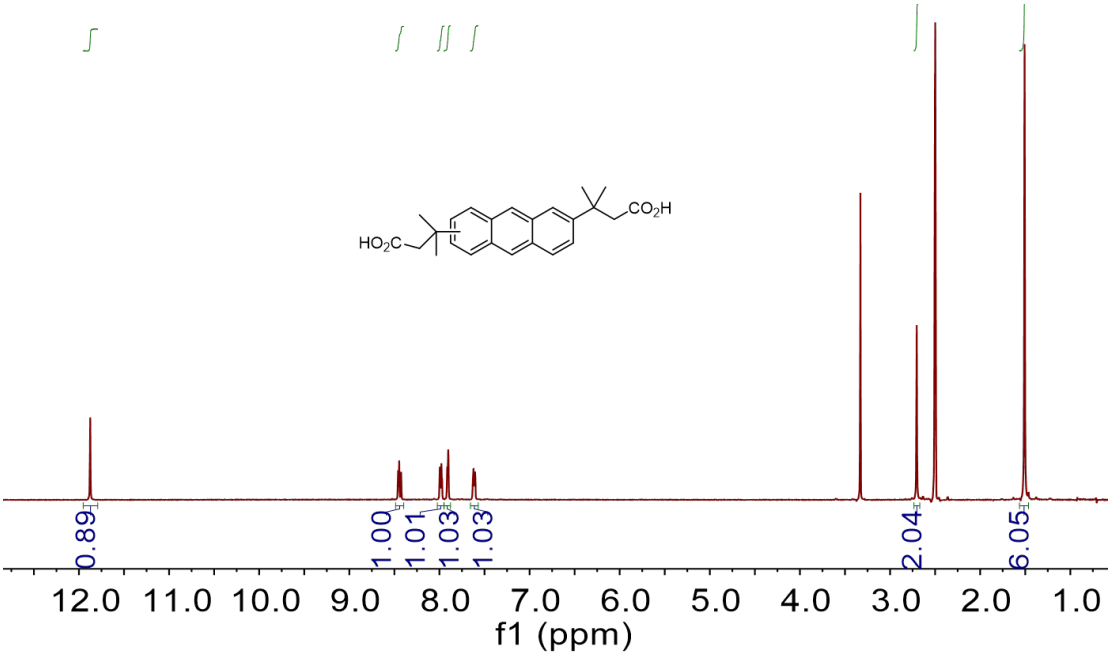

Figure 2.1 ^{1}H NMR spectrum of DPivOHAC in DMSO-d_6. Solvent peaks are those that are not integrated. ^{1}H NMR (500 MHz, DMSO-d_6) δ 11.88 (s, 2H), 8.45 (t, 2H), 7.99 (dd, 2H), 7.91 (d, 2H), 7.62 (d, 2H), 2.71 (s, 2H), 1.51 (s, 6H).

2.2.2 Synthesis of DPivOHAQ:

DPivOHAC (6.00 g, 15.85 mM) was dissolved in glacial acetic acid (70 mL). Then, a CrO_3 solution (3.33 g, 33.3 mM) was added to the DPivOHAC/acetic acid mixture. The reaction mixture was heated at 90 °C for 1 h. After cooling down to room temperature, water was added to precipitate the solid. The compound was purified by dissolution in base followed by addition of acid to afford the precipitate. Yield: 85%.

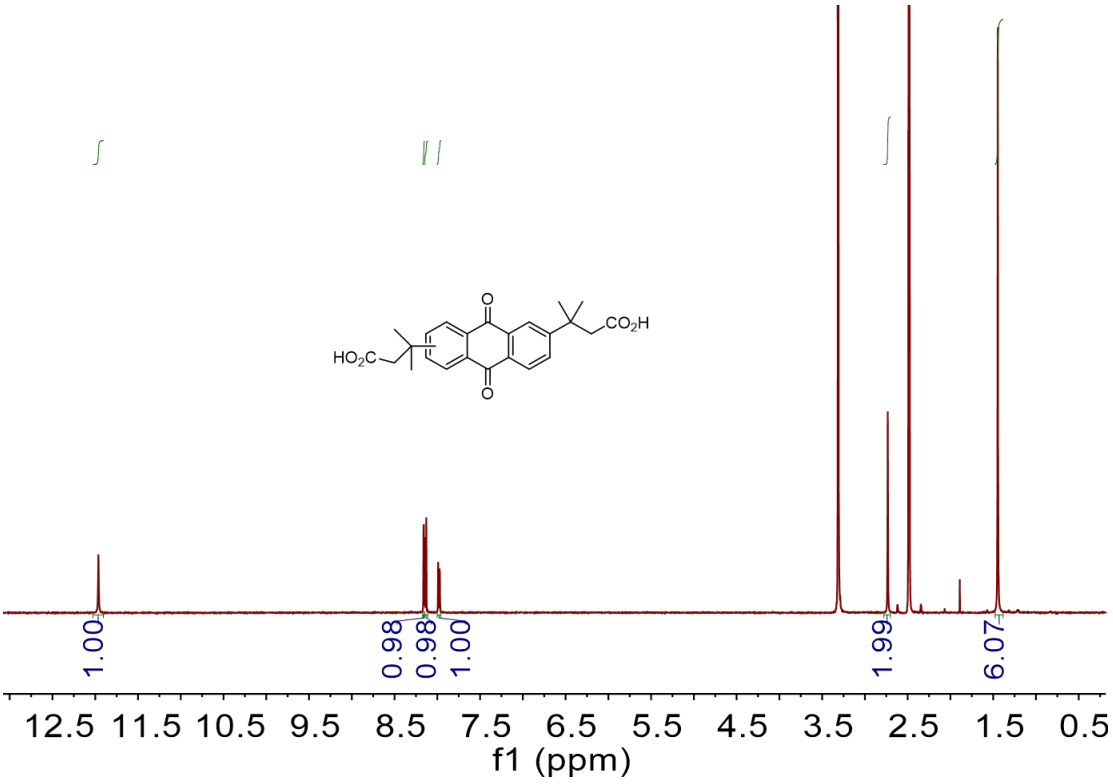

Figure 2.2 ^{1}H NMR spectrum of DPivOHAQ in DMSO-d_6. Solvent peaks are those that are not integrated. ^{1}H NMR (500 MHz, DMSO-d_6) δ 11.99 (s, 2H), 8.17 (d, 2H), 8.15 (d, 2H), 8.0 (dd, 2H), 2.75 (s, 2H), 1.46 (s, 6H).

2.2.3 4,4'-(9,10-dihydroanthracene-diyl)bis(4-oxobutanoic acid) (DOBDHAC):

15.50 g (115.89 mmol) of $AlCl_3$ was suspended in ~200 mL of anhydrous CH_2Cl_2. A solution of 5.69 g (56.49 mmol) of succinic anhydride was added and the mixture stirred

at 0 °C for 0.5 hour under nitrogen. Subsequently, a solution of 5.00 g (27.74 mmol) of 9,10-dihydroanthracene in ~15 mL of anhydrous CH_2Cl_2 was added to the above mixture and stirred overnight. Then the suspension was filtered to obtain the red solid, which was then washed with ice water twice and filtered to afford a yellow solid (10.5 g). Yield: 99%.

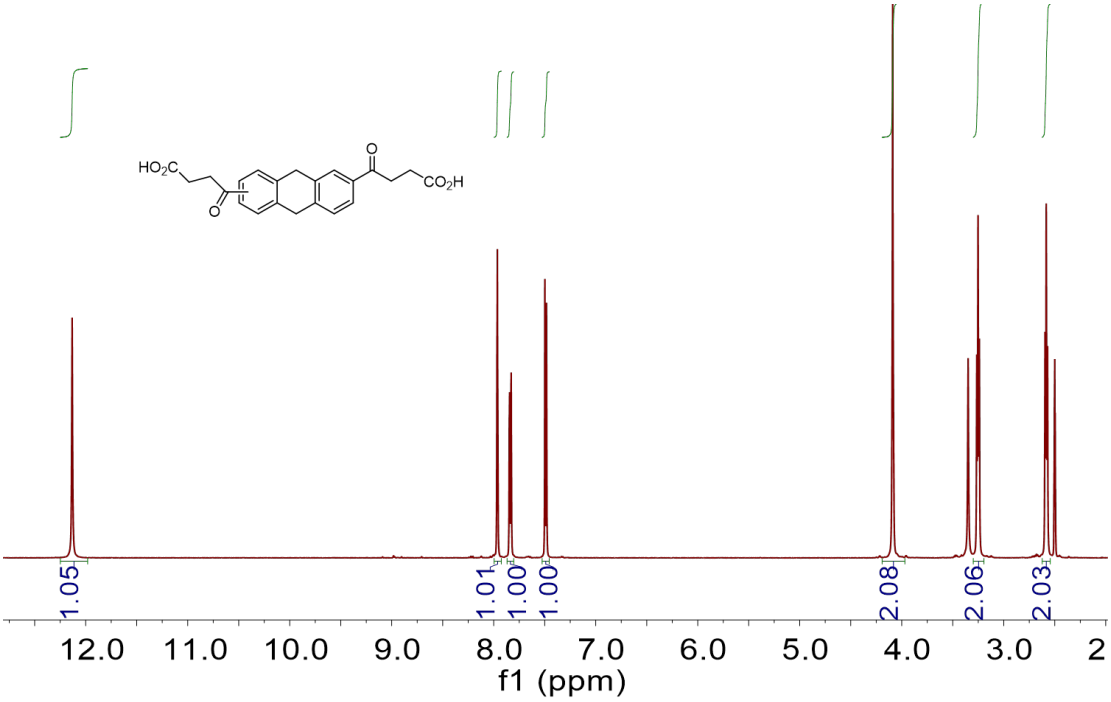

Figure 2.3 ^{1}H NMR spectrum of DOBDHAC in DMSO-d_6. Solvent peaks are those that are not integrated. ^{1}H NMR (500 MHz, DMSO-d_6) δ 12.13 (s, 2H), 7.96 (t, 2H), 7.84 (dd, 2H), 7.49 (d, 2H), 4.09 (s, 4H), 3.25 (t, 4H), 2.58 (t, 4H).

2.2.4 Synthesis of 4,4'-(9,10-dihydroanthracene-diyl)dibutanoic acid (DBDHAC):

To a solution of DOBDHAC (10.5 g, 27.74 mmol) in diethylene glycol (100 mL) at room temperature was added hydrazine monohydrate (98%, 8 mL, 166 mmol). The reaction mixture was stirred for half an hour. Then potassium hydroxide was added (8.73 g, 155.59 mmol) and stirred at 100 °C for 1 hour under nitrogen. Then the temperature was allowed

to rise to 200 °C for 4 hours. After cooling to room temperature, 500 mL of water was added to the solution, which was then filtered twice to remove insoluble solid. The filtrate was acidified with 5 M HCl to adjust the pH to 1, and the resulting precipitate was collected and washed with water (500 mL) twice to afford the light brown solid. Yield: approximately 95%. ^{1}H NMR indicated that the product was DBDHAC (4,4'-(9,10-dihydroanthracene-2,6-diyl)dibutanoic acid) with around 10% percent of DBAC (4,4'-(anthracene-diyl)dibutanoic acid). As both dihydroanthracene and anthracene may be converted to anthraquinone, no further purification was needed at this step.

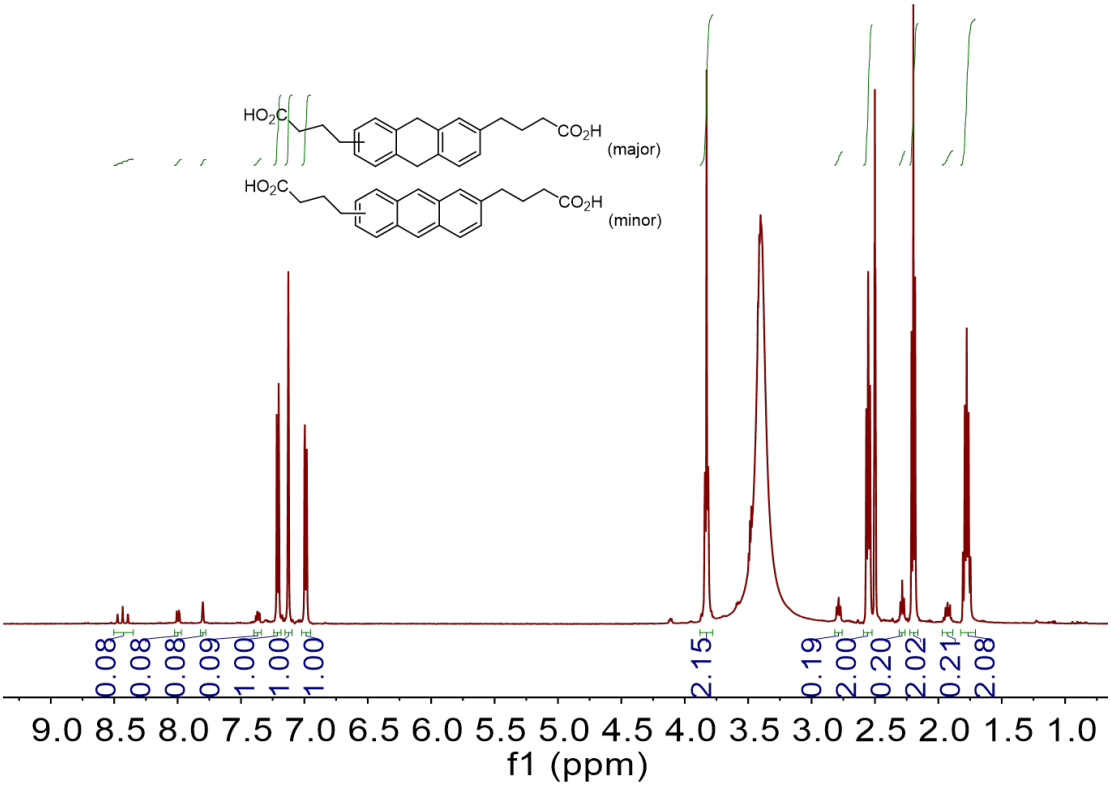

Figure 2.4 ^{1}H NMR spectrum of DBDHAC in DMSO-d_6. Solvent peaks are those that are not integrated. ^{1}H NMR (500 MHz, DMSO-d_6) DBHAC: δ 7.21 (d, 2H), 7.13 (s, 2H), 6.99 (dd, 2H), 3.83 (t, 4H), 2.55 (t, 4H), 2.20 (t, 4H), 1.78 (m, 4H). DBAC: δ 8.43 (t, 2H), 7.99 (dd, 2H), 7.80 (s, 2H), 7.37 (t, 2H), 2.79 (t, 4H), 2.29 (t, 4H), 1.93 (m, 4H).

2.2.5 Synthesis of DBAQ:

DBDHAC (10 g, 28.4 mM) was dissolved in 100 mL glacial acetic acid. Then, a CrO_3 solution, prepared by dissolving CrO_3 (7.1 g, 71 mM) in 4 mL of water, was added to the above solution. The reaction mixture was allowed to stir at room temperature overnight. Then 300 mL of water was added to the mixture, which was then filtered to afford the yellow product. The product was dissolved in base and further acidified to afford a yellow precipitate. The last step was used to remove the residual Cr (III) compound. Yield: 90%.

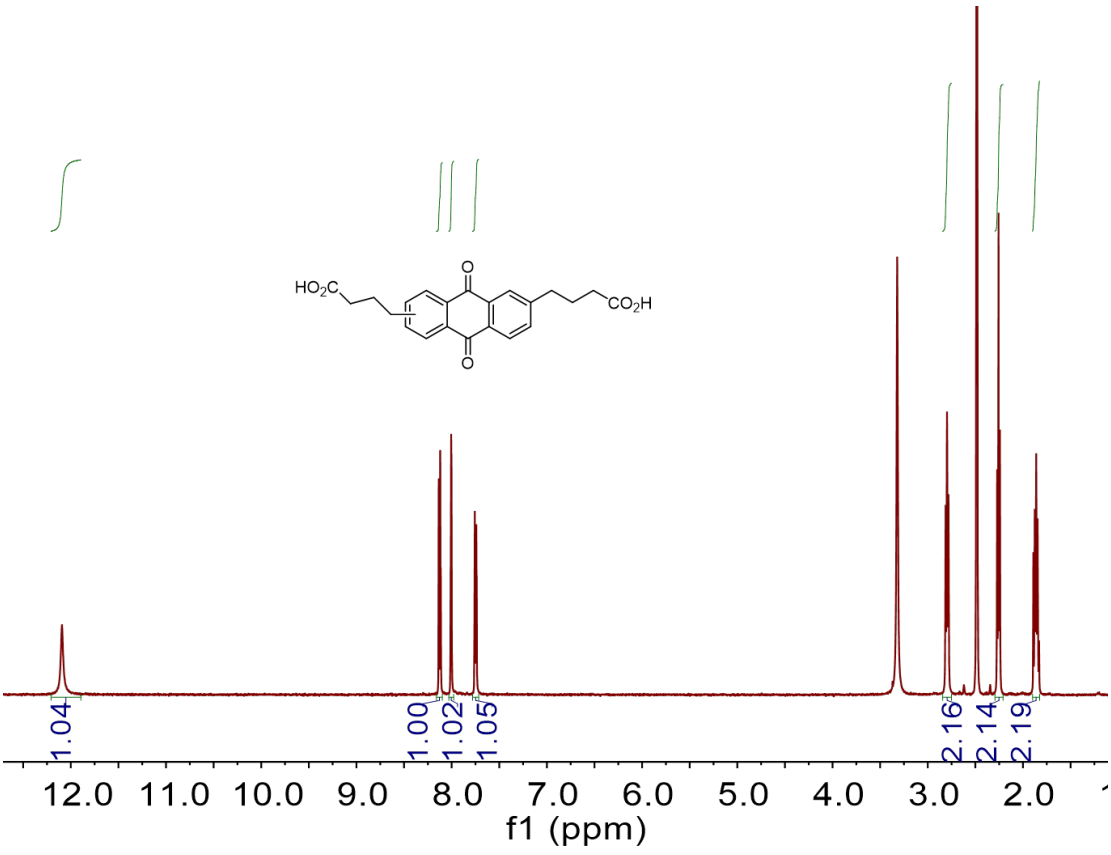

Figure 2.5 ^{1}H NMR spectrum of DBAQ in DMSO-d_6. Solvent peaks are those that are not integrated. ^{1}H NMR (500 MHz, DMSO-d_6) δ 8.05 (dd, 2H), 7.94 (t, 2H), 7.70 (dd, 2H), 2.77 (t, 4H), 2.27 (t, 4H), 1.86 (m, 4H).

2.3 Results and discussion

Figure 2.6 illustrates the synthetic routes, chemical structure, Pourbaix diagram, and cyclic voltammogram (CV) of DPivOHAQ. Synthesis was achieved by first functionalizing 9,10-dihydroanthracene with the water-soluble group -$C(CH_3)_2CH_2COOH$, followed by an oxidation step with CrO_3. The oxidation step is well known in industry for anthraquinone synthesis, and it can also be accomplished by other methods, such as nitric acid/air, that could further decrease the costs.[73, 74] Compared to 2,6-DBEAQ and 2,6-DPPEAQ synthesis, the reported synthetic approach could be potentially more cost-effective. For example, assuming anthracene is the starting material, both DBEAQ and DPPEAQ require five synthetic steps in total as illustrated in Scheme 2.1 with an overall yield around 52% and 59%, respectively; whereas DPivOHAQ synthesis requires only three steps with an overall yield of 81%. Moreover, the cost of side chains for DPivOHAQ is slightly lower than that of DBEAQ and substantially lower than that of DPPEAQ, as shown in Table 2.1. Therefore, we expect that DPivOHAQ is most likely less expensive to produce than DBEAQ and DPPEAQ at industrial scales.

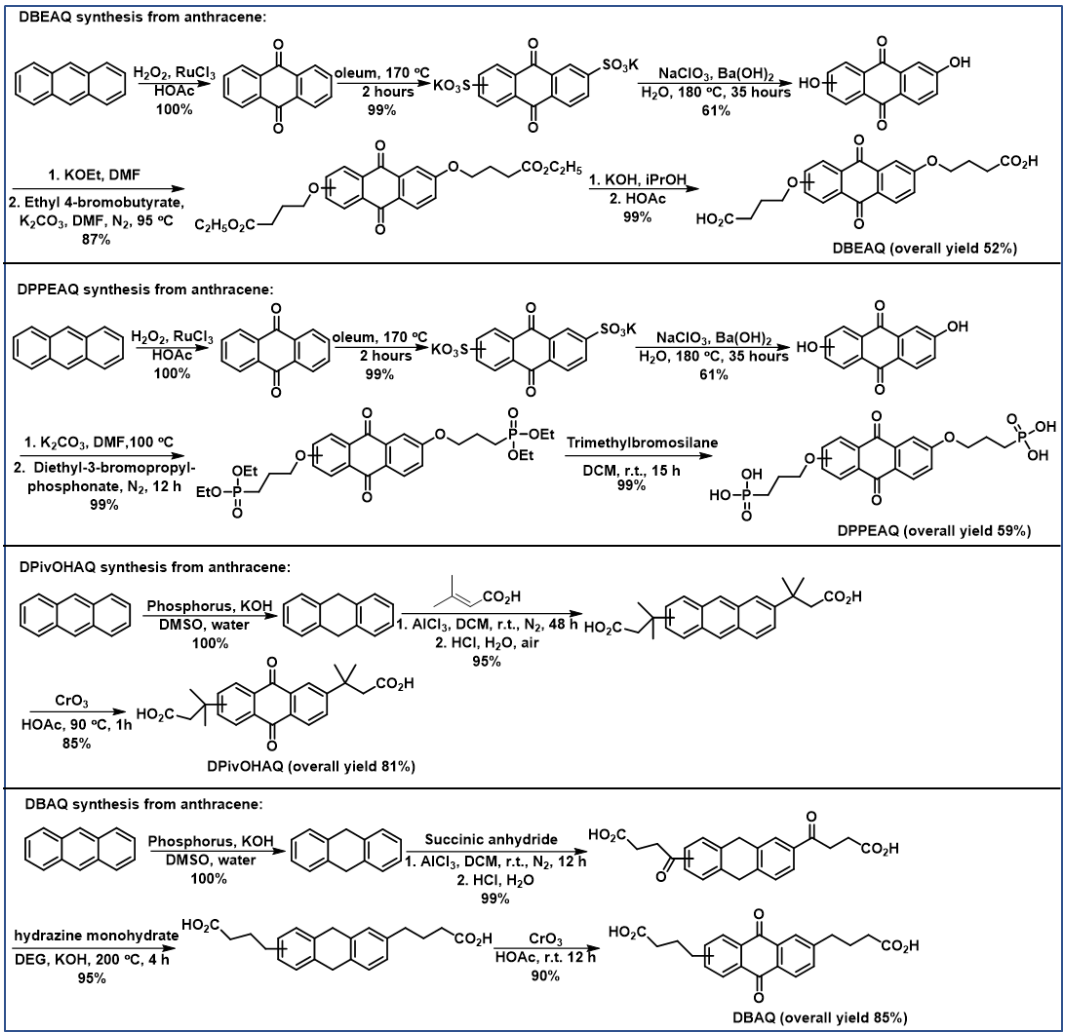

Scheme 2.1. Comparison of the synthetic routes for DBEAQ,[58, 65, 75, 76] DPPEAQ,[58, 66, 75, 76] DPivOHAQ,[71]and DBAQ[71] from anthracene.

Table 2.1 Lab-scale cost for raw materials of four stable anthraquinones from Sigma-Aldrich in Nov. 2019.

	2,6-DHAQ	DBEAQ	DPPEAQ	9,10-dihydroanthracene	DPivOHAQ	DBAQ
side chain		ethyl 4-bromobutyrate	diethyl-3-bromopropylphosphonate		3,3-dimethylacrylic acid	succinic anhydride
cost	5 g: $105	250 g: $138	5mL: $91	5 g: $41.1	500 g: $152	500 g: $41
unit price ($/mol)	5044.4	107.7	3498	1481	30.4	8.2

Note that even though the lab-scale cost of 2,6-DHAQ is high, the mass production cost of 2,6-DHAQ is predicted to be as low as $2.4/kg by Borealis Technology Solutions LLC.[62] As the lab-scale cost of 9,10-dihydroanthracene is approximately one third of that of 2,6-DHAQ, we suppose the cost of 9,10-dihydroanthracene could be inexpensive if produced in large-scale.

In addition to potentially lower synthetic costs, DPivOHAQ is functionalized with carbon-linked functional groups, which are chemically more robust than the oxygen-linked side chains in DBEAQ and DPPEAQ, minimizing the opportunity for S_N2 and S_NAr side reactions to occur.[65, 66] The thermochemical stability of both oxidized and reduced forms of 0.1 M DPivOHAQ were evaluated at high temperature (65 °C) and in strongly alkaline conditions (pH 14) for eight days. The extent of decomposition was determined by ^1H NMR, with peak integrals measured relative to an internal standard of $NaCH_3SO_3$ prepared at 10 mM concentration in D_2O. All samples were diluted in this deuterated solvent containing the internal standard at a fixed ratio of 1:5. No apparent decomposition was detected from the ^1H NMR as shown in Figure 2.6, indicating that DPivOHAQ is quite chemically stable.

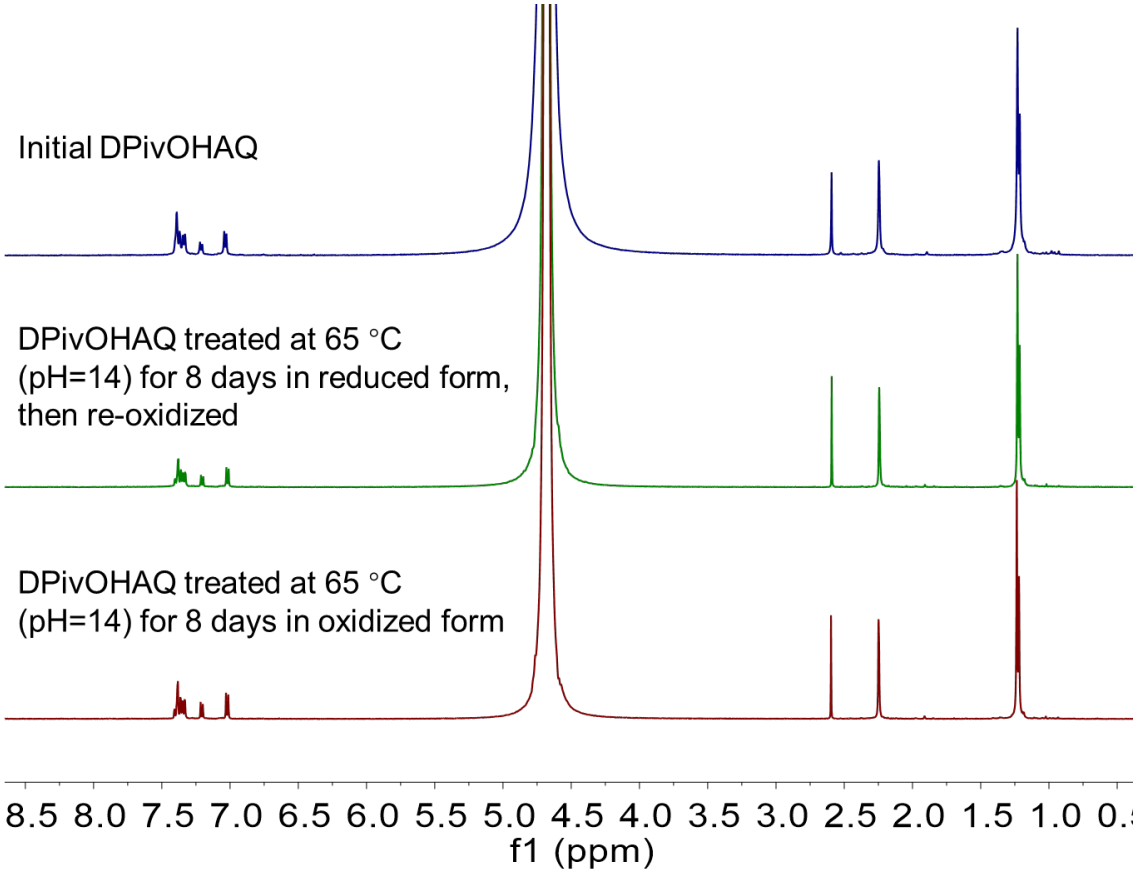

Figure 2.6 ^{1}H NMR spectra (500 MHz, 1 M KOD in D_2O with 10 mM $NaCH_3SO_3$ internal standard) of (a) the oxidized form of DPivOHAQ in pH 14 aqueous solution (1 M KOH); (b) DPivOHAQ treated at 65 °C for 8 days at 0.1 M concentration in pH 14 aqueous solution (1 M KOH) in the reduced form and then re-oxidized in order to compare to samples tested in the oxidized form; (c) DPivOHAQ treated at 65 °C for 8 days at 0.1 M concentration in pH 14 aqueous solution (1 M KOH) in the oxidized form. No apparent decomposition was detected; the integration did not appreciably change.

Synthesis of DPivOHAQ results in a mixture of 2,6- and 2,7- isomers that does not require further separation prior to use in a battery. The Pourbaix diagram of DPivOHAQ, shown in Figure 2.7b, suggests that the molecule undergoes a two-proton/two-electron process below pH 9, a one-proton/two-electron process between pH 9 and 11, and a zero-proton/two-electron process with a pH-independent potential of approximately -0.48 V

versus SHE at pH>11. Pairing a DPivOHAQ negolyte with potassium ferrocyanide at pH 12 should yield an equilibrium cell potential of approximately 0.98 V (Figure 2.7c).

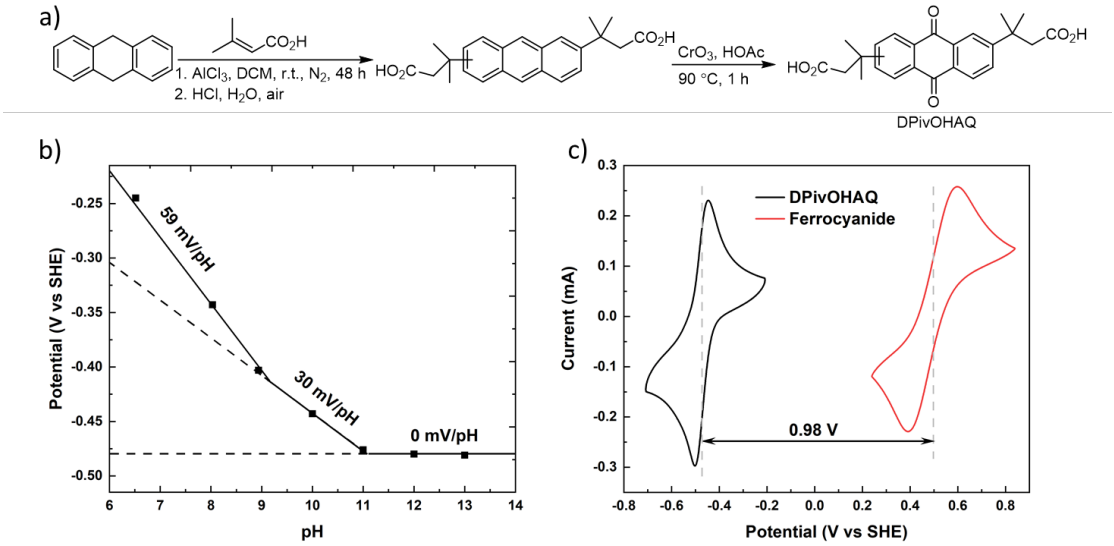

Figure 2.7 DPivOHAQ synthesis and electrochemistry. a) Synthetic route for DPivOHAQ; b) Pourbaix diagram; c) Cyclic voltammograms of 5 mM DPivOHAQ and 10 mM potassium ferrocyanide at pH 12 with a scan rate of 100 mV/s.

Electrochemical kinetics of DPivOHAQ reduction were determined with the rotating disk electrode (RDE) method as shown in Figure 2.8. Glassy carbon was used as the working electrode for all three-electrode CV tests. RDE experiments were conducted using a Pine Instruments Modulated Speed Rotator AFMSRCE equipped with a 5 mm diameter glassy carbon working electrode, a Ag/AgCl reference electrode (BASi, pre-soaked in a 3 M NaCl solution), and a graphite counter electrode. The diffusion coefficient of the oxidized form of DPivOHAQ was calculated using the Levich equation, which relates the mass-transport-limited current to the number of electrons transferred (n), the area of the electrode (A), and the concentration of redox-active species in the electrolyte (C) by

plotting the mass-transport-limited current against the square root of the rotation rate (Figure 2.8b) with the following parameters: n = 2, F = 96,485 Coulombs/mol, A = 0.196 cm^2 , C = 5 mM, kinematic viscosity of 1 M KCl = 0.89×10^{-6} m^2/s.[77] The resulting value of the diffusion coefficient for the oxidized form of DPivOHAQ is 2.4×10^{-6} cm^2/s.

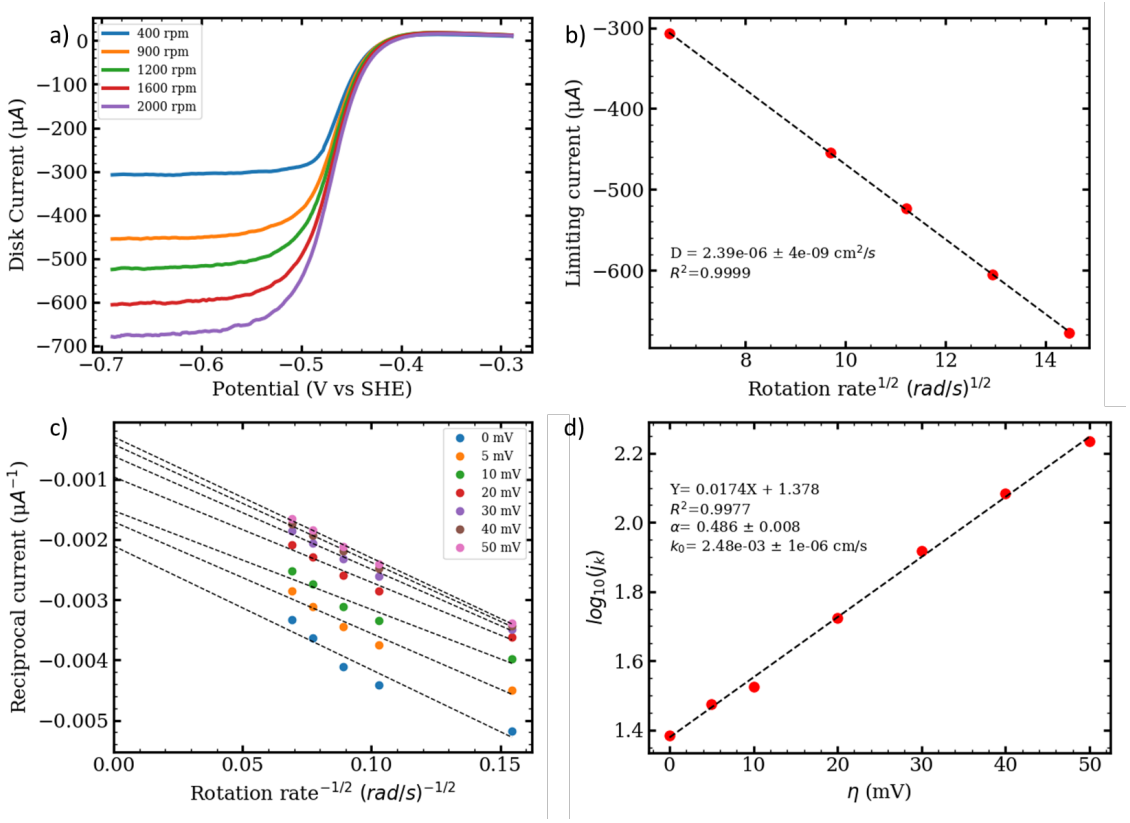

Figure 2.8 DPivOHAQ reduction kinetics in RDE. a) Linear sweep voltammograms of 5 mM DPivOHAQ in 1 M KCl at pH 12 on a glassy carbon electrode at rotation rates between 400 and 2000 rpm. b) Levich plot (limiting current versus square root of rotation rate in rad/s) of 5 mM DPivOHAQ in 1 M KCl at pH 12. Limiting current is taken as the current at -0.65 V in (a). The slope yields a diffusion coefficient for the oxidized form of DPivOHAQ of 2.39×10^{-6} cm^2 s^{-1}. c) Koutecky-Levich plot (reciprocal current versus inverse square root of rotation rate in rad/s) of 5 mM DPivOHAQ in 1 M KCl at pH12. d) Fitted Tafel plot of 5 mM DPivOHAQ in 1 M KCl at pH 12. The charge transfer coefficient is calculated to be 0.49, and the rate constant is calculated to be 2.48×10^{-3} cm s^{-1}.

The charge transfer coefficient is 0.49, the diffusion coefficient is 2.4×10^{-6} cm^2/s, and the kinetic rate constant is 2.5×10^{-3} cm/s; the latter is much higher than is typical of inorganic redox active materials.[78] The solubilities of the oxidized forms of anthraquinones in alkaline solutions are typically lower than those of the reduced forms.

The solubility limit of DPivOHAQ was measured in the oxidized form by adding the potassium salt of DPivOHAQ (prepared by reacting DPivOHAQ with potassium hydroxide in water) until no further solid could be dissolved. The mixture was adjusted to pH 12. After the suspension was filtered through a nylon 0.45 μm syringe filter, a saturated solution of DPivOHAQ at pH 12 was obtained. The saturated solution was then diluted 20,000 times while maintaining a pH of 12, and the concentration was evaluated by UV–Vis spectrophotometry (Agilent Cary 60 spectrophotometer). The concentration was calculated according to a pre-calibrated absorbance concentration curve of known concentrations of DPivOHAQ at pH 12. The resulting value of the solubility of the oxidized form of DPivOHAQ at pH 12 is 0.74 M. The solubility of DPivOHAQ at pH 12 was determined by UV-Vis spectrophotometry (Figure 2.9) to be 0.74 M, corresponding to a volumetric capacity of 39.7Ah/L. For the solubility of K_2DBAQ, we prepared a 1.0 M solution in pH 12 KOH and found that it remained fully dissolved. We did not determine an upper limit. Therefore we report the solubility as 1.0 M.

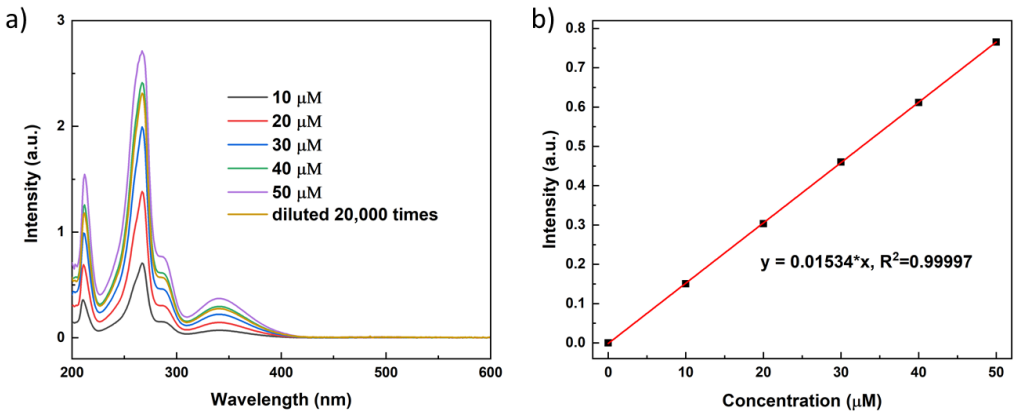

Figure 2.9 Solubility test of DPivOHAQ. a) UV–Vis spectra of DPivOHAQ at different concentrations; b) the absorbance at 287.9 nm versus the concentration; a least-squares linear fit to the data was performed to generate the calibration curve utilized in this work. The saturated sample was diluted 20,000 times and calculated to be 0.74 M at pH 12.

Polarization experiments of a 0.5 M DPivOHAQ/ferrocyanide full cell at pH 12 were performed at various states of charge. The electrolytes comprised 5 mL of 0.5 M DPivOHAQ (negolyte) at pH 12 (10 mM KOH) and 80 mL of 0.3 M potassium ferrocyanide and 0.1 M potassium ferricyanide (posolyte) at pH 12. The cell was constructed from graphite flow plates and AvCarb carbon cloth electrodes, separated by a Fumasep E-620 (K) membrane because of its low permeability of ferricyanide and high ionic conductivity.[65, 66] A peak galvanic power density of 0.34 W cm^{-2} was achieved at ~100% SOC (Figure 2.10a). The open-circuit voltage (OCV) increases from 0.95 to 1.08 V as the SOC increases from 10% to ~100%, and the OCV at 50% SOC of 0.99 V (Figure 2.10b) is consistent with the voltage expected from CV. The alternating current area-specific resistance (ASR) of the cell was determined *via* high-frequency potentiostatic electrochemical impedance spectroscopy (EIS), and the value was below 0.6 Ω cm^2 across

all SOCs (Figure 2.10b). This is a relatively low alternating current ASR value for RFBs with alkaline electrolytes.[65, 66] The polarization ASR was determined using the linear region within the voltage range 0.9−1.1 V (Figure 2.10a, b). The ASR of the membrane (0.54 Ω cm^2 at 50% SOC, determined by high-frequency EIS in the full cell) accounted for around 67% of the ASR of the entire cell (0.81 Ω cm^2 at 50% SOC, DC polarization). The capacity utilization is approximately 95% at 50 mA cm^{-2} with a high round-trip energy efficiency of 91.5% (Figure 2.10c, d). At a reasonable practical operation target of 80% round-trip energy efficiency, the low value of the ASR permits galvanostatic operation at around 140 mA cm^{-2} with an electrolytic power density of 0.16 W cm^{-2}, a galvanic power density of 0.13 W cm^{-2}, and 92% capacity utilization.

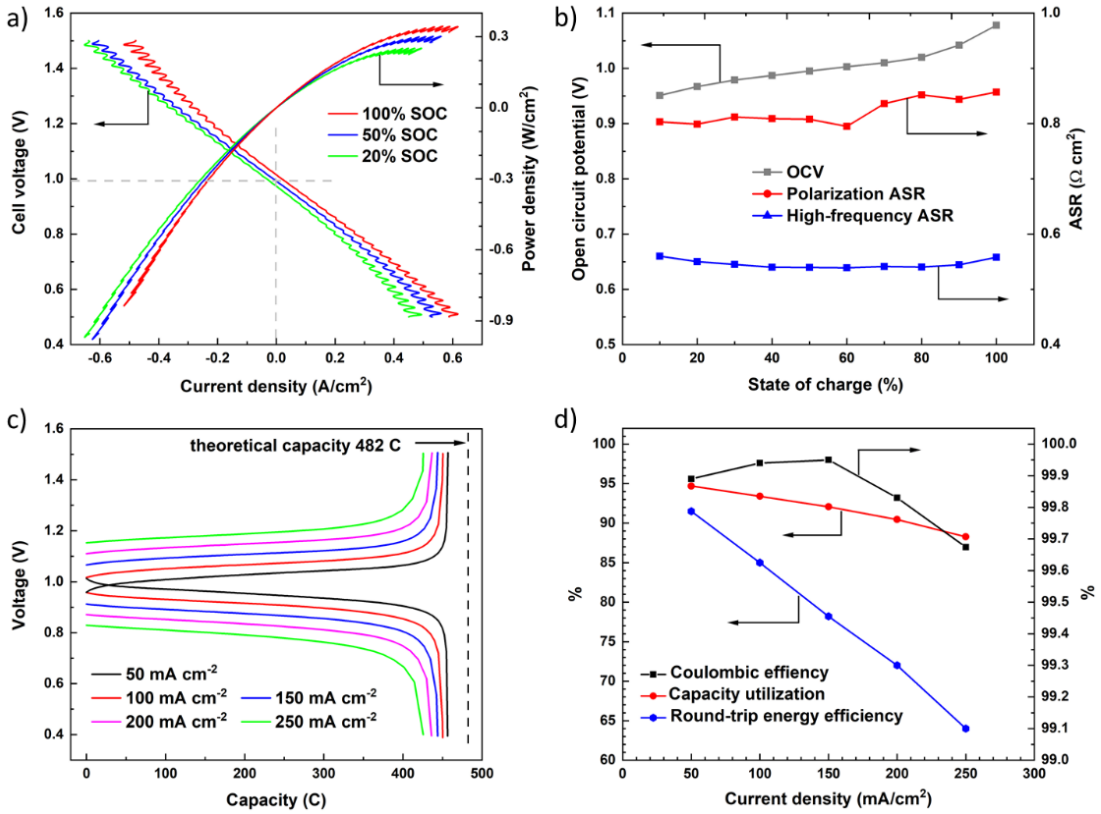

Figure 2.10 Polarization measurements of 0.5 M DPivOHAQ/ferrocyanide full cell at pH 12. a) Cell voltage vs. current density at room temperature at various SOC. b) OCV, high-frequency ASR and polarization ASR vs. SOC. c) Galvanostatic charge-discharge voltage profiles at various current densities. The vertical dashed line indicates the theoretical capacity. d) Capacity utilization, coulombic efficiency, and round-trip energy efficiency versus current density.

The same 0.5 M DPivOHAQ-ferrocyanide full cell was used for long-term stability evaluation (Figure 2.11). The cell was cycled at a constant current density of ±0.1 A cm^{-2}, and each galvanostatic half-cycle was followed by a potential hold at the voltage limit (1.3 V for charge, 0.6 V for discharge) until the current density fell below 2 mA cm^{-2} to mitigate the effect of temporal variations in accessible capacity during full cell cycling caused by drifts in cell resistance.[13] The charge-discharge profiles near the voltage limits (Figure 2.11b, c) are quite steep and are followed by small subsequent horizontal segments during

the potential holds. The horizontal segments end at 95.5% of theoretical capacity, but the steepness followed by a small subsequent horizontal segment of the charge-discharge profiles suggests that the electrolyte had around 4.5% inactive material and that the active material is undergoing deep cycling to essentially the full SOC limits. The cell was cycled for 690 cycles at 100 mA cm^{-2}, which required 15.6 days to complete. The capacity retention over the 690 cycles was 99.78% with an average coulombic efficiency greater than 99.9%, reflecting a capacity fade rate of 0.00031% per cycle or 0.014% per day (Figure 2.11a), i.e. 5.1% per year. This temporal fade rate is among the lowest exhibited by full cells in which organic molecules composed the capacity-limiting side: 2,6-DBEAQ fades at ~ 0.04%/day; 2,6-DPPEAQ fades at ~0.014%/day.[67]

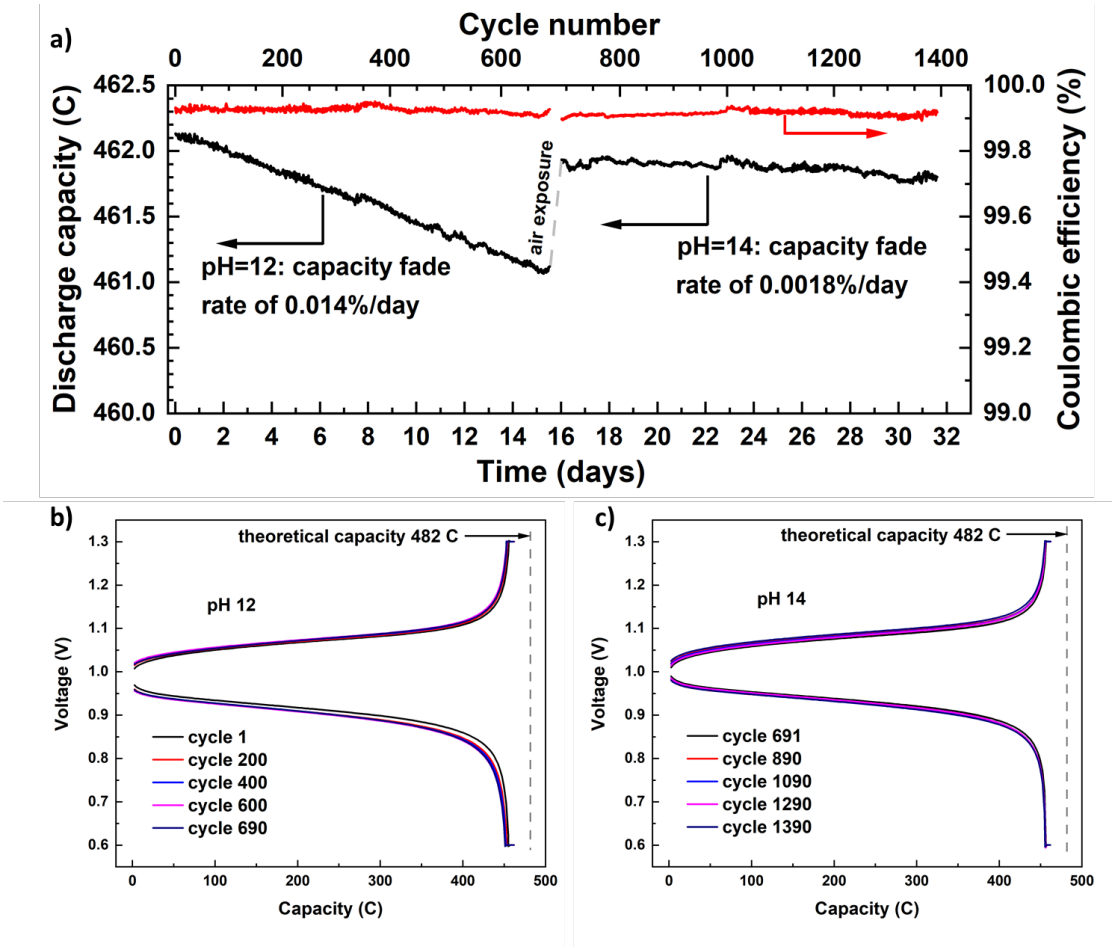

Figure 2.11 Cycling Performance of DPivOHAQ at pH 12 and 14. a) Coulombic efficiency and discharge capacity versus time and cycle number for a negolyte-limited DPivOHAQ/$K_4Fe(CN)_6$ full cell. Each 100 mA cm^{-2} half cycle was followed by a potentiostatic hold until the magnitude of the current density fell below 2 mA cm^{-2}. The negolyte comprised 5 mL of 0.5 M DPivOHAQ at pH 12, and the posolyte comprised 80 mL of 0.3 M potassium ferrocyanide and 0.1 M potassium ferricyanide at pH 12. After approximately 16 days of cycling, the negolyte was exposed to air and the pH of both negolyte and posolyte were adjusted to 14 before cycling for an additional 16 days. Note that the left y-axis represents 0.54% of the capacity of the DPivOHAQ negolyte. b) Charge-discharge voltage profile of DPivOHAQ from selected cycles at pH 12 in Figure 2.11a. c) Charge-discharge voltage profile of DPivOHAQ from selected cycles at pH 14 in Figure 2.11a.

After 15.6 days of cycling at pH 12, DPivOHAQ negolyte, in the discharged state, was exposed to air for 2 hours and the pH was adjusted to 14 by dissolving KOH pellets into

the negolyte and posolyte without changing cell materials or setup. As a result, 81% of the lost capacity was recovered, as shown in Figure 2.11a. Over the additional 16 days at pH 14, the cell exhibited a capacity fade rate of 0.0018%/day, which is 6 times lower than that at pH 12. The charge-discharge voltage profiles (Figure 2.11b, c) are almost invariant, indicating no apparent change in ohmic resistance and good chemical compatibility with the cell membrane and other cell components.[79] Based on the decomposition study of 2,6-DHAQ,[80] we attribute capacity fade to anthrone formation (Scheme 2.2). Therefore, increasing the hydroxide concentration should suppress the formation of anthrone. This expectation is consistent with the lower capacity fade rate observed at pH 14 than at pH 12. In general, the disproportionation reaction will generate OH^- (or consume H^+) at pH above the first pK_a of the anthrahydroquinone. Therefore, anthrone formation will be disfavored under alkaline conditions relative to acid conditions and will be progressively disfavored as the pH increases (Figure 2.12). We interpret the sudden increase in capacity at cycle 691 as the consequence of anthrone being converted back to anthraquinone by both the pH effect and the effect of exposure to atmospheric O_2.

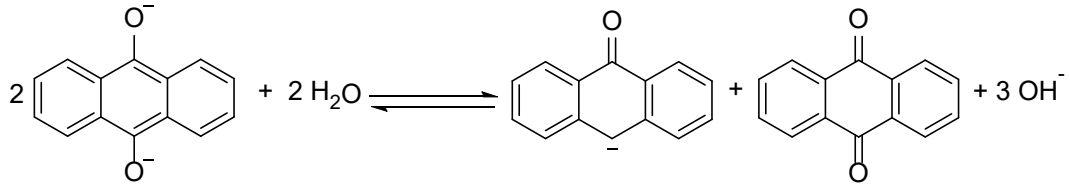

Scheme 2.2. The reversible disproportionation reaction of anthraquinone negolyte species under alkaline conditions. The pK_a of anthrone is reported[81] to be 10; therefore, anthrone is depicted in the deprotonated form at pH values between 12 and 14.[80]

Thermodynamics of the disproportionation reaction of anthraquinone is interpreted as follows. When the pH is between 12 and 14, both 9,10-dihydroxyanthracene (reduced anthraquinone) and anthrone (pK_a = 10) [81] are deprotonated, and the disproportionation reaction proceeds as follows:

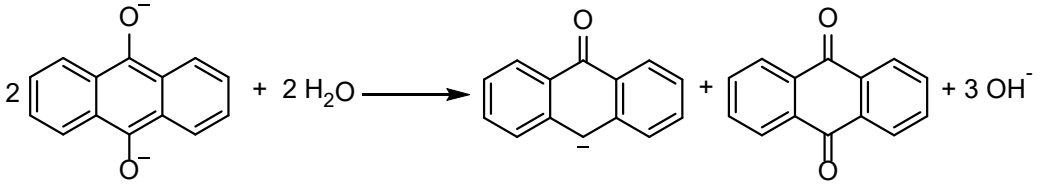

This disproportionation reaction is a combination of the following two half reactions:

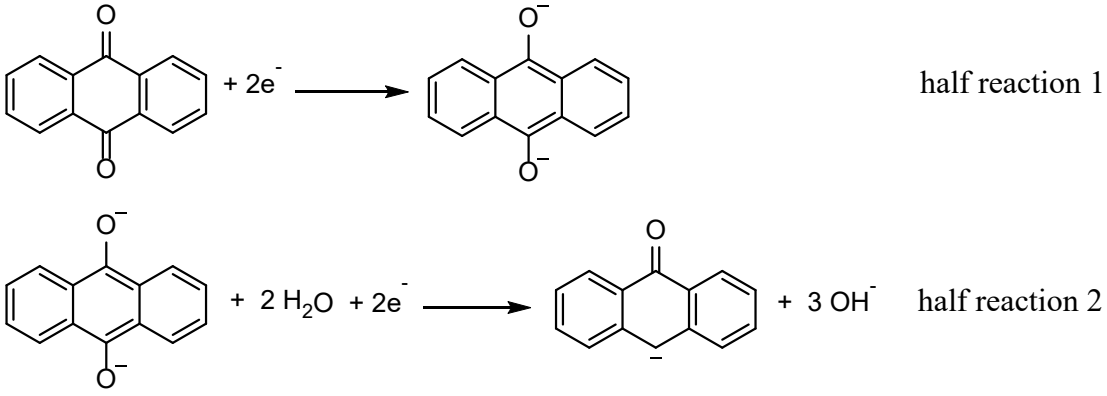

Within this pH range, the redox potential E_1 for half reaction 1 is pH independent, whereas the redox potential E_2 for the half reaction 2 decreases by approximately 89 mV per pH unit increase based on Nernst equation. The Gibbs free energy change ΔG per molecule of anthrone formed by the disproportionation reaction (half reaction 2 minus half reaction 1) is given by:

$$\Delta G = -2 \times F \times (E_2 - E_1) / N_A$$

assuming reactants and products (other than OH^-) have unit activities and the activity of

OH^- is consistent with the pH. As pH increases, the Gibbs free energy change ΔG increases, and the disproportionation reaction is less prone to happen. This observation is equivalent to the statement that the overall reaction within this pH range involves OH^-, so the activity of OH^- factors into the reaction quotient and equilibrium constant. By Le Chatelier's principle, the reaction will be disfavored as the pH increases.

When the pH is below the pK_{a1} (typically approximately 7) of 9,10-dihydroxyanthracene, the disproportionation reaction becomes:

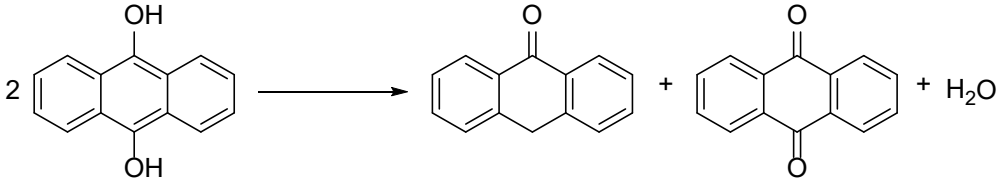

The two corresponding two half reactions are

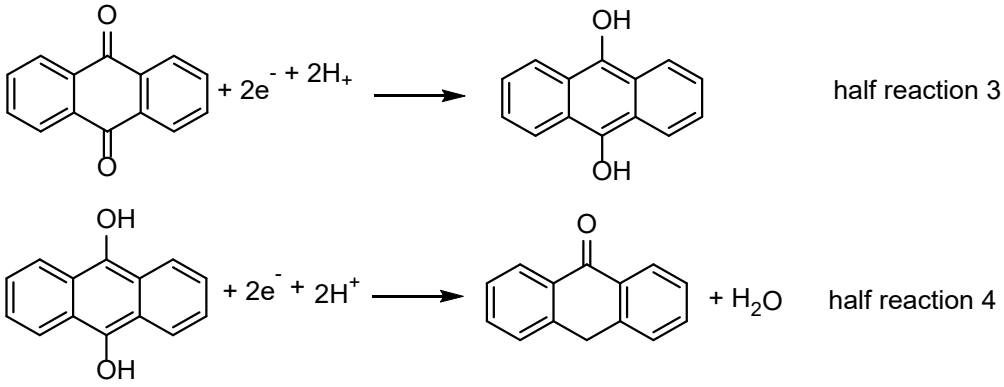

The redox potential E_3 for half reaction 3 decreases by approximately 59 mV per pH unit increase based on Nernst equation, and so does the redox potential E_4. The Gibbs free energy change $\Delta G'$ per molecule of anthrone formed by the disproportionation reaction (half reaction 4 minus half reaction 3) is given by:

$$\Delta G' = -2 \times F \times (E_4 - E_3) / N_A$$

assuming reactants and products (other than H^+) have unit activities and the activity of H^+ is consistent with the pH. As pH (below pK_{a1}) increases, the Gibbs free energy change $\Delta G'$ is constant. This observation is equivalent to the statement that the overall reaction within this pH range does not involve H^+, so the activity of H^+ does not factor into the reaction quotient and equilibrium constant.

If we draw a theoretical Pourbaix diagram for the two half reactions of the anthrone-forming disproportionation reaction according to Nernst equation (assuming that the pK_a of anthrone lies between the pK_{a1} and pK_{a2} of hydroquinone), we obtain:

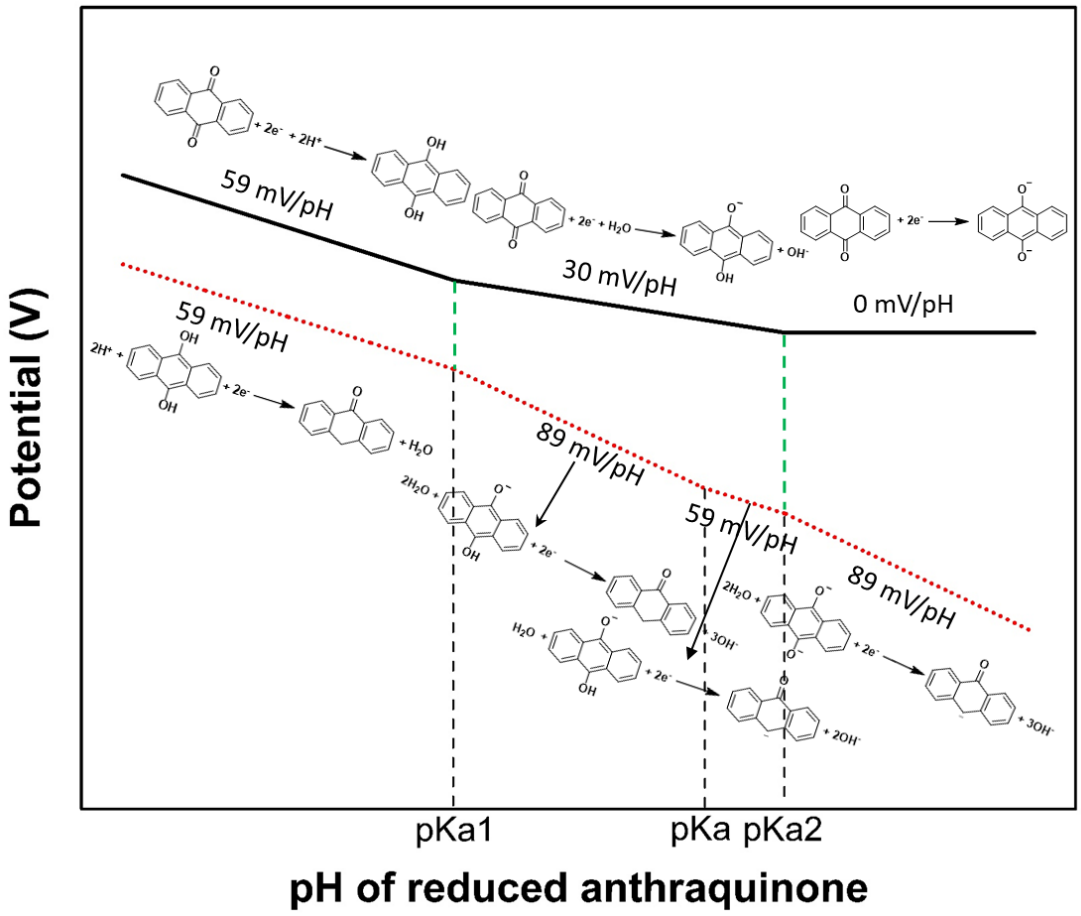

Figure 2.12 Representative Pourbaix diagram of anthraquinone, anthrahydroquinone, and anthrone. The pK_{a1} and pK_{a2} belong to the 9,10-dihydroxyanthracene (anthrahydroquinone). The pK_a (reported to be approximately 10) belongs to anthrone.[9] Here we assume that the pK_a of anthrone lies between the pK_{a1} and pK_{a2} of anthrahydroquinone.

This Pourbaix diagram illustrates that the Gibbs free energy change ΔG for the disproportionation reaction is larger at alkaline pH than at neutral or acidic pH. Therefore, anthrone formation is disfavored at alkaline pH relative to neutral or acidic pH. In real applications with a reasonable concentration of quinone, even starting at pH 7, the pH will increase to (or above) the pK_{a2} of 9,10-dihydroxyanthraquinone upon quinone reduction;

therefore, it is still possible to get a relatively stable anthraquinone negolyte starting at pH 7.

To confirm the major side reaction is the disproportionation of reduced anthraquinone, a fully reduced (~100% SOC) sample of DPivOHAQ at pH 12 was prepared and stored in an FEP vial in a glove box for 238 days, allowing the disproportionation to reach equilibrium. Indeed, some appreciable new peaks appeared in the ^{1}H NMR spectrum of the reduced DPivOHAQ, whereas upon re-oxidation in air, the ^{1}H NMR spectrum contained no observable decomposition peaks (Figure 2.13), indicating that the decomposition products can either be re-oxidized back to DPivOHAQ or are converted to other products with no observable signals above the detection limit of the NMR instrument. Therefore, high-performance liquid chromatography-mass spectrometry was performed to analyze both the reduced and the re-oxidized samples (Figure 2.14). The anthrone species was detected in the reduced sample but not in the re-oxidized sample, in agreement with the ^{1}H NMR result shown in Figure 2.13. In the re-oxidized sample after 238 days, approximately 1.24% of the signal corresponded to an anthrone dimer, suggesting a fade rate of 1.90%/year for reduced DPivOHAQ at pH 12 after aeration.

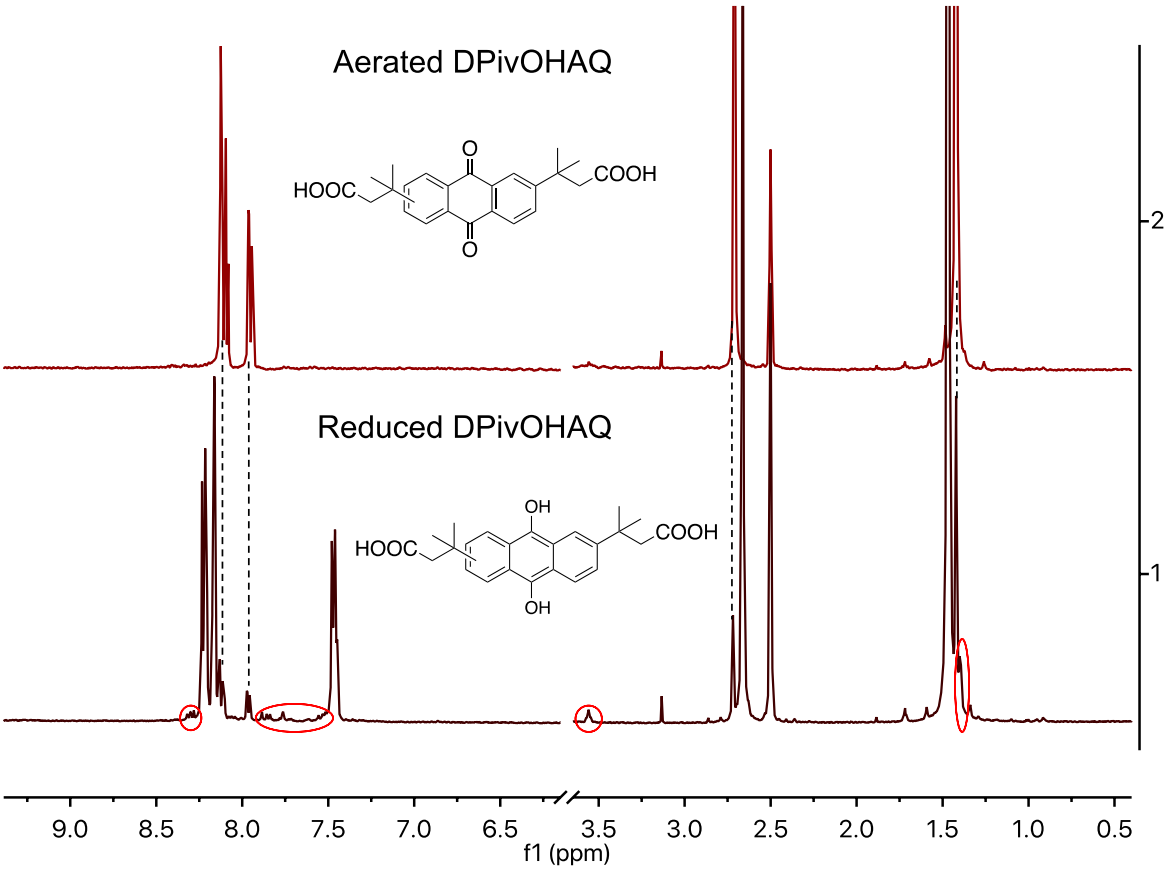

Figure 2.13 ^{1}H NMR spectra of the reduced and aerated DPivOHAQ in DMSO-d_6. Sample preparation: 5 mL of 0.1 M DPivOHAQ was fully charged to ~100% SOC and stored in a brown vial in a glovebox for 238 days. After that, an aliquot was taken and acidified with concentrated HCl to obtain the protonated and reduced DPivOHAQ precipitate after clear solution was removed. The protonated and reduced DPivOHAQ was re-dissolved in DMSO-d_6 and stored in a J. Young NMR tube for ^{1}H NMR spectrometry. The aerated sample was prepared by exposing the same reduced sample to air and shaking the NMR tube for several minutes before collecting the NMR spectrum. The ^{1}H NMR spectrum of the reduced sample revealed, in addition to peaks from reduced DPivOHAQ and a small amount of the oxidized form, some appreciable peaks highlighted with red circles, corresponding to signals from unknown compounds. However, these signals disappeared when the same NMR sample was aerated, indicating that the unknown compounds can either be oxidized back to DPivOHAQ or convert into other products with no observable signals above the detection limit of the NMR instrument.

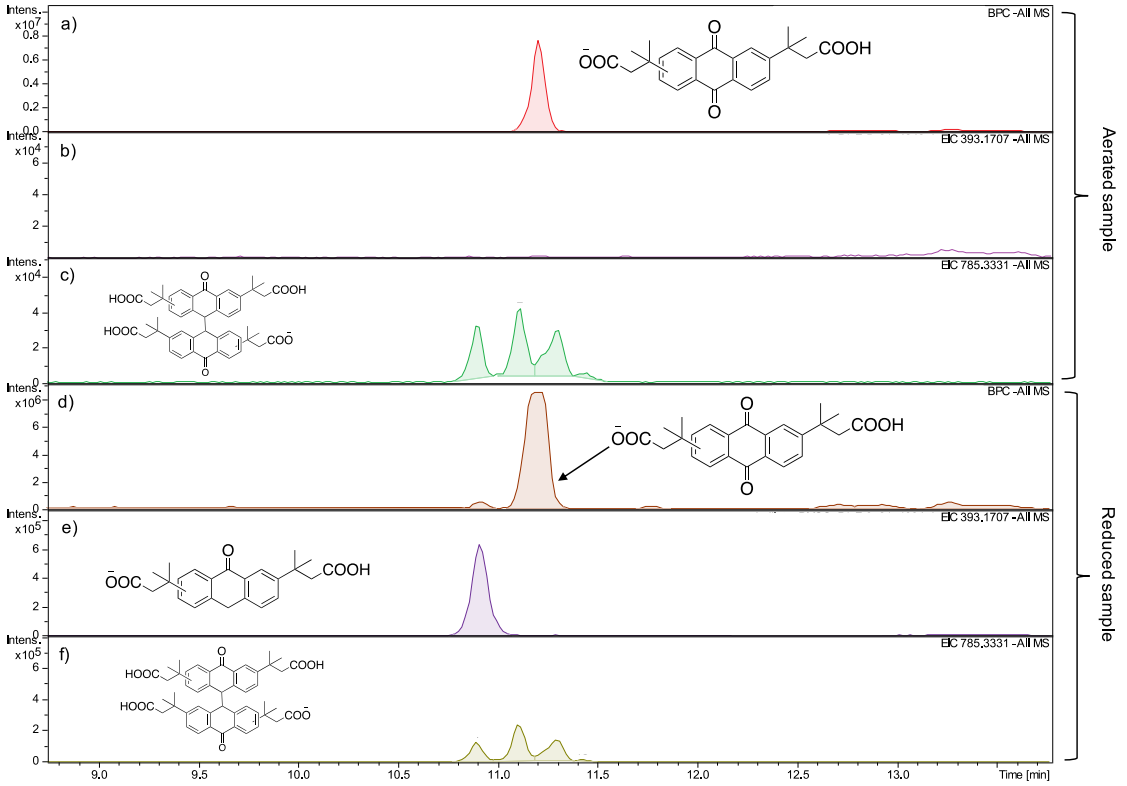

Figure 2.14 LC-MS results from the reduced DPivOHAQ samples stored for 238 days. a) The base peak chromatogram of the aerated sample. b) The extracted-ion chromatogram for the anthrone derivative from the aerated sample. c) The extracted-ion chromatogram for the anthrone dimer derivative from the aerated sample. d) The base peak chromatogram of the reduced sample. e) The extracted-ion chromatogram for the anthrone derivative from the reduced sample. f) The extracted-ion chromatogram for the anthrone dimer derivative from the reduced sample. In the reduced sample, both anthrone and anthrone dimer forms were detected. After aeration, no anthrone form is detected. The anthrone dimer accounts for 1.24% in the aerated sample, corresponding a fade rate of 1.90% per year for the reduced DPivOHAQ after aeration. Sample preparation: 5 mL of 0.1 M DPivOHAQ was fully charged to ~100% SOC and stored in a brown vial in a glovebox for 238 days. After that, aliquots were taken and acidified with concentrated HCl to obtain protonated DPivOHAQ precipitate after clear solution was removed. The protonated and reduced DPivOHAQ was re-dissolved in DMSO. The resulting solution was further diluted to the desired concentration (10-20 μM) by acetonitrile/water co-solvents (V/V=1:1). One sample was stored in a glovebox in the reduced form prior to the LC-MS measurement, whereas another sample was intentionally aerated. After that, the two samples were immediately subjected to the LC-MS experiment.

Goulet and Tong *et al.* showed that, by avoiding high SOC, the anthrone formation rate in 2,6-DHAQ decreased substantially.[80] They also demonstrated recovery of most of the lost capacity by air exposure. Because DPivOHAQ also decomposes via anthrone formation, we hypothesize that similar approaches will extend its lifetime significantly. We predict that a flow cell with decades-long calendar life should be achievable with DPivOHAQ at pH 12.

Another anthraquinone, DBAQ, with higher solubility, was synthesized (Figure 2.15) using a similar strategy. The first step is a Friedel–Crafts acylation, followed by Wolff-Kishner reduction of the carbonyl groups to methylene. The last step is oxidation of the corresponding anthracene (or 9,10-dihydroanthracene) to the final anthraquinone form. Compared to the three steps for DPivOHAQ synthesis, four steps are required for DBAQ synthesis when starting from anthracene. Because of the low cost of succinic anhydride and given that the Wolff–Kishner reduction is well-developed in industry, the cost of DBAQ could also be low. Electrochemical kinetics studies of DBAQ were conducted by RDE techniques as shown in Figure 2.16a. The diffusion coefficient of the oxidized form of DBAQ was determined by Levich analysis (Figure 2.16b) to be 2.5×10^{-6} cm^2/s. According to the Koutecký-Levich equation and Tafel plot, the charge transfer coefficient is 0.50, and the kinetic rate constant is 2.9×10^{-3} cm/s, which is slightly higher than that of DPivOHAQ.

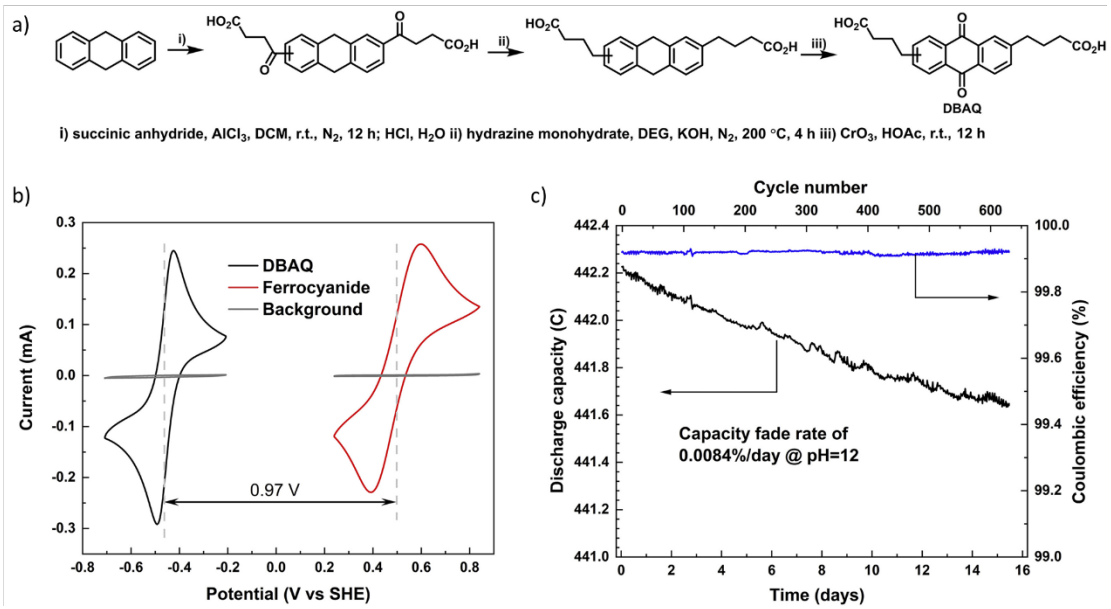

Figure 2.15 DBAQ Synthesis and Electrochemistry. a) Synthetic route for DBAQ; b) Cyclic voltammograms of 5 mM DBAQ and 10 mM potassium ferrocyanide at pH 12 with a scan rate of 100 mV/s; c) Coulombic efficiency and discharge capacity versus time and cycle number for a negolyte-limited DBAQ/$K_4Fe(CN)_6$ full cell. The cell was cycled galvanostatically at 100 mA cm^{-2} between 0.4 and 1.3 V with SGL 39AA carbon electrodes, and each half cycle was followed by a potentiostatic hold until the magnitude of the current density fell below 2 mA cm^{-2}. The negolyte comprised 5 mL of 0.5 M DBAQ at pH 12, and the posolyte comprised 80 mL of 0.3 M potassium ferrocyanide and 0.1 M potassium ferricyanide at pH 12. Note that the left y-axis represents about 0.32% of the capacity of the DBAQ negolyte.

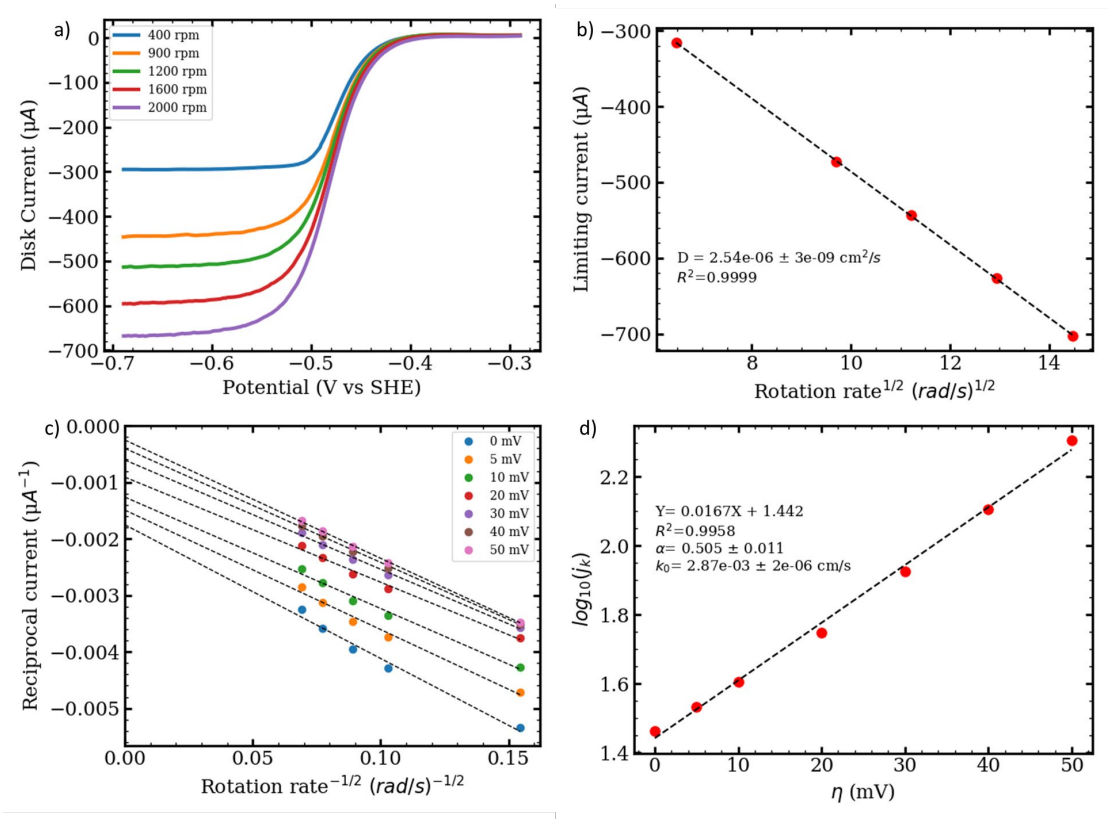

Figure 2.16 RDE test for DBAQ. a) Linear sweep voltammograms of 5 mM DBAQ in 1 M KCl at pH 12 on a glassy carbon electrode at rotation rates between 400 and 2000 rpm. b) Levich plot (limiting current versus square root of rotation rate in rad/s) of 5 mM DBAQ in 1 M KCl at pH 12. Limiting current is taken as the current at -0.65 V in (a). The slope yields a diffusion coefficient for the oxidized form of DBAQ of 2.54 × 10^{-6} cm^2 s^{-1}. c) Koutecky-Levich plot (reciprocal current versus inverse square root of rotation rate in rad/s) of 5 mM DBAQ in 1 M KCl at pH 12. d) Fitted Tafel plot of 5 mM DBAQ in 1 M KCl at pH 12. The charge transfer coefficient is calculated to be 0.50, and the rate constant is calculated to be 2.87 × 10^{-3} cm s^{-1}.

The solubility of DBAQ was determined to be 1.0 M at pH 12, corresponding to a volumetric capacity of 53.6 Ah/L for the negolyte. The reduction potential is -0.47 V versus SHE at pH 12. When paired with potassium ferrocyanide, a full cell of approximately 0.97 V can be achieved. To evaluate the stability of a DBAQ negolyte, a full cell was assembled with 5 mL of 0.5 M DBAQ negolyte at pH 12 as the capacity limiting side and a posolyte

comprising 80 mL of 0.3 M $K_4Fe(CN)_6$ with 0.1 M $K_3Fe(CN)_6$ at pH 12 as the non-capacity-limiting side. The flow cell was constructed from graphite flow plates and carbon paper electrodes, separated by a Fumasep E-620 (K) membrane. The cell exhibited 91.7% of its theoretical capacity. It was cycled for 650 cycles at 100 mA cm^{-2}, which required 15.5 days to complete. The average capacity fade rate was 0.0084%/day, corresponding to 3.1%/year. Assuming the capacity fade is primarily due to anthrone formation then, with careful control of the pH and SOC of the DBAQ electrolyte and periodic exposure to air, DBAQ should exhibit an even lower loss rate in real-world applications.

2.4 In situ electrosynthesis anthraquinone

In previous section, DPivOHAQ was synthesized by three steps with a final chemical oxidation method. However, the use of CrO_3 in the synthesis can be highly toxic and explosive if produced in large scale. Here, we showed DPivOHAQ could be synthesized by electrochemical oxidizing DPivOHAc as shown in Figure 2.17. The DPivOHAC powder was dissolved in water by adding KOH to deprotonate the carboxylic acid groups, then a high oxidation potential was applied to oxidize the anthracene to anthraquinone. The electrochemical oxidation method eliminates the further purification, therefore, further decrease the synthetic cost. Figure 2.17b illustrates how DPivOHAQ and ferrocyanide active species can be produced *in situ* in the flow cell's electrosynthesis mode. These materials can directly serve as the active species in the negolyte and the posolyte, respectively, of a flow battery in the same cell as illustrated in Figure 2.17c.

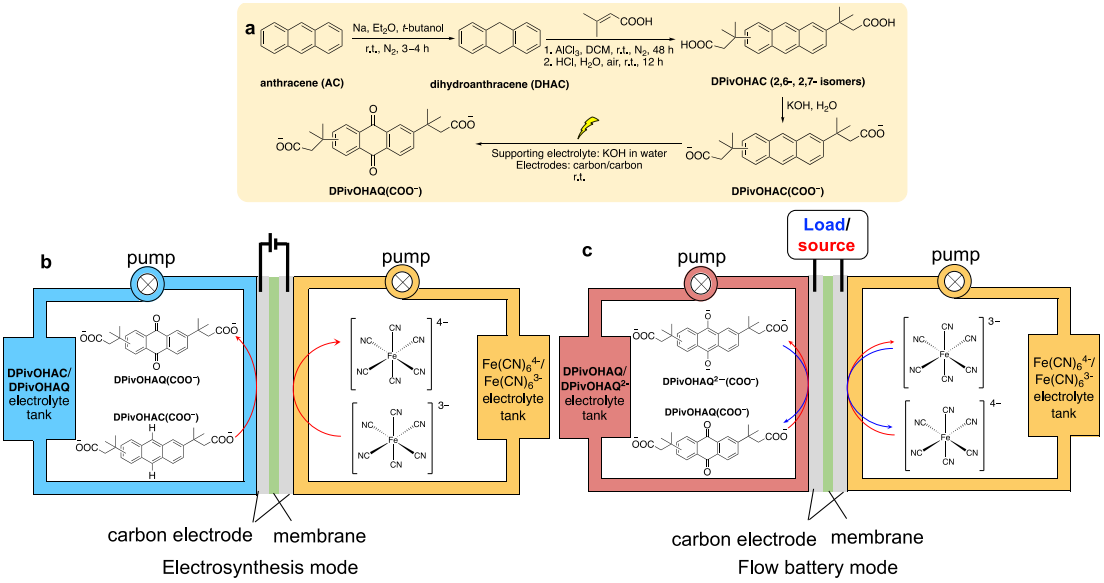

Figure 2.17 Preparation of DPivOHAQ and the corresponding flow battery. (a) The DPivOHAQ synthetic route and conditions starting from anthracene. (b) The setup for electrosynthesis of DPivOHAQ and ferrocyanide. (c) The flow battery setup with DPivOHAQ negolyte (generated *in situ*) and ferrocyanide posolyte (generated *in situ*).

Figure 2.18a lists three different oxidation methods for DPivOHAQ synthesis. Conventionally, anthracene derivatives can be chemically oxidized to their anthraquinone forms by oxidants such as chromium oxide (CrO_3) in strong acidic media at elevated temperature. To minimize the use of hazardous oxidants, the strategy of mediated electrochemical oxidation can be performed by regenerating oxidants such as cerium(IV) compounds.[82, 83] However, in both of these thermochemical and indirect electrochemical oxidation processes, tedious and expensive isolation of anthraquinone-based products from oxidants and acids is required. Taking advantage of the high solubility of DPivOHAC in base, we demonstrate a synthetic route via direct electrochemical oxidation in alkaline electrolyte with a flow cell. This method allows the complete elimination of hazardous

oxidants and costly separation processes.

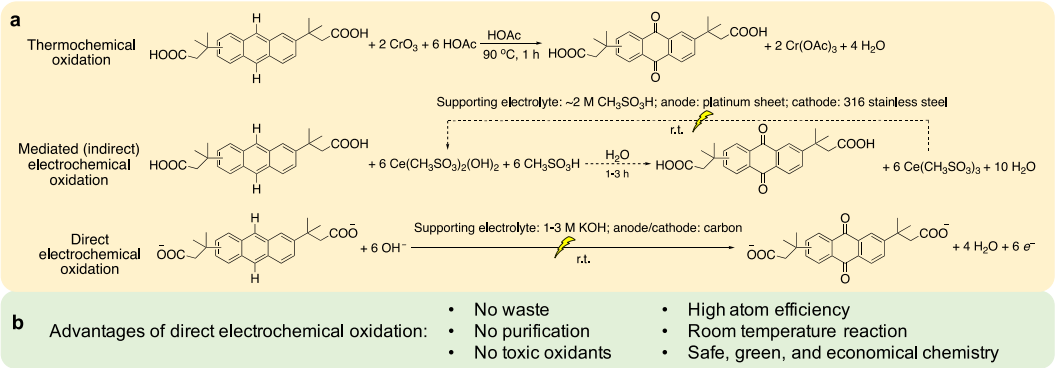

Figure 2.18 Comparison of DPivOHAQ synthetic methods. (a) Thermochemical, mediated (indirect) electrochemical, and direct electrochemical oxidation reactions to synthesize DPivOHAQ. (b) Advantages of direct electrochemical oxidation *in situ*.

Glassy carbon was used as the working electrode for all three-electrode cyclic voltammetry (CV) tests with a 5 mm diameter glassy carbon working electrode, an Ag/AgCl reference electrode (BASi, pre-soaked in 3 M NaCl solution), and a graphite counter electrode. Both undivided cell and divided cell were built for electrosynthesis. Flow battery experiments were constructed with cell hardware from Fuel Cell Tech (Albuquerque, NM) assembled into a zero-gap flow cell configuration. Pyrosealed POCO graphite flow plates with serpentine flow patterns were used for both electrodes. Each electrode comprised a 5 cm^2 geometric surface area covered by AvCarb HCBA woven carbon fiber without pretreatment, or Pt-coated Toray carbon paper without pretreatment. The membrane is pre-soaked (1 M KOH for 24 hours) Nafion 212.

Undivided electrolytic cell setup (electrochemical oxidation vs. the HER)

Working electrode: carbon felt, where DPivOHAC was oxidized to DPivOHAQ; counter

electrode: carbon rod, where water was reduced to hydrogen gas. While the electrolyte was stirred, a constant potential (1.1 V vs. Ag/AgCl) was applied to the divided electrolytic cell until 120% of the required coulombs were extracted from the working electrode.

Divided electrolytic cell setup (electrochemical oxidation vs. the ORR)

Anode: Commercial AvCarb HCBA (woven carbon cloth), where DPivOHAC was oxidized to DPivOHAQ; cathode: platinum coated Toray carbon paper, where humidified air/oxygen was reduced to hydroxide. A constant voltage (1.8 V) was applied to the divided electrolytic cell until the current decreased to 2 mA/cm^2. The number of extracted electrons was ~1.2 times higher than the theoretical value.

Divided electrolytic cell setup (electrochemical oxidation vs. the reduction of ferricyanide)

Anode: AvCarb HCBA (woven carbon cloth), where DPivOHAC was oxidized to DPivOHAQ; cathode: AvCarb HCBA (woven carbon cloth), where potassium ferricyanide was reduced to potassium ferrocyanide. A constant current density (20 mA/cm^2) was applied to the divided cell for at most 1.5 hours with a 1.2 V voltage cutoff; when either time or voltage reached the limit, the potential was held (1.2 V vs. ferro-/ferricyanide) until the current decreased to 2 mA/cm^2. The number of extracted electrons was ~1.2 times higher than the theoretical value.

For characterization, an aliquot (~250 μL) was transferred from the as-prepared

anolyte to an Eppendorf® tube (capacity: 1.5 mL) and acidified by a drop of concentrated HCl to obtain DPivOHAQ precipitate. The final DPivOHAQ precipitate was re-dissolved in DMSO-d_6 for ^{1}H NMR measurement. The yield was determined by peak integrations of spectrum. Faradaic efficiency (%) = yield (%) / 1.2.

In an electrolytic cell, an anodic oxidation half reaction must be accompanied by a cathodic reduction half reaction. As shown in Table 2.2, we devise three different reduction half reactions to be coupled with direct DPivOHAC electrochemical oxidation, *i.e.*, the hydrogen evolution reaction (HER), the oxygen reduction reaction (ORR), and the $Fe(CN)_6^{3-}$ to $Fe(CN)_6^{4-}$ reduction reaction. The corresponding oxidation or reduction potentials for these reactions are listed in Table 2.2.

For the electrochemical oxidation of DPivOHAC to DPivOHAQ, two cell types are used. A divided cell uses an ion exchange membrane to separate the two half reactions, resembling the architecture of traditional fuel cells and ARFBs. An undivided cell employs two electrodes suspended in electrolyte without the use of a membrane, reflecting a bulk electrolysis cell.

Comparing these three overall reactions, the first one paired with the HER requires the highest voltage; the second one paired with the ORR is known to have slow reaction kinetics and a high overpotential;[84] the third one paired with $Fe(CN)_6^{3-}$ to $Fe(CN)_6^{4-}$ reduction exhibits the lowest overall reaction cell voltage, suggesting the least amount of energy will be required for electrosynthesis. Another merit of the third reaction is the *in*

situ generation of the desired negolyte active species (DPivOHAQ) and posolyte active species $Fe(CN)_6^{4-}$ simultaneously. The disadvantage is that at least six equivalents of ferricyanide and hydroxide have to be consumed. Given the similar reduction potentials of ORR and ferricyanide to ferrocyanide, we expect that one equivalent of oxygen and two equivalents of ferricyanide can be concurrently reduced on cathode, achieving high yields as well as lower chemical cost. By using the same full cell configuration without changing electrolyte reservoirs, carbon-based electrodes, or ion-exchange membranes, we can immediately switch from electrosynthesis mode to flow battery mode for electrochemical energy storage. In this configuration, neither hazardous oxidants nor purification steps are needed, nor is waste generated. Furthermore, the reaction may proceed at room temperature with high atom efficiency. The new synthesis is therefore potentially safe, green, economical, and scalable.

Table 2.2 Anodic, cathodic, and overall reactions for electrochemical oxidation.

	Reactions	Potential at pH 14 (V vs SHE) / Cell voltage (V)
Anodic	**DPivOHAC(COO^-)** + 6 OH^- ⟶ **DPivOHAQ(COO^-)** + 4 H_2O + 6 e^-	1.14*
Cathodic	6 H_2O + 6 e^- ⟶ 3 H_2 + 6 OH^- (divided or undivided cell)	–0.83
	1.5 O_2 + 6 e^- + 3 H_2O ⟶ 6 OH^- (divided or undivided cell)	0.40
	6 $Fe(CN)_6^{3-}$ + 6 e^- ⟶ 6 $Fe(CN)_6^{4-}$ (divided cell)	0.44
Overall	**DPivOHAC(COO^-)** + 2 H_2O ⟶ **DPivOHAQ(COO^-)** + 3 H_2	1.97
	DPivOHAC(COO^-) + 1.5 O_2 ⟶ **DPivOHAQ(COO^-)** + H_2O	0.74
	DPivOHAC(COO^-) + 6 OH^- + 6 $Fe(CN)_6^{3-}$ ⟶ **DPivOHAQ(COO^-)** + 6 $Fe(CN)_6^{4-}$ + 4 H_2O	0.70

*: The electro-oxidation potential at peak current

The cyclic voltammogram (CV) of DPivOHAC at pH 14 (Figure 2.19a) indicates a

peak oxidation current at 1.14 V vs. SHE. This value is more positive than the standard redox potential of 0.40 V vs. SHE for the oxygen evolution reaction (OER), and we expect that the OER will be a major side reaction of electrosynthesis.

We then assembled a flow cell with DPivOHAC as the anolyte and $K_3Fe(CN)_6$ as the catholyte. Galvanostatic electrolysis with a potentiostatic hold after reaching a potential limit of 1.2 V was performed for ~4.5 hours to complete the electrosynthesis. The OER side reaction, evidenced by the observation of bubbles generated in the anolyte, precludes a faradaic efficiency of 100%. Thus, the number of electrons extracted from the anolyte was ~1.2 times higher than the theoretical number for complete conversion. A plateau appears at ~0.8 V against $K_3Fe(CN)_6$ (0.44 V vs. SHE) in the voltage profile (Figure 2.19b).

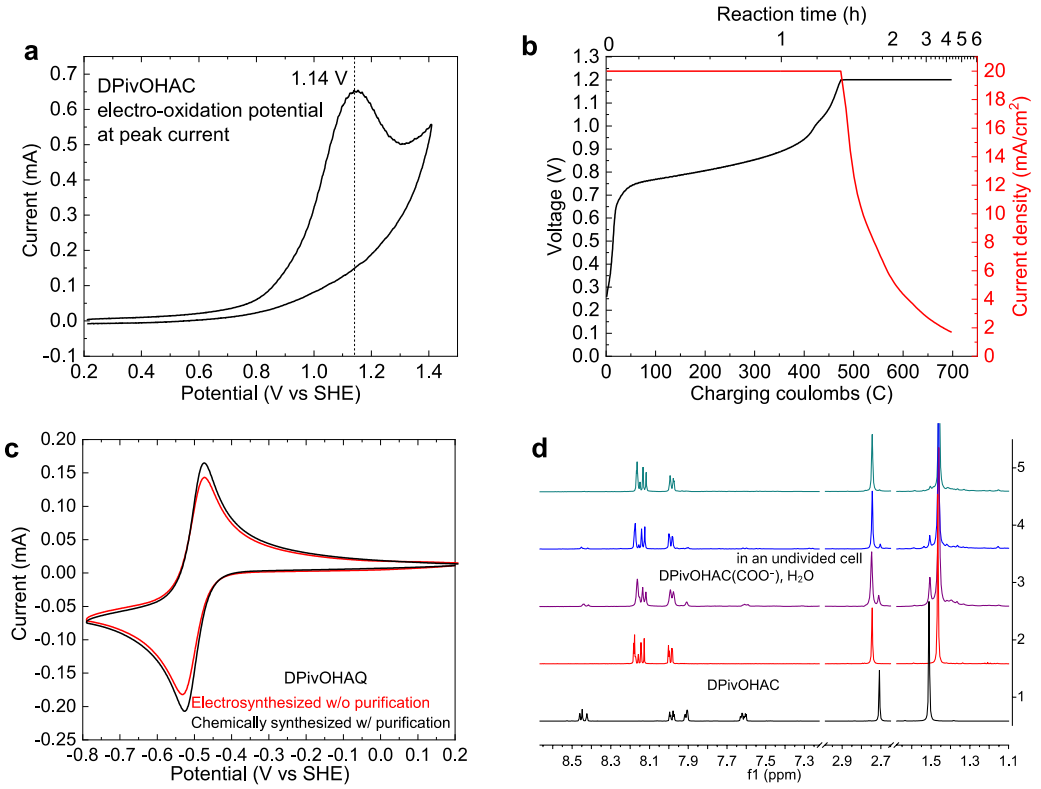

Figure 2.19 Electrosynthesis and characterization of DPivOHAQ. (a) The cyclic voltammogram (CV) of 0.1 M DPivOHAC in 1.0 M KCl + 1.0 M KOH aqueous solution. Scan rate: 0.1 V/s. b) The electrochemical oxidation of DPivOHAc. (c) CV of 10 mM electrosynthesized DPivOHAQ without purification and 10 mM chemically synthesized DPivOHAQ with purification, respectively. Scan rate: 0.1 V/s. (d) ^{1}H NMR spectra of (bottom to top): chemically synthesized DPivOHAC (black) and DPivOHAQ (red); electrosynthesized DPivOHAQ in an undivided cell (purple), 17.3% of DPivOHAC remained unreacted according to the integration, yield: 82.7%; electro-synthesized DPivOHAQ in a divided cell against $Fe(CN)_6^{3-}$ (blue), 7.0% of DPivOHAC remained unreacted according to the integration, yield: 93.0%; electro-synthesized DPivOHAQ in a divided cell against O_2 (green), 0 % of DPivOHAC remained unreacted according to the integration, yield: 100%. The solvent peaks (DMSO and H_2O) were removed to better display the peaks of interest.

We compared the CV of DPivOHAQ produced by electrosynthesis against the reduction of $Fe(CN)_6^{3-}$ to that of the chemically synthesized product at the same concentration to verify that the reaction products are the same regardless of the synthetic

procedure employed (Figure 2.19c). The two CV curves show identical redox peaks and similar peak currents, indicating a high-yield electrosynthesis process. ^{1}H nuclear magnetic resonance (NMR) spectroscopy was used to further examine the structure of electrosynthesized DPivOHAQ when using either a divided or undivided cell and to compare the spectra with those of the starting material, DPivOHAC, and the chemically synthesized DPivOHAQ. The top three spectra in Figure 2.19d are the ^{1}H NMR spectra from electrosynthesized DPivOHAQ, in which the dominating peaks have the same chemical shifts as those in the spectrum of chemically synthesized DPivOHAQ, further suggesting the desired product was achieved.

Slightly different yields of DPivOHAQ were obtained when paired with the HER in an undivided cell or with $Fe(CN)_6^{3-}$ reduction or the ORR in a divided cell. The 82.7% yield when paired with the HER in an undivided cell could be explained by a molecular shuttling effect; *i.e.*, the electrosynthesized DPivOHAQ can first migrate to the cathode where it is reduced, then diffuse back to the anode for re-oxidation. As a result, double counting of electrons can occur. When paired with the $Fe(CN)_6^{3-}$ reduction half reaction, a yield of 93.0% was obtained. The incomplete yield is likely due to the consumption and therefore decreased concentration of both DPivOHAC and OH^- as the electrosynthesis continues, making further oxidation increasingly difficult.

The use of the ORR half reaction achieved almost 100.0% yield. This exceptional yield may be attributed to the as-formed OH^- ions on the cathode (ORR) side crossing over

to the anolyte and compensating for any loss of OH^- ions on the anode side. Overall yields in excess of 80.0% for all three conditions exceed many conventional reactions and are acceptable for direct flow battery use without purification or separation.

To demonstrate that the electrochemical oxidation can be applied to other anthracene derivatives, we performed electrochemical oxidation of DBDHAC, where the molecular core is 9,10-dihydroanthracene.[85] The ^{1}H NMR results indicate that DBDHAC can, like DPivOHAC, be electrochemically oxidized to the final anthraquinone (Figure 2.20), DBAQ, which has also been shown to be extremely stable.[85]

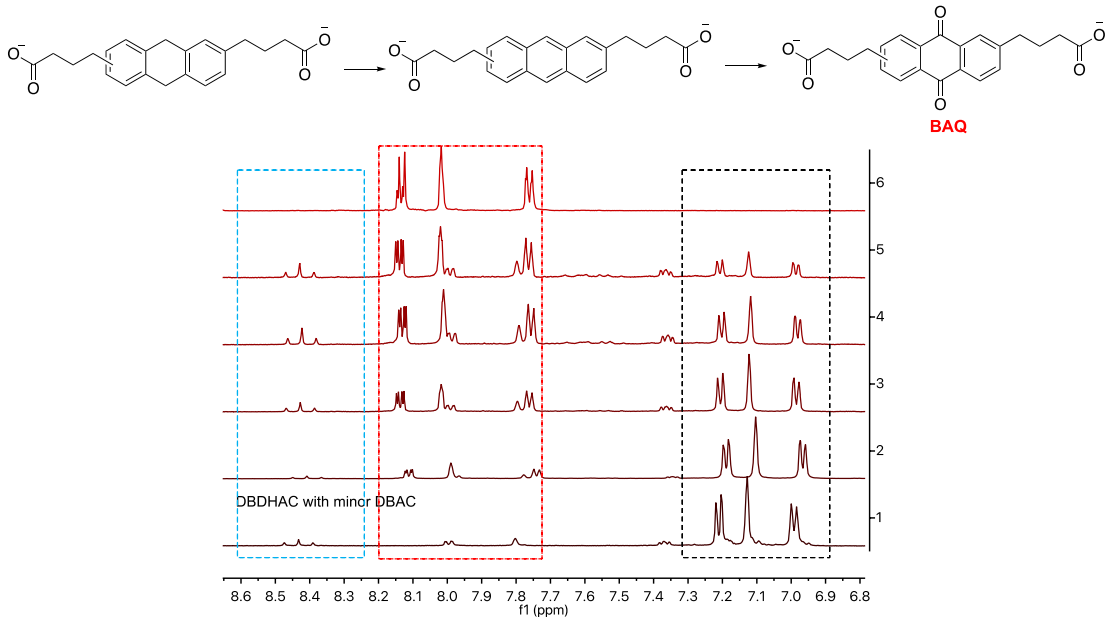

Figure 2.20 ^{1}H NMR spectra of DBDHAC (bottom), chemically synthesized DBAQ (top), and electrochemically synthesized DBAQ in an undivided cell after varying extents of reaction. DBDHAC: 4,4'-(9,10-dihydroanthracene-diyl)dibutanoic acid; DBAC: 4,4'-(anthracene-diyl)dibutanoic acid; DBAQ: 4,4'-(9,10-anthraquinone-diyl)dibutanoic acid. The time interval between successive measurements labeled electrochemical oxidation-1, 2, 3, and 4 is approximately one hour. The deuterated solvent is DMSO-d_6.

2.5 Conclusions

In this report, we have demonstrated a new route to synthesize water-soluble anthraquinones with solubilizing groups attached by carbon-carbon bonds, starting from potentially inexpensive 9,10-dihydroanthracene. Two of these anthraquinones exhibit high aqueous solubilities and low capacity fade rates of 0.0084%/day or 0.014%/day at pH 12. We demonstrated in a full cell containing a DPivOHAQ negolyte that anthrone formation is the major side reaction responsible for capacity fade and that air exposure can recover most of the lost capacity. Furthermore, by increasing the pH of the negolyte to 14, we reduced the DPivOHAQ capacity fade rate to an extremely low value of less than 1%/year. We expect that the stability of DPivOHAQ and DBAQ can be even further improved with careful control of the battery operating conditions. We suggest that strategies combining SOC limit control, precision air exposure, and pH tuning can be extended to other inexpensive anthraquinone molecules to achieve extremely low-capacity fade rates. Furthermore, we developed an *in-situ* electrosynthetic method to further decrease the synthetic cost. These optimized anthraquinone-based RFBs will be able to store the massive amounts of electrical energy needed to stabilize the variable wind and solar sources that must supply our future electric grid.

Chapter 3. Potentially Low-Cost, Stable Anthraquinone Electrolytes for Aqueous Redox Flow Batteries

Authorship

The following work has been adapted from the submitted manuscript "High-Performance Anthraquinone with Potentially Low Cost for Aqueous Redox Flow Batteries" written by Min Wu, Dr. Meisam Bahari, Prof. Roy G. Gordon, and Prof. Michael J. Aziz. Wu conducted the chemical synthesis, chemical characterization, electrochemical measurements such as CV and long cycling test for the low concentration cell, and wrote the manuscript. Bahari performed the polarization test and long cycling test of high concentration cell, as well as reviewed and revised the manuscript. Gordon advised the materials synthesis and reviewed the manuscript. Aziz advised the battery test, reviewed and revised the manuscript.

3.1 Introduction

Bulk electrical energy storage technologies have attracted great attention because of their capability to address the intrinsic intermittency of renewable energy sources such as solar and wind electricity.[6, 12, 67] Aqueous redox-flow batteries are particularly attractive for grid-scale energy storage owing to their flexible architecture, long cycle life, and good safety features.[67] Aqueous vanadium RFBs are the most commonly studied and adopted

system, but their widespread application is hindered by the availability and the fluctuating price of vanadium.[11, 12, 67] In contrast, redox-active organics comprising earth-abundant elements such as C, H, O, and N are potentially inexpensive alternatives to vanadium.[22, 86, 87] Redox-active organics based on quinone,[49, 58, 60, 62, 65, 66, 68, 79, 85, 88-91] viologen,[39, 40, 92-98] phenazine,[63, 99-101] alloxazine,[61] and (2,2,6,6-tetramethylpiperidin-1-yl)oxyl[92, 93, 99, 102-106] derivatives have been studied for aqueous redox flow batteries. However, only a few anthraquinone,[65, 66, 85] phenazine,[101] and viologen[40, 95, 96, 98] derivatives have demonstrated very good long-term stability; others tend to have poor chemical stability. Viologens are vulnerable to attack by both protons and hydroxide, making their practical implementation difficult, as a small amount of a side reaction, e.g. with air leaking into the system, can lead to a large deviation from neutral pH.[40, 98] Recently, phenazine derivatives have also been reported to be extremely stable; however, they suffer from high synthetic cost because expensive phenazine precursors, precious metal catalysts, and ligands are used for the synthesis.[101] All of the extremely stable anthraquinones reported to date also suffer from high chemical cost issues due to a multi-step synthesis or expensive precursors.[65, 66, 85] Developing inexpensive, stable, and soluble redox-active organics remains crucial for the practical implementation of aqueous organic redox flow batteries (AORFBs).

Here, we report a potentially low-cost and highly soluble anthraquinone negolyte with good cycling stability. The anthraquinone 1,8-dihydroxy-2,7-dicarboxymethyl-9,10-anthraquinone (DCDHAQ) was synthesized from the relatively inexpensive precursor 1,8-

dihydroxyanthraquinone (1,8-DHAQ) with a one-pot, green synthesis method with water as the solvent. The solubility of DCDHAQ at pH 14 is 1.3 M, corresponding to a volumetric capacity of 69.7 Ah/L, which is more than 15 times that of its precursor (0.08 M). The redox potential of DCDHAQ in 1M KOH is -0.56 V vs. SHE; pairing with ferrocyanide, it enables a full cell voltage of 1.1 V. With this simple $–CH_2CO_2^-$ functionalization, the average capacity fade rate decreases from 13%/day for 1,8-DHAQ[89] to less than 0.1%/day for DCDHAQ under the most favorable conditions. Moreover, the cost at mass-production scale is estimated to be of the order of $5/kg, potentially leading to a competitive flow battery chemistry. The functionalization raises aqueous solubility, decreases molecular crossover rates, and greatly increases the cycling stability of anthraquinones, providing guidance for the rational design of redox-active organics for low cost and ultra-stable cycling performance.

3.2 Experimental section:

Materials: 1,8-dihydroxyanthraquinone (96%), 1,4-dihydroxyanthraquinone (98%) were purchased from Sigma Aldrich. 50 wt. % glyoxylic acid solution was purchased from Acros Organics. All chemicals were used as received.

3.2.1 Synthesis of DCDHAQ

3 g of 1,8-dihydroxyanthraquinone (12.49 mmol) was added to 100 mL 0.1 M NaOH solution. The mixture was stirred at room temperature for 0.5 h under nitrogen. A portion

of $Na_2S_2O_4$ (2.39 g, 13.74 mmol) was added to the mixture to give an orange-red solution. Then an aqueous solution of glyoxylic acid (50%, 3 eq.) was added to the above mixture. The solution was stirred at room temperature for 1 hour. Afterward, another portion of $Na_2S_2O_4$ (2.28 g, 13.1) mmol was added to the solution. The temperature was increased to 80 °C, held for 0.5 h, cooled to room temperature and exposed to air. The solution was subsequently acidified with 2 M HCl to collect the crude solid. The crude compound was washed with DMSO to give an orange solid. Yield: 3.1 g (70%).

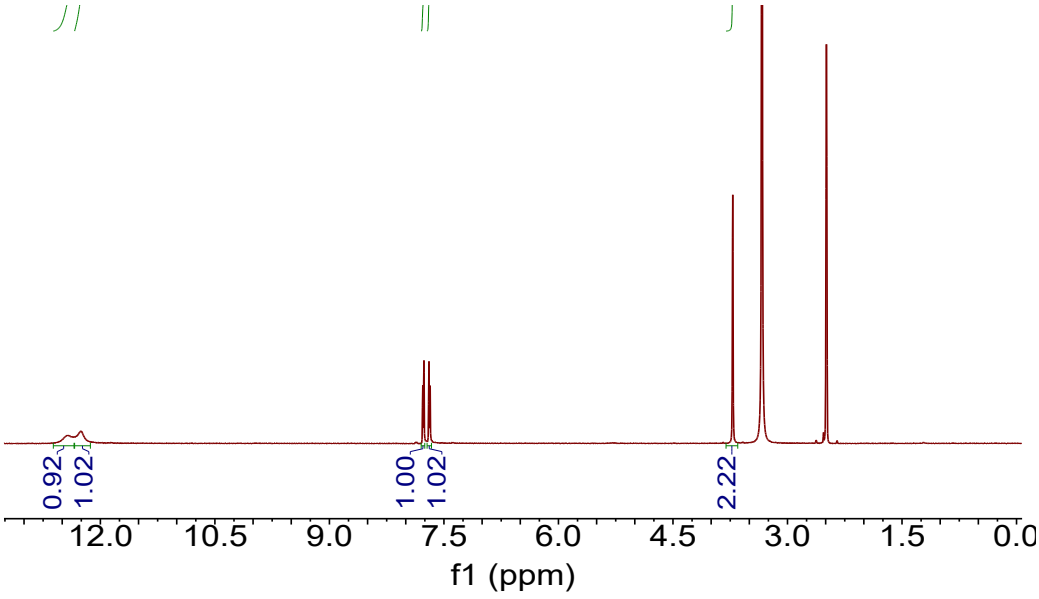

Figure 3.1 ^{1}H NMR spectrum of DCDHAQ in DMSO-d6. Solvent peaks are those that are not integrated. ^{1}H NMR (500 MHz, DMSO-d_6) δ 12.43 (s, 2H), 12.24. (s, 2H), 7.76 (dd, J=7.5 Hz, 2H), 7.68 (dd, J=7.5 Hz, 2H), 3.71 (s, 4H).

3.2.2 Synthesis of 1,4-dihydroxy-2-carboxymethyl-9,10-anthraquinone (1,4-CDHAQ):

3 g of 1,4-dihydroxyanthraquinone (12.49 mmol) was added to 100 mL 0.1 M NaOH solution. The mixture was stirred at room temperature for 0.5 h under nitrogen. A portion of $Na_2S_2O_4$ (2.39 g, 13.74 mmol) was added to the mixture to give an orange-red solution. Then an aqueous solution of glyoxylic acid (50%, 2 eq.) was added to the above mixture. The temperature was increased to 80 °C, for 1 h, cooled to room temperature and exposed to air. The solution was subsequently acidified with 2 M HCl to collect the crude solid. The crude compound was washed with DMSO to give a red solid. Yield: 3 g (81%).

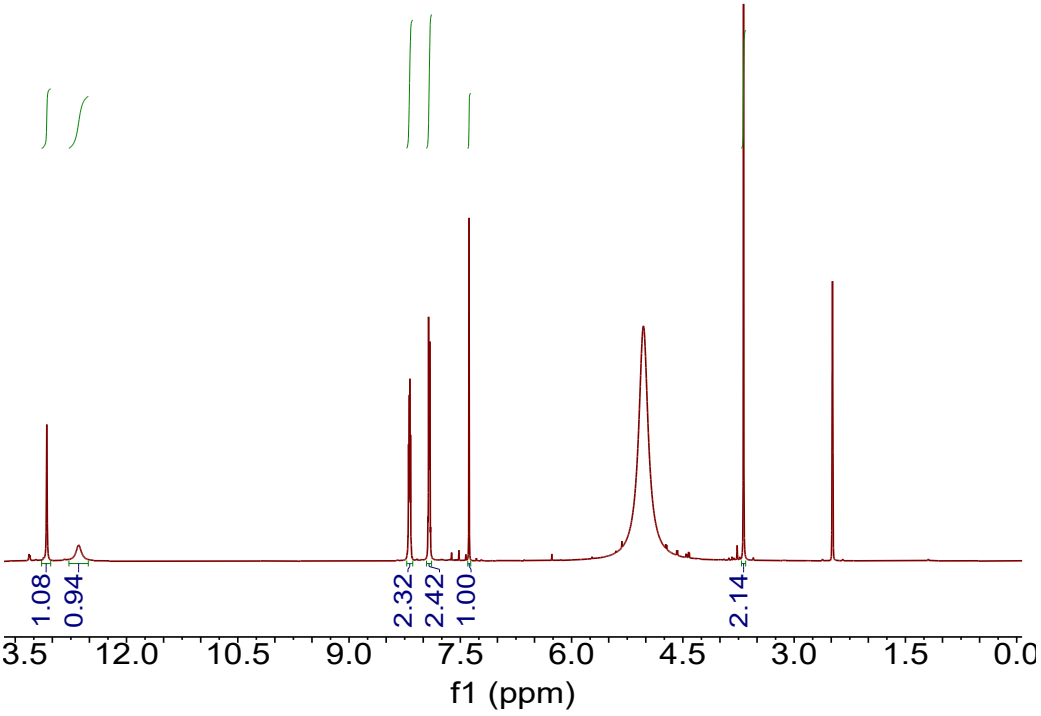

Figure 3.2 ^{1}H NMR spectrum of 1,4-CDHAQ in DMSO-d6. Solvent peaks are those that are not integrated. ^{1}H NMR (500 MHz, DMSO-d_6) δ 13.10 (s, 1H), 12.66 (s, 1H), 8.22. (m, 2H), 7.95 (m, 2H), 7.42 (s, 1H), 3.70 (s, 2H), peak at 5.02 is the water peak.

3.2.3 Full cell measurements

Flow battery experiments were conducted with cell and hardware from Fuel Cell Tech. (Albuquerque, NM), assembled into a zero-gap flow cell configuration. Pyrosealed POCO graphite flow plates with serpentine flow patterns were used for both electrodes. Each electrode comprised a 5 cm^2 geometric surface area covered by one sheet of AvCarb carbon cloth electrode. For DCDHAQ/ferrocyanide full cell tests, a Nafion^{TM} 212 membrane was used to serve as the ion-selective membrane between the AvCarb electrodes. The Nafion membrane was soaked in 1M KOH for 24 hours before use. The outer portion of the space between the electrodes was gasketed by Viton sheets with the area over the electrodes cut out. Torque applied during cell assembly was 60 lb-in (6.78 Nm) on each of eight 1/4-28 bolts. The electrolytes were fed into the cell through fluorinated ethylene propylene (FEP) tubing at a rate of 60 mL/min, controlled by Cole-Parmer 6 Masterflex L/S peristaltic pumps. The 0.2 M DCDHAQ/ferrocyanide cell was run inside a nitrogen-filled glove bag and the 0.75 M DCDHAQ/ferrocyanide cell was run inside a glove box (1 ppm O_2). Cell polarization measurements and charge-discharge cycling were performed using a Biologic BCS-815 battery cycler. Long-term cycling of the 0.2 M DCDHAQ/ferrocyanide cell was performed at ±50 mA cm^{-2} with potential holds at 1.4 V for charging and 0.8 V for discharging until the current density dropped to 2 mA cm^{-2}. For the limited SOC cycling, the cell was charged to a fixed state of charge (e.g., 80% SOC or 90% SOC) and then fully discharged to 0.8 V with the potential held until the current dropped to 2 mA cm^{-2}. For the

0.75 M DCDHAQ/ferrocyanide cell, the cut-off voltage was 1.4 V for charging and 0.6 V for discharging. The polarization curves were obtained by charging to the desired state of charge first and then polarizing via linear sweep voltammetry at a rate of 100 mV s^{-1}. This method yielded polarization curves very close to those obtained by point-by-point galvanostatic holds and imposes minimal perturbation to the SOC of the small-electrolyte-volume cell.

A glassy carbon (BASi, 3 mm diameter) working electrode, an Ag/AgCl reference electrode (BASi, pre-soaked in a 3 M NaCl solution), and a graphite counter electrode were used in the three-electrode system for all CV tests. The scan rates for CV tests were 10, 20, 50, 100, and 200 mV s^{-1}. The diffusion coefficient D was calculated based on the Randles-Sevcik equation: $I_p = 269000 \times n^{1.5}AD^{0.5}v^{0.5}C$, Where I_p is the peak current in amps, n is the number of electrons involved ($n = 2$ for DCDHAQ), A is the active surface area (0.0707 cm^2), D is the diffusion coefficient in cm^2/s, v is the scan rate in V/s, and C is the concentration of redox species in mol/cm^3.

3.3 Results and Discussion

DCDHAQ was synthesized via a one-pot, green synthesis method with an inexpensive precursor 1,8-DHAQ and finished in around 4 hours. As shown in Scheme 3.1, 1,8-DHAQ was reduced by sodium dithionite. Subsequently, the side-chain precursor, glyoxylic acid, was added to the solution, where the coupling reaction happened at room temperature to form 2,7-di-hydroxyacetic acid-1,8,9,10-tetrahydroxy-anthracene (DHATHAc).

DHATHAc was further reduced with sodium dithionite and then air oxidized to form DCDHAQ.

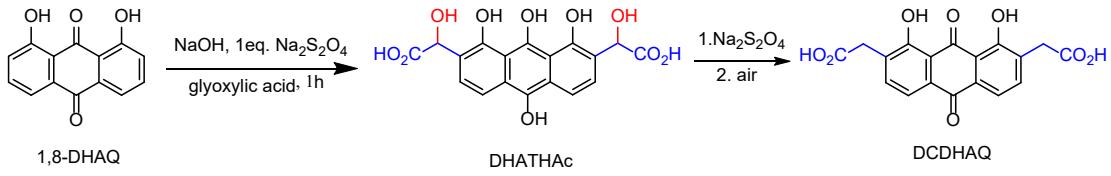

Scheme 3.1 Synthetic route for DCDHAQ.

Figure 3.3a compares the water solubility of 1,8-DHAQ and DCDHAQ. 1,8-DHAQ has a solubility of 0.008 M and 0.08 M at pH 12 and 14, respectively, whereas DCDHAQ has a solubility of 1.1 M and 1.3 M at pH 12 and 14, respectively; these latter values correspond to a volumetric capacity of 59.0 Ah/L and 69.7 Ah/L, respectively. Thus, the volumetric capacity of anthraquinone increased by more than one order of magnitude with a simple chemical functionalization. The cyclic voltammograms (CV) of 1,8-DHAQ, DCDHAQ, and potassium ferrocyanide are shown in Figure 3.3b. The redox potential of DCDHAQ at pH 14 is –0.56 V vs. SHE, which is 20 mV higher than that of 1,8-DHAQ. The increased redox potential is known to suppress the disproportionation reaction of reduced anthraquinone thermodynamically, thereby improving the cell cycling stability.[80] Additionally, compared to 1,8-DHAQ, the DCDHAQ molecule has two additional negative charges, which may increase cell lifetime by reducing the rate of the disproportionation side reaction via Coulomb repulsion [80, 107] and by decreasing the molecular crossover rate. Pairing a DCDHAQ negolyte with potassium ferrocyanide at pH 14 yields an equilibrium cell potential of approximately 1.06 V (Figure 3.3b). The Pourbaix diagram of DCDHAQ

is shown in Figure 3.3c. Because the redox potential of DCDHAQ decreases as pH increases, the cell was run at pH 14 to achieve a high cell voltage. The diffusion coefficient of DCDHAQ can be calculated by the Randles–Sevcik equation because the redox reaction of anthraquinone is a diffusion-controlled process as indicated by the linear relationship between peak currents and square root of scan rate (Figure 3.3d). The diffusion coefficient of DCDHAQ was calculated to be 3.6×10^{-6} cm^2 s^{-1} for the cathodic reduction and 1.2×10^{-6} cm^2 s^{-1} for the anodic oxidation; these are similar to the values reported for other redox organics in aqueous condition.[108] The high diffusion coefficient for the cathodic reduction contributes to a low mass transport overpotential, which is beneficial for the energy efficiency.

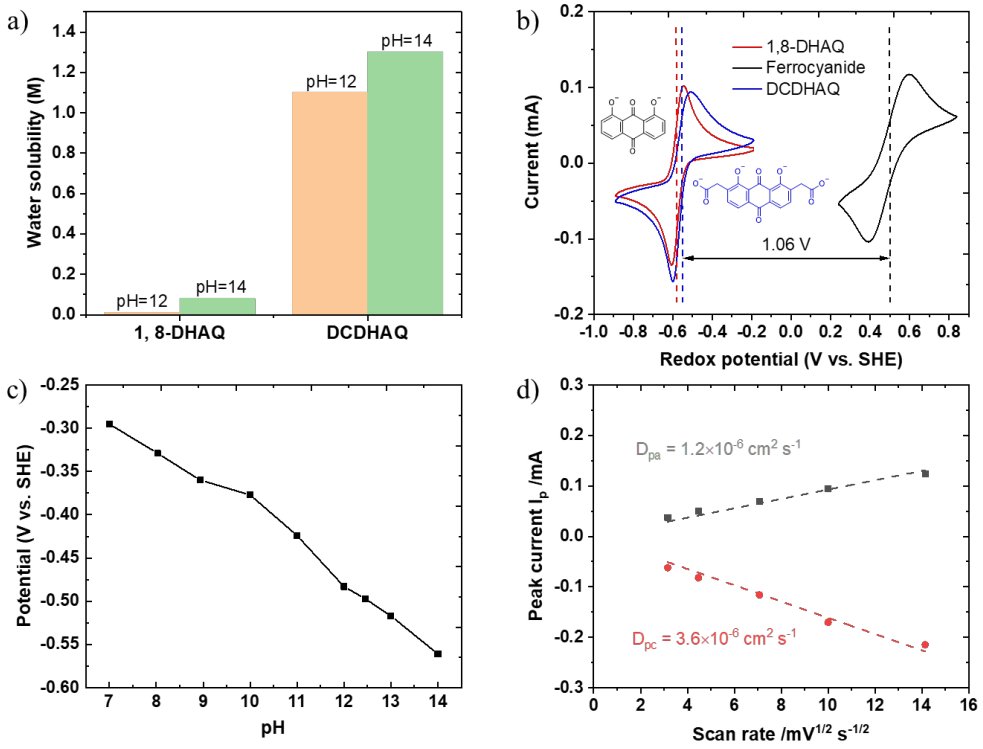

Figure 3.3 Physical and electrochemical properties of 1,8-DHAQ and DCDHAQ. a) Solubility comparison for 1,8-DHAQ and DCDHAQ in KOH(aq); b) Cyclic voltammograms of 5 mM 1,8-DHAQ, 5 mM DCDHAQ and 10 mM potassium ferrocyanide at pH 14 with a scan rate of 100 mV/s; c) Pourbaix diagram of DCDHAQ redox process; d) demonstration of proportional relationship between peak current and square root of scan rate for oxidation (gray) and reduction (red) of DCDHAQ.

To understand the quantitative relationship between cell potential E_{cell}, standard cell potential E^0_{cell}, cell overpotential $ir(i)$, and state of charge (SOC) of the negolyte when the negolyte is the capacity limiting side of the RFB, we performed a numerical simulation of SOC with various $E_{cell} - E^0_{cell} - ir(i)$ values. Here i is the current density and $r(i)$ is the area-specific resistance of the cell as a whole which, in principle, may depend on current density. For electrochemical reactions that occur in a flow battery, the relevant equilibrium potentials can be expressed as

Posolyte: $A - ne^- \rightleftharpoons A^{n+}, E^{eq}_{posolyte} = E^0_{posolyte} - \frac{RT}{nF} ln \frac{C^*_A}{C^*_{A^{n+}}}$; (3.1)

Negolyte: $B + me^- \rightleftharpoons B^{m-}, E^{eq}_{negolyte} = E^0_{negolyte} - \frac{RT}{mF} ln \frac{C^*_{B^{m-}}}{C^*_B}$. (3.2)

with the assumption that the activity coefficients are concentration-independent. *C* represents the concentration of the electroactive species A or B either in its reduced or oxidized form, *R* is the universal gas constant, *T* is the absolute temperature, *F* is Faraday's constant. E^{eq} and E^0 are equilibrium and standard redox potentials of desired electrolytes as denoted by the relevant subscripts. And *n* and *m* are the number of electrons transferred during the electrochemical reaction of A and B, respectively. The cell potential becomes

$$E_{cell} = E^{eq}_{posolyte} - E^{eq}_{negolyte} + ir(i) = E^0_{cell} - \frac{RT}{nF} ln \frac{C^*_A}{C^*_{A^{n+}}} + \frac{RT}{mF} ln \frac{C^*_{B^{m-}}}{C^*_B} + ir(i), \quad (3.3)$$

where E_{cell} is the cell potential, E^0_{cell} is the cell potential at standard state, *ir(i)* is the total cell overpotential, reckoned as positive during the charging step. For an anthraquinone (AQ)/ferrocyanide full cell, *m*=2 and *n*=1 as anthraquinone and ferrocyanide undergo two-electron and one-electron redox processes, respectively. Under a negolyte capacity-limited condition with the assumption that no complexes form in the electrolytes, we have

$$\frac{C^*_{B^{m-}}}{C^*_B} = \frac{SOC}{1 - SOC}, \quad (3.4)$$

$$E_{cell} = E^0_{cell} - \frac{RT}{F} ln \frac{C^*_{Ferro}}{C^*_{Ferri}} + \frac{RT}{2F} ln \frac{SOC}{1 - SOC} + ir(i). \quad (3.5)$$

In a general case of AQ as the capacity limiting side,

$$\frac{C^*_{Ferro}}{C^*_{Ferri}} = \frac{n^0_{Ferro} - 2n_{rAQ}}{n^0_{Ferri} + 2n_{rAQ}} = \frac{n^0_{Ferro} / 2n^0_{AQ} - 2n_{rAQ} / 2n^0_{AQ}}{n^0_{Ferri} / 2n^0_{AQ} + 2n_{rAQ} / 2n^0_{AQ}} = \frac{p - SOC}{q + SOC}, \tag{3.6}$$

where $n^0_{Ferro}, n^0_{Ferri}, n^0_{AQ}$ are the initial molarities of ferrocyanide, ferricyanide, and AQ; and n_{rAQ} is the molarity of reduced AQ. AQ is presumed to be fully oxidized initially. *p* and *q* represent the initial capacity ratios of ferrocyanide to AQ and ferricyanide to AQ, respectively, and are defined as:

$$p = n^0_{Ferro} / 2n^0_{AQ}; \tag{3.7}$$

$$q = n^0_{Ferri} / 2n^0_{AQ}. \tag{3.8}$$

Therefore, the cell potential, E_{cell}, of an AQ capacity-limited flow battery may be expressed as:

$$E_{cell} = E^0_{cell} + \frac{RT}{2F} ln\left(\frac{SOC}{1 - SOC} \times \left(\frac{q + SOC}{p - SOC} \right)^2 \right) + ir(i). \tag{3.9}$$

For a capacity-balanced full cell for which the capacity of posolyte and negolyte are equal, *p*=1 and *q*=0. We plot $E_{cell} - E^0_{cell} - ir(i)$ as a function of achievable SOC at different electrolyte compositions to obtain Figure 3.4.

It is clear that, to achieve an essentially full SOC, the magnitude of $E_{cell} - E^0_{cell}$ should be 0.2 V or above as shown in Figure 3.4a, especially for a capacity balanced cell (*p*=1, *q*=0). Therefore, charging of the cell should be continued until the cell voltage is at least 0.2 V higher than E^0_{cell} for a two-electron redox molecule. The standard cell voltage for a certain redox couple is not necessarily equal to the open-circuit voltage (OCV) at 50% SOC when the cell is not capacity-balanced. The OCV at 50% SOC varies with ferro-

/ferricyanide ratio, whereas E_{cell}^{0} stays constant. Figure 3.4b compares the dependence of $E_{cell} - E_{cell}^{0} - ir(i)$ on SOC for a single-electron process in the posolyte and either a single-electron process or a two-electron process in the negolyte, suggesting that, other things being equal, accessing the same SOC requires charging to a higher cell voltage for a single-electron molecule than for a two-electron molecule.

A common method of investigating charge capacity and its fade rate is to charge the cell to a certain voltage (either potentiostatically or galvanostatically with a cutoff voltage, and then to hold at that voltage until the current density decays to a fixed cutoff value before switching polarity – and likewise for discharging. To investigate the relationship between maximum accessible SOC and cut-off current density, we present Figure 3.4c, in which we assume $r(i)$ is a constant over the entire SOC range. At intermediate SOC the activation overpotential has been shown to be Ohmic for species with fast kinetics and the mass transport overpotential has been shown to be Ohmic for reactant utilization (the fraction of reactant converted by the device in a single pass, which is proportional to the current divided by the product of reactant concentration and flow rate) up to about 40%.[109, 110] It is apparent from Figure 3.4c that, for current densities of tens of mA cm^{-2}, a small change in cell resistance, e.g through aging or temperature drifts, leads to a significant change in maximum accessible SOC, leading to large fluctuations in apparent cell capacity and the inability to evaluate low capacity fade rates. For a cell with a non-Ohmic mass transport overpotential, which may occur when the charging approaches the high-SOC limit where

the concentration of available reactant becomes quite small and the utilization may become quite high, the mass transportant overpotential increases superlinearly with current density.[110] The net effect of this nonlinear behavior is a move to the right along the curve for the current density under consideration. In other words, the assumption of Ohmic behavior in Figure 3.4c means that the curves represent an upper limit to the maximum accessible SOC. We conclude that, in order to measure stable high SOC values not subject to artifacts from drifting cell resistance, a potential hold until the current density drops to a small cut-off value is needed, as shown experimentally by Goulet and Aziz.[13] The simulation presented here serves as a guide for selecting numerical values of cycling voltage limits and cut-off current density for an accurate evaluation of discharge capacity and of slow capacity fade rates in redox flow batteries.

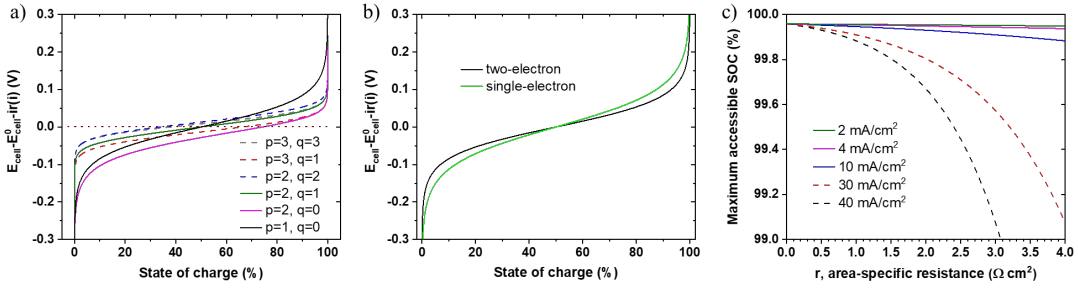

Figure 3.4 Simulations for a cell with a capacity-limiting negolyte and a posolyte comprising one-electron redox molecules. a) Calculated $E_{cell} - E^0_{cell} - ir(i)$ vs. SOC for negolyte comprising two-electron redox molecules of different electrolyte compositions; b) Calculated $E_{cell} - E^0_{cell} - ir(i)$ as a function of SOC for a capacity balanced cell (p=1, q=0) with negolyte undergoing a two-electron reaction or a single-electron reaction; c) maximum accessible SOC vs. cell resistance for various cut-off current densities when $E_{cell} - E^0_{cell} = 0.3$ V for a capacity-balanced cell (p=1, q=0) with negolyte comprising two-electron redox molecules.

Polarization experiments of a 0.75 M DCDHAQ/ferrocyanide full cell at pH 14 were performed at various states of charge. The electrolytes comprised 5 mL of 0.75 M DCDHAQ (negolyte) at pH 14 and 40 mL of 0.3 M potassium ferrocyanide and 0.3 M potassium ferricyanide (posolyte) at pH 14 to ensure that the negolyte always remained the capacity limiting side. The concentrations were chosen such that the cation concentrations were balanced at intermediate SOC to reduce the osmotic imbalance. The cell was constructed from graphite flow plates and AvCarb carbon cloth electrodes, separated by a Nafion 212 membrane pretreated in 1M KOH. The open-circuit voltage (OCV) increases from 1.1 to 1.23 V as the state of charge (SOC) increases from 10% to ~90% (Figure 3.5a). The OCV at 50% SOC is around 1.16 V. A peak galvanic power density of 0.16 W cm^{-2} was achieved at ~90% SOC (Figure 3.5b). The power density may be increased by engineering improvements such as the incorporation of lower- resistance membranes.

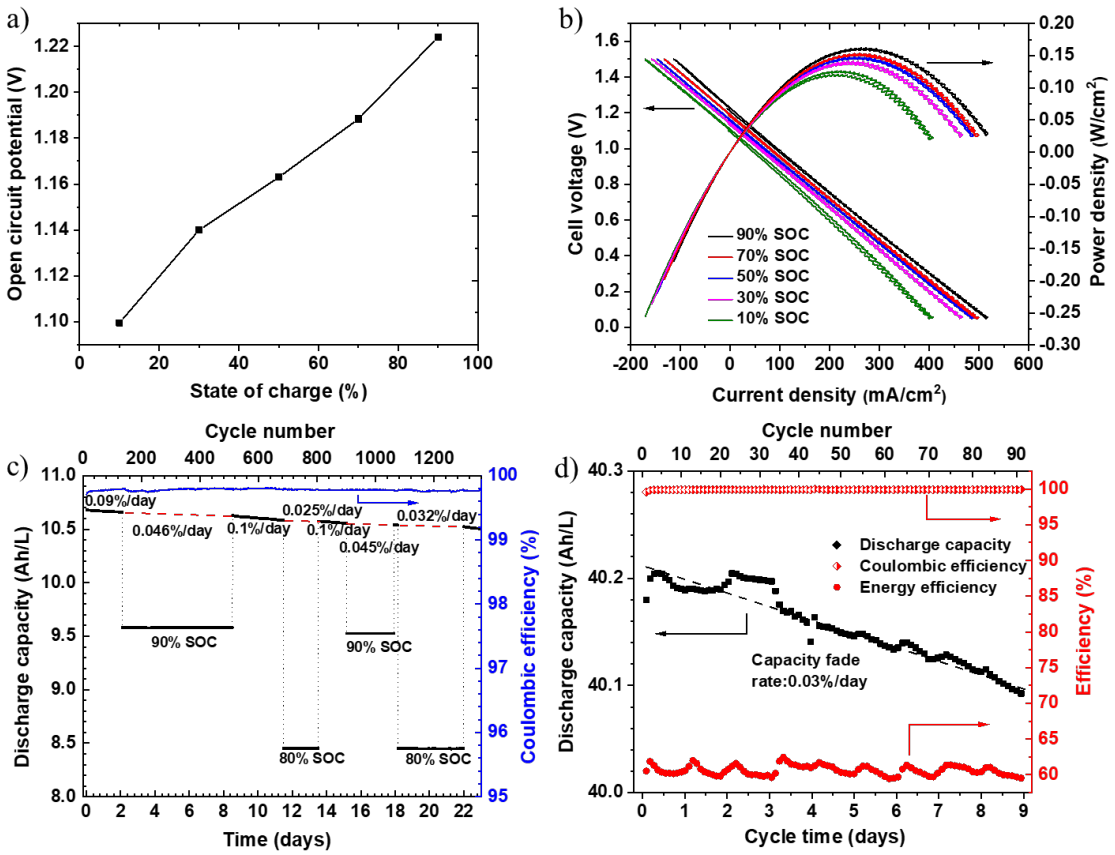

Figure 3.5 Electrochemistry of DCDHAQ. a) Open circuit voltage of 0.75 M DCDHAQ/0.3 M potassium ferrocyanide + 0.3 M potassium ferricyanide full cell at pH 14; b) Polarization measurements of the corresponding 0.75 M full cell at pH 14; c) Cell cycling of 5 mL 0.2 M DCDHAQ and 30 mL 0.2 M ferrocyanide + 0.02 M ferricyanide at pH 14; d) Discharge capacity, Coulombic efficiency, and round-trip energy efficiency during cycling of 0.75 M DCDHAQ with 0.3 M potassium ferrocyanide and 0.3 M potassium ferricyanide full cell at pH 14.

Long-term galvanostatic cycling of the 0.2 M DCDHAQ/ferrocyanide cell was performed at 50 mA cm^{-2} with potential holds at 1.4 V for charging and 0.8 V for discharging until the current density dropped to 2 mA cm^{-2} (Figure 3.5c). The electrolytes comprised 5 mL of 0.2 M DCDHAQ (negolyte) at pH 14 and 40 mL of 0.2 M potassium ferrocyanide + 0.02 M potassium ferricyanide (posolyte) at pH 14. The initial discharge capacity at full SOC was 10.67 Ah L^{-1} (theoretical value 10.72 Ah L^{-1}). After 2.1 days of

full SOC range cycling, the capacity faded by 0.19%, corresponding to a temporal capacity fade rate of 0.09%/day or 0.0017%/cycle. For the next 6.4 days, the cell continued to be charged galvanostatically to 90% SOC at 50 mA cm^{-2} and immediately discharged to 0.8 V at 50 mA cm^{-2} with a potential hold, until the current density dropped to 2 mA cm^{-2}. The cell was subsequently charged back to full SOC to evaluate the capacity fade rate during cycling when charging had been limited to 90% SOC. The capacity fade rate when charging was limited to 90% SOC was determined to be 0.046%/day or 0.00074%/cycle. Similarly, the average capacity fade rate when charging was limited to 80% SOC was around 0.03%/day. The increased cycling stability at lower charge-limiting SOC suggests that the capacity fade was due to the formation of electrochemically inactive anthrone, which is known to be suppressed by limiting charging during cycling.[80] Cycling was continued at different limiting SOCs (100%, 90%, 100%, 80%, 100%, 90%, 100%, 80%, 100%) for 23 days, and the discharge capacity was always determined immediately after fully charging the cell. The average capacity fade rate for the 23 days of cycling was 0.068%/day or 0.0011%/cycle with an average coulombic efficiency of 99.8%, which stands out as the most stable cell performance to date with a potentially low-cost redox-active organic molecule, as shown in Table 3.1.

Table 3.1 Properties of potentially low-cost redox-active organics for aqueous redox flow batteries.

Negolyte	Posolyte	Electron Concentration (M) Nego-/Posolyte	$E_{cell} - E^0_{cell}$ (V)	Cut-off current density (mA/cm^2)	Cell voltage (V)	Capacity fade rate (%/day)	Ref
Methyl viologen	4-OH-TEMPO	0.5/0.5	0.45	60	1.25	3.5	92
Methyl viologen	FcNCl	0.7/0.7	0.45	60	1.06	1.3	39
Alloxa-zine	Ferro-cyanide	2/0.4	0.6	100	1.13	1.8	61
DHPS	Ferro-cyanide	2.8/0.31	0.3	100	1.4	0.68	63
Phena-zine BHPC	Ferro-cyanide	1/0.4	0.4	100	1.3	0.08	100
2,6-DHAQ	Ferro-cyanide	1/0.4	0.5	100	1.2	5	60
1,8-DHAQ	Ferro-cyanide	0.2/0.2	0.45	80	1.1	13	89
PEGAQ	Ferro-cyanide	3/0.31 0.2/0.1	0.25	16	1.05	0.5 1.1	68
DCDH-AQ	Ferro-cyanide	1.5/0.3 0.4/0.2	0.35	2	1.1	0.03 0.1	**This work**

Long-term cycling of the 0.75 M DCDHAQ/ferrocyanide cell was performed at 40 mA cm^{-2} with potential holds at 1.5 V for charging and 0.6 V for discharging until the current density dropped to 2 mA cm^{-2} (Figure 3.5d). Such a wide voltage window and low cut-off current density should access the full cell capacity, according to the simulation results presented in Figure 3.4a. When the cut-off voltage with respect to the measured OCV and the cut-off current density are appropriate as the simulations suggest, measurements of

capacity and true capacity fade rate reflect losses from chemical decomposition, leakage, or crossover of active species from the capacity limiting side.[111] The initial volumetric capacity was 40.2 Ah L^{-1}, which is equal to the theoretical capacity, to three significant figures. The measured volumetric capacity is one of the highest capacities demonstrated experimentally for AORFBs.[68, 79] The coulombic efficiency is above 99.9% over the whole cycling process. Although the round-trip energy efficiency exhibited in Figure 3.5d fluctuated due to daily temperature oscillations in the laboratory, the daily capacity fluctuation was much smaller; this highlights the importance of the potential-hold method to accurately evaluate the capacity fade rate. After 9 days of cycling, the volumetric capacity faded by 0.27%, which corresponded to a temporal capacity fade of 0.03%/day, or 0.0029%/cycle, representing one of the most stable organics reported.[67] Surprisingly, the capacity fade rate (0.03%/day) at the elevated concentration is lower than that at low concentration (0.09 ~ 0.1%/day). This observation might be due to the increased pH in the charged state of the high-concentration cell or decreased water activity, suppressing the formation of anthrone, which involves two water molecules per molecule of anthrone.[85] No apparent chemical decomposition was detected from the ^{1}H NMR of cycled DCDHAQ as shown in Figure 3.6, indicating high chemical stability of DCDHAQ molecule.

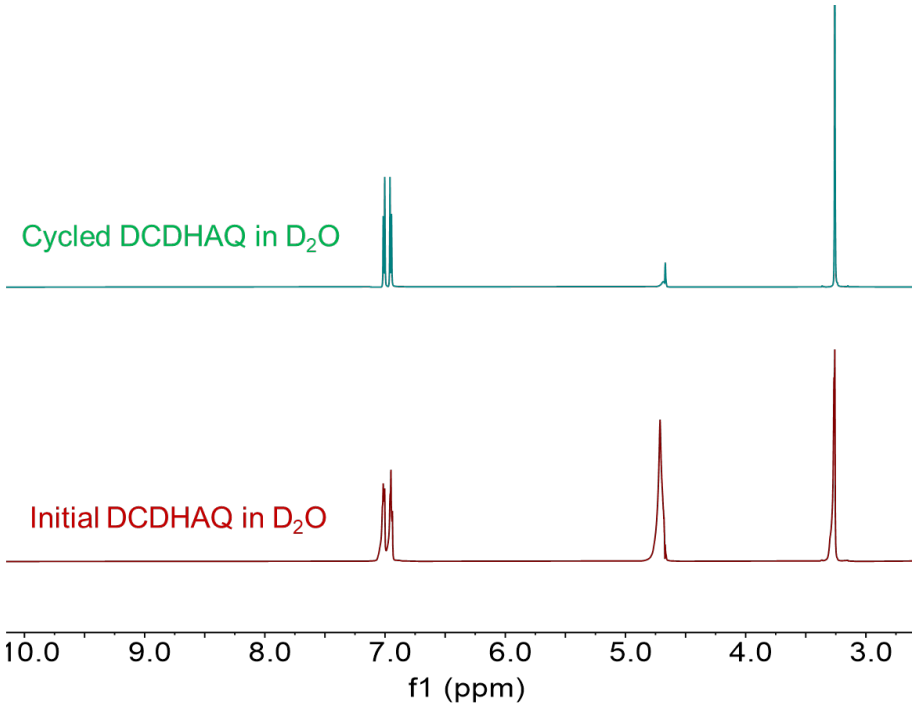

Figure 3.6 ^{1}H NMR spectra of DCDHAQ before and after cycle in D_2O solvent. Suppression of the peak from water at 4.7 ppm was performed to increase other signals. No new decomposition peaks were observed.

When considering the potential for practical deployment, the electrolyte cost at a commercial scale is one of the most important factors but is also one of the most difficult to assess for a new composition of matter. The laboratory-scale cost of the precursor 1,8-DHAQ is low compared to that of its isomer 2,6-DHAQ, as shown in Table 3.2. Given that DCDHAQ synthesis is a one-pot green method that uses water as the solvent and inexpensive glyoxylic acid as the chain precursor, its synthetic cost at a commercial scale could be low. Additionally, the reaction is expected to proceed with an electrochemical synthesis method as shown in Figure 3.7. The electrochemical method would further reduce the synthetic cost because it avoids the use of sodium dithionite and also converts a low value chemical ferrocyanide to a higher value chemical ferricyanide, which is produced

industrially by oxidizing ferrocyanide with chlorine gas. The estimated lab-scale cost of DCDHAQ is slightly higher than that of 1,8-DHAQ but is significantly lower than that of 2,6-DHAQ. The mass-production cost of 2,6-DHAQ was estimated to be between \$0.92/kg and \$3.92/kg.[62, 65] Thus, it is reasonable to suppose the mass-production cost of DCDHAQ could be as low as \$5/kg. The industrial-scale cost of potassium ferrocyanide is around \$2.15/kg,[47] corresponding to a capital cost of about \$61/kWh for the electrolyte.

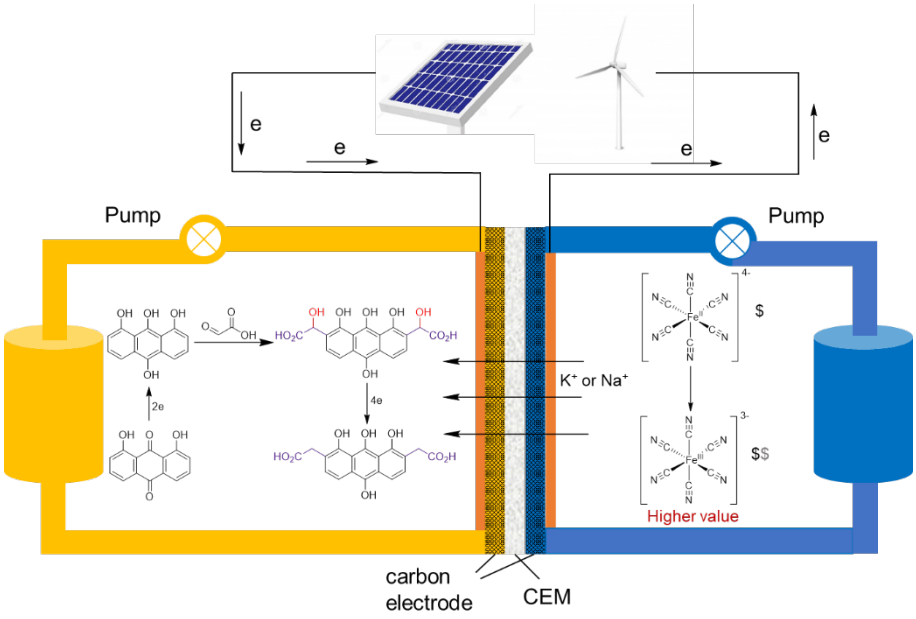

Figure 3.7 Proposed electrochemical synthesis method for DCDHAQ.

3.3.1 Estimation of cost of electrolytes

The cost of 1 kg of 50 wt. % glyoxylic acid solution at Sigma-Aldrich is \$104, corresponding to \$15.4/mol. Therefore, the lab-scale cost of DCDHAQ is estimated to be (34*2+3*15.4)/2/70% = \$82/mol electrons without considering the cost of KOH and sodium dithionite as they are quite inexpensive and also could be potentially eliminated by

the electrochemical synthesis proposed in the main text. In the arithmetic, 2 means two electrons per anthraquinone molecule, 3 means three equivalent of side chain precursor used for synthesis, and 70% is the synthetic yield. The estimated lab-scale cost of DCDHAQ is slightly higher than that of 1,8-DHAQ but significantly lower than that of 2,6-DHAQ. The mass-production cost of 2,6-DHAQ was estimated to be between $0.92/kg and $3.92/kg.[65] Thus, we suppose the scalable cost of DCDHAQ could be as low as $5/kg, resulting in a capacity cost of $0.89/mol electrons for the 2-electron DCDHAQ in the negolyte. The industrial-scale cost of potassium ferrocyanide is around $2.15/kg,[47] corresponding to a capital cost of about $0.91/mol electrons. Given a DCDHAQ/ferrocyanide cell voltage of 1.1 V, the capital cost for the electrolyte is estimated to be $61/kWh.

3.3.2 1,4-CDHAQ results

To demonstrate the generality of the synthetic method of attaching glyoxylic acid groups, we attached a single –CH_2COOH group to 1,4-DHAQ, forming 1,4-dihydroxy-2-carboxymethyl-9,10-anthraquinone (1,4-CDHAQ), as shown in Figure 3.8. Compared to DCDHAQ, the mass-production cost of 1,4-CDHAQ may be lower because of the lower cost of 1,4-DHAQ (Table 3.2) and the use of only half as much of the chain precursor as for DCDHAQ. 1,4-DHAQ is readily produced from phthalic anhydride and 4-chlorophenol; thus, it is the least expensive of the DHAQ family with a cost comparable to that of anthraquinone.[112] The redox potential of 1,4-CDHAQ is -0.56 V vs. SHE at pH 14, enabling

it to form a 1.05 V full cell when paired with potassium ferrocyanide (3.8b). The solubility at pH 14 of 1,4-CDHAQ is 1.0 M, corresponding to a volumetric capacity of 53.6 Ah/L, which is more than 10 times that of 1,4-DHAQ (Figure 3.8c) and comparable to that of DCDHAQ. Unfortunately, 1,4-CDHAQ appears, based on color changes and CV results, to react irreversibly with ferricyanide, which would cross the membrane from the posolyte; thus cell-scale performance evaluation must await a membrane with a negligible ferricyanide crossover rate.

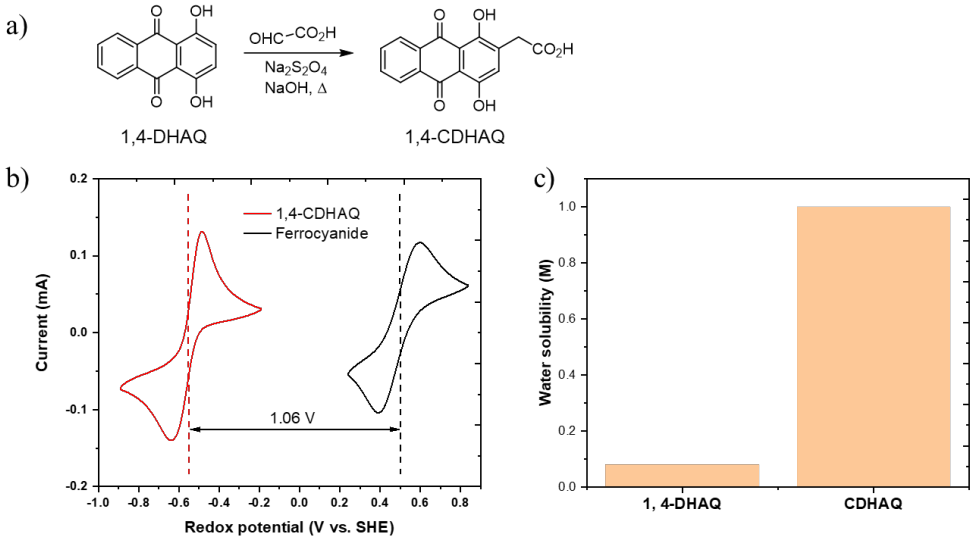

Figure 3.8 Physical and electrochemical properties of 1,4-CDHAQ. a) Synthetic route for 1,4-CDHAQ; b) Cyclic voltammograms of 5 mM 1,4-CDHAQ and 10 mM potassium ferrocyanide at pH 14 with a scan rate of 100 mV/s; c) Water solubility comparison for 1,4-DHAQ and 1,4-CDHAQ in 1 M KOH (aq).

Table 3.2 Electrochemical, physical properties, and estimated lab-scale cost comparison between 1,8-DHAQ, 2,6-DHAQ, DCDHAQ, 1,4-DHAQ. The cost of 1,8-DHAQ, 2,6-DHAQ and 1,4-DHAQ are from Sigma-Aldrich in December 2020.

Compound	Solubility (mol L^{-1}) pH=12, pH=14	$E_{1/2}$ (V vs. SHE)	Capacity fade rate (%/day)	Lab-scale cost ($/$mol_{e^-}$)
1,8-DHAQ	0.008, 0.08	–0.58	13	34
2,6-DHAQ	0.1, 0.6	–0.67	5	3240
DCDHAQ	1.1, 1.3	–0.56	<0.1	82
1,4-DHAQ	N/A, 0.08	–0.56	N/A	23

3.4 Conclusions

We showed how simple molecular modification of a potentially inexpensive but poorly-performing aromatic precursor can improve the performance of redox-active organics in aqueous flow batteries. We demonstrated a high-performance AORFB with a highly soluble, stable, and potentially inexpensive anthraquinone in the negolyte. Because glyoxylic acid is known to react with phenol,[113] the potentially inexpensive synthetic method of attaching glyoxylate groups on aromatics might be readily extended to other anthraquinone derivatives and perhaps other aromatics, accelerating the development of redox-active organics for practical application. Finally, the simulated results relating SOC to cycling voltage limits and cut-off current density provide quantitative guidance for accurate evaluation of cell capacity and its fade rate.

Chapter 4 A Highly Stable Low Redox Potential Quinone for Aqueous Flow Batteries

4.1 Introduction

Safe and economical energy storage technologies are indispensable for the deep penetration of intermittent renewable energies such as photovoltaic and wind electricity.[6, 12, 67] Aqueous redox flow batteries are promising candidates for large-scale energy storage compared to other storage devices such as pumped-hydro, flywheel and lithium-ion batteries, owing to the highly modular configuration, long cycle life and good safety features.[58, 67] Aqueous vanadium redox flow batteries (VRFBs) have been successfully established by many manufacturers, due to their long cycling life and high-power density.[114] Nevertheless, the availability and high fluctuating price of vanadium minerals hinders the widespread application of VRFBs.[67] Consequently, aqueous organic redox flow batteries (AORFBs) are attracting tremendous research interest, as the redox active materials comprising earth abundant elements are potentially less expensive than vanadium.[22, 67, 86, 115] Additionally, the physical and electrochemical properties of redox organics such as water solubility, molecular size, molecular net charge, chemical stability, and redox potential could be tailored via chemical functionalization.[58, 60]

One drawback of many reported AORFBs, however, is their fast capacity fade because redox organics are susceptible to degradation reactions such as nucleophilic substitution,

disproportionation, and tautomerization.[67] To date, various redox-active organics based on quinone,[58, 60, 62, 65, 66, 68, 79, 85, 88-91, 116] viologen,[39, 40, 92, 94-96, 98, 106, 107, 117] phenazine,[63, 99-101] alloxazine,[61] ferrocene[39, 40, 118, 119] and nitroxide radical derivatives[92, 99, 103, 106] have been reported for AORFBs. Most of them, however, exhibit high capacity fade rates of 0.1%–10%/day,[67] which is unsuitable for practical application. Recently, anthraquinone derivatives have demonstrated very good long-term stability.[65, 66, 85] However, their widespread application is hindered by the high synthetic cost due to sophisticated synthesis or expensive precursors. Additionally, their redox potentials are no less than -0.52 V vs. Standard hydrogen electrode (SHE) at pH 14; anthraquinones with a lower redox potential exhibited less stable cycling performance.[60, 120] To achieve a high power density, however, a low redox potential negolyte is desired. Therefore, developing inexpensive and stable negolytes with a low redox potential remains crucial for the practical implementation of AORFBs.

Here, we report a potentially inexpensive and low redox-potential anthraquinone with outstanding cycling stability. The anthraquinone sodium 3,3',3",3'"-((9,10-anthraquinone-2,6-diyl)bis(azanetriyl))tetrakis(propane-1-sulfonate) (2,6-N-TSAQ) was synthesized from potentially inexpensive 2,6-diaminoanthraquinone (2,6-DAAQ) via a one-step *N*-alkylation route. The reduction potential of 2,6-N-TSAQ at pH 12 and above is -0.62 V vs. SHE, which is 120 mV lower than the oxygen-linked anthraquinone sodium 3,3'-((9,10-anthraquinone-2,6-diyl)bis(oxy))bis(propane-1-sulfonate) (2,6-O-DPSAQ) and 170 mV

lower than the carbon-linked anthraquinone sodium 3,3'-(9,10-anthraquinone-2,6-diyl)bis(propane-1-sulfonate) 2,6-DPSAQ. Pairing with ferri/ferrocyanide, it forms a 1.14 V full cell and shows a maximum peak power density of 0.18 W/cm^2 at pH 14. The capacity fade rate of 2,6-N-TSAQ is 0.025%/day at pH 14, making it one of the most stable redox organic molecules ever reported, and the first highly stable anthraquinone with a redox potential below -0.6 V vs. SHE. In contrast, the capacity fade rate at neutral condition (1 M sodium chloride) is as high as 2.6%/day. The substantial difference in anthraquinone cycling stability at different pH values is due to their differences in Gibbs free energy change for the anthrone formation reaction. These results provide guidance to improve the cell performance of anthraquinone-based negolyte, and highlight the great potential of organic synthesis towards inexpensive and stable electrolytes for grid-scale energy storage application.

4.2. Experimental section

Chemicals: 2,6-diaminoanthraquione (97%), 1,3-propanesultone (98%), sodium hydride (60% in mineral oil), anhydrous dimethyl sulfoxide, anhydrous N,N-Dimethylformamide, potassium carbonate, and palladium(II) acetate (98%) were purchased from Sigma-Aldrich. 2,6-dihydroxyanthraquinone (98%) was purchased from AK scientific. Sodium allylsulfonate (94%) was purchased from Ambeed, inc. Ltd. Hydrogen gas was purchased from Airgas. The materials were directly used without further purification.

4.2.1 Synthesis of 2,6-N-TSAQ

3 g of 2,6-diaminoanthraquinone (12.59 mmol) was added to 50 mL anhydrous dimethyl sulfoxide. Then 2.1 g sodium hydride (60%, 52.46 mmol) was added to the solution under vigorous stirring. After 15 minutes, 6.41 g 1,3-propanesultone (98%, 52.46 mmol) was added to the above mixture. The solution was stirred at room temperature for 1 hour. Afterward, ethyl acetate was added to the solution to collect the red solid. The crude product was washed with ethyl acetate to remove any mineral oil. Yield:9.7 g (95%).

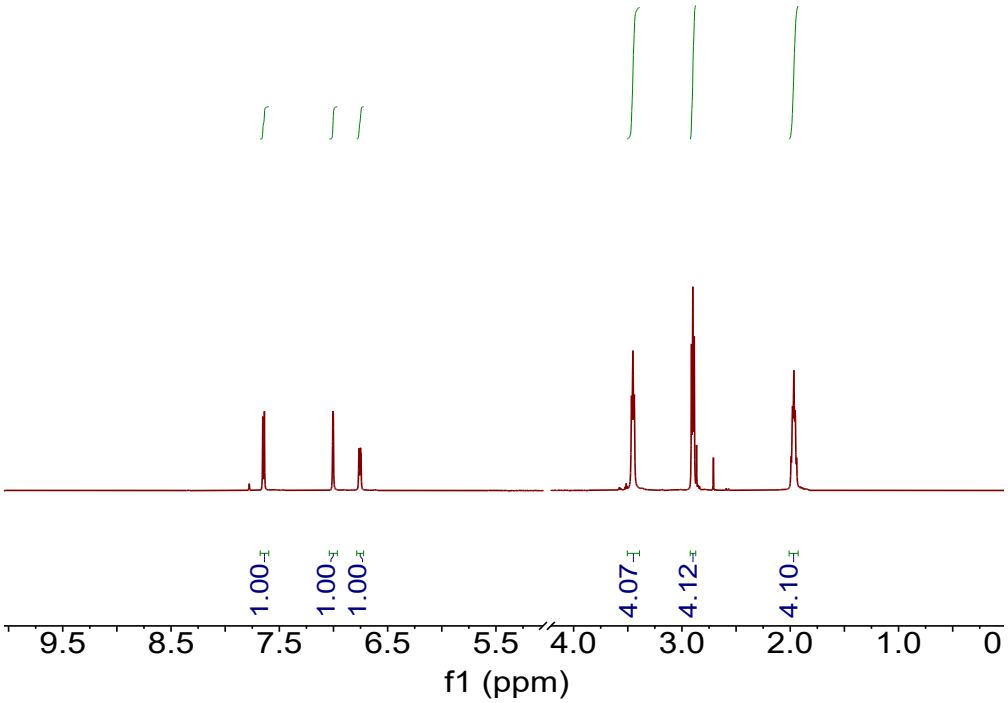

Figure 4.1 ^{1}H NMR spectrum of 2,6-N-TSAQ in D_2O-d6. Solvent peak at 4.7 pm was cut to increase other peaks. ^{1}H NMR (500 MHz, D_2O) δ 7.65 (d, 2H), 7.00 (d, 2H), 6.76 (dd, 2H), 3.45 (t, 8H), 2.90 (t, 8H), 1.97 (m, 8H).

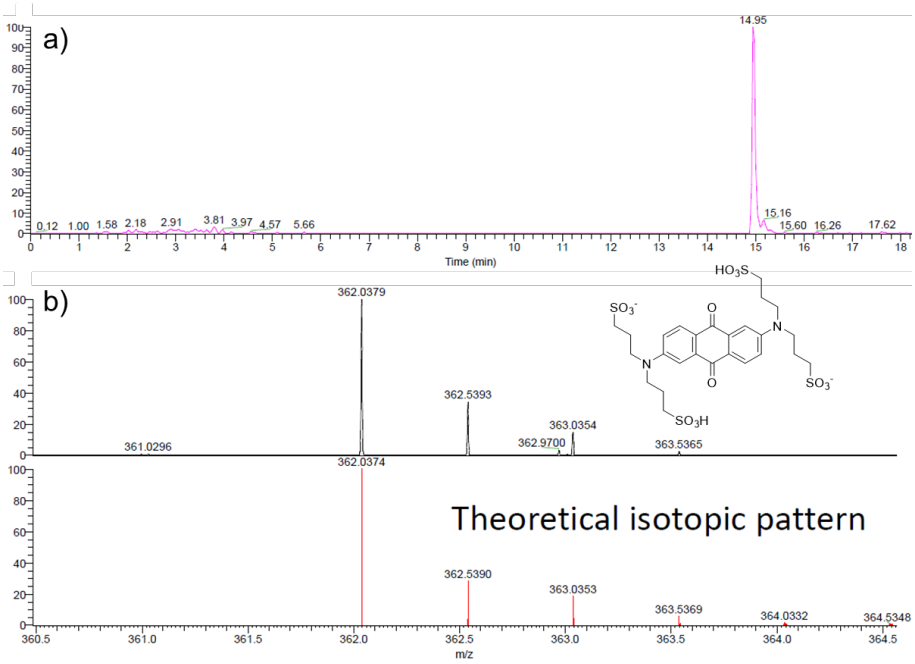

Figure 4.2 LC-MS traces of the synthesized 2,6-N-TSAQ. a) LC trace of 2,6-N-TSAQ; b) Mass spectrum of the material eluted at 14.95 min in the LC trace. The peak at m/z = 362.04 corresponding to the 2,6-N-TSAQ with two protonate form and two negative charges. Sample preparation: 0.1 M 2,6-N-TSAQ was diluted 100 times with HPLC water, and further diluted 100 times with acetonitrile/water co-solvents (volume ratio = 1:1) to the desired concentration 10 μM. High-resolution LC-MS analysis was performed in the Small Molecule Mass Spectrometry Facility at Harvard University on a MiniLIMS. The elution solution is 0.1% v/v formic acid in acetonitrile. The ESI mass spectrum was recorded in negative ionization mode.

4.2.2 Synthesis of 2,6-O-DPSAQ

3 g of 2,6-dihydroxyanthraquinone (12.49 mmol) was added to 50 mL anhydrous N,N-Dimethylformamide. Then 1.05 g sodium hydride (60%, 26.23 mmol) was added to the solution under vigorous stirring. After 15 minutes, 3.20 g 1,3-propanesultone (98%, 26.23 mmol) was added to the above mixture. The solution was stirred at room temperature for 1 hour. Afterwards, ethyl acetate was added to the solution to collect the yellow solid. The crude product was washed with ethyl acetate to remove any mineral oil. Yield: 6.4 g (97%).

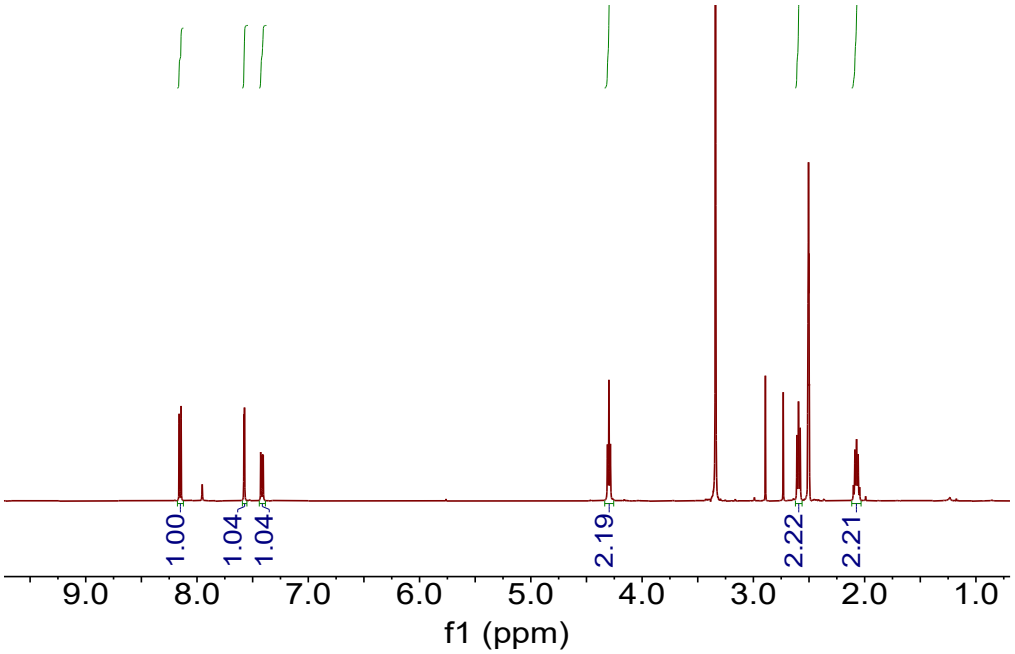

Figure 4.3 ^{1}H NMR spectrum of 2,6-O-DPSAQ in DMSO-d6. Solvent peaks are those not integrated. ^{1}H NMR (500 MHz, DMSO-d6) δ 8.15 (d, 2H), 7.58 (d, 2H), 7.42 (dd, 2H), 4.30 (t, 4H), 2.59 (t, 4H), 2.07 (m, 4H).

4.2.3 Synthesis of 2,6-DPSAQ

2,6-diiodoanthraquinone was synthesized according to the reported procedure.[121] Heat a mixture of 2 g 2,6-diiodoanthraquinone (4.35 mmol), 0.75 g sodium allylsulfonate (5.22 mmol), 0.72 g potassium carbonate (5.22 mmol) and 49 mg palladium acetate(0.22 mmol) in 40 mL water in a pressure vessel at 120 °C for overnight. The mixture solution was filtered to remove any insoluble gradients. Collect the filtrate and add it to a 20 mL methanol solution. The solution was stirred in a hydrogen atmosphere for overnight. Evaporate the solution in vacuum to collect the solid. Yield: 1.51 g (70%).

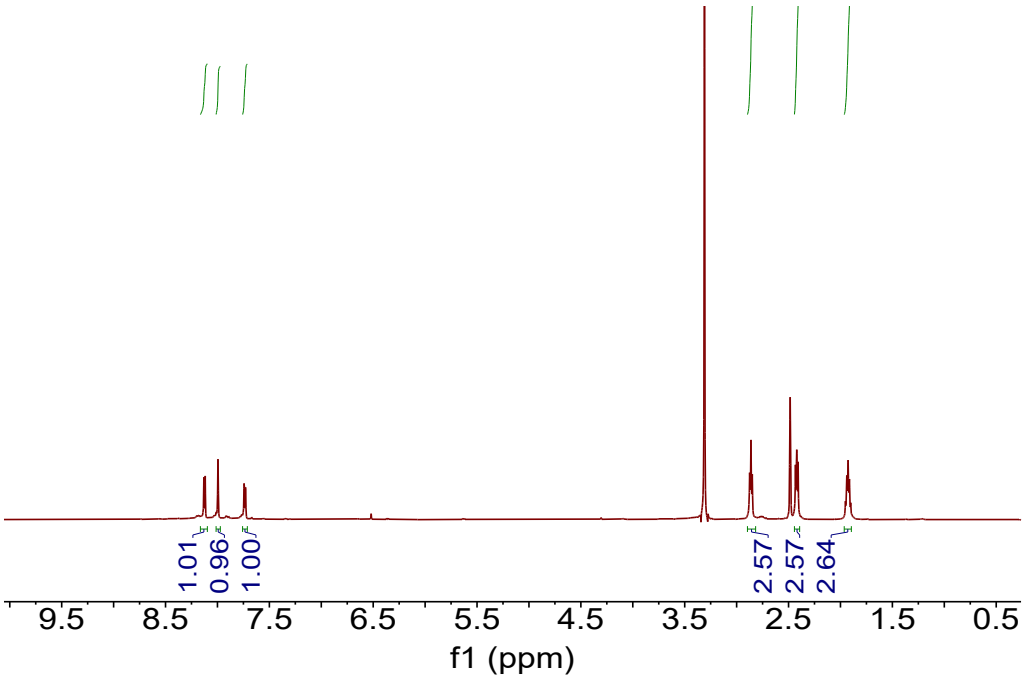

Figure 4.4 ^{1}H NMR spectrum of 2,6-DPSAQ in DMSO-d6. Solvent peaks are those not integrated. ^{1}H NMR (500 MHz, DMSO-d6) δ 8.12 (d, 2H), 7.99 (d, 2H), 7.74 (dd, 2H), 2.86 (t, 4H), 2.42 (t, 4H), 1.93 (m, 4H).

4.2.4 Full cell measurements

Flow battery experiments were performed with cell and hardware from Fuel Cell Tech. (Albuquerque, NM). Pyrosealed POCO graphite flow plates with serpentine flow designs were used for both electrodes. Each electrode comprised a single 5 cm^2 geometric surface area sheet of AvCarb carbon electrode. For 2,6-N-TSAQ/ferrocyanide full cell tests, a Nafion^{TM} 212 membrane was used to serve as the ion-selective membrane. The Nafion membrane was soaked in the supporting electrolyte (sodium hydroxide or sodium chloride) for at least 24 hours before use. Viton sheets were used to cover the outer portion space between the electrodes. Torque used for cell assembly was 60 lb-in (6.78 Nm) on each of

eight 1/4-28 bolts. The electrolytes were fed into the cell through fluorinated ethylene propylene (FEP) tubing at a rate of 60 mL/min, controlled by Cole-Parmer 6 Masterflex L/S peristaltic pumps. The cell was run inside a glove box (1 ppm O_2). Cell polarization measurements and charge-discharge cycling were conducted using a Biologic BCS-815 battery cycler. Long-term cycling of the 0.1 M 2,6-N-TSAQ/ferrocyanide cell was achieved at ±40 mA cm^{-2} with potential holds at 1.4 V for charging and 0.6 V for discharging until the current density dropped to 2 mA cm^{-2}. The polarization curves were obtained by charging to a desired state of charge first and then polarizing via linear sweep voltammetry at a rate of 100 mV s^{-1}.

A glassy carbon (BASi, 3 mm diameter) working electrode, an Ag/AgCl reference electrode (BASi, 3 M NaCl solution), and a graphite counter electrode were used in the three-electrode system for all CV tests. The scan rates for CV tests were 10, 20, 50, 100, and 200 mV s^{-1}. The diffusion coefficient D was calculated based on the Randles-Sevcik equation: $I_p = 269000 \times n^{1.5} A D^{0.5} v^{0.5} C$,[122] where I_p is the peak current in amps, n is the number of electrons involved ($n = 2$ for 2,6-N-TSAQ) in the redox reaction, A is the active surface area (0.0707 cm^2), D is the diffusion coefficient in cm^2/s, ν is the scan rate in V/s, and C is the concentration of redox species in mol/cm^3.

4.3 Results and Discussion

Figure 4.5 illustrates the synthetic routes for three different anthraquinones 2,6-N-TSAQ, 2,6-O-DPSAQ and 2,6-DPSAQ. The structure of 2,6-N-TSAQ was verified by ^{1}H nuclear magnetic resonance (NMR) and high-resolution liquid chromatography-mass spectrometry as shown in Figure 4.1 and 4.2. And the structures of 2,6-O-DPSAQ and 2,6-DPSAQ were verified by ^{1}H NMR as shown in Figure 4.3 and 4.4. Among them, 2,6-N-TSAQ and 2,6-O-DPSAQ were synthesized via a similar one-step nucleophilic reaction. 2,6-N-TSAQ was produced from 2,6-DAAQ, and 2,6-O-DPSAQ was synthesized from 2,6-dihydroxyanthraquinone (2,6-DHAQ). In both cases, sodium hydride was used to fully deprotonate the anthraquinone precursors in anhydrous dimethyl sulfoxide or N, N-Dimethylformamide. Afterward, the deprotonated anthraquinone was reacted with 1,3-propanesultone at room temperature for 1 hour to afford 2,6-N-TSAQ or 2,6-O-DPSAQ. Benefiting from the high reactivity of 1,3-propanesultone, the reaction is readily happened at room temperature with high purity and yield, making it very suitable for mass production. 2,6-DPSAQ was synthesized from 2,6-DAAQ with three steps. First, 2,6-DAAQ was iodized to form 2,6-diiodoanthraquinone. Subsequently, it reacted with sodium allylsulfonate via Heck reaction followed by a hydrogenation step to yield 2,6-DPSAQ. The three-step reaction involving precious metal catalysts makes it less attractive compared with the one-step synthesis of 2,6-N-TSAQ and 2,6-O-DPSAQ. Since the laboratory cost of precursor 2,6-DAAQ is much lower than that of 2,6-DHAQ,[120] 2,6-N-TSAQ could be

the most inexpensive anthraquinone among the three at mass production scale, decreasing the capital cost of AORFBs.

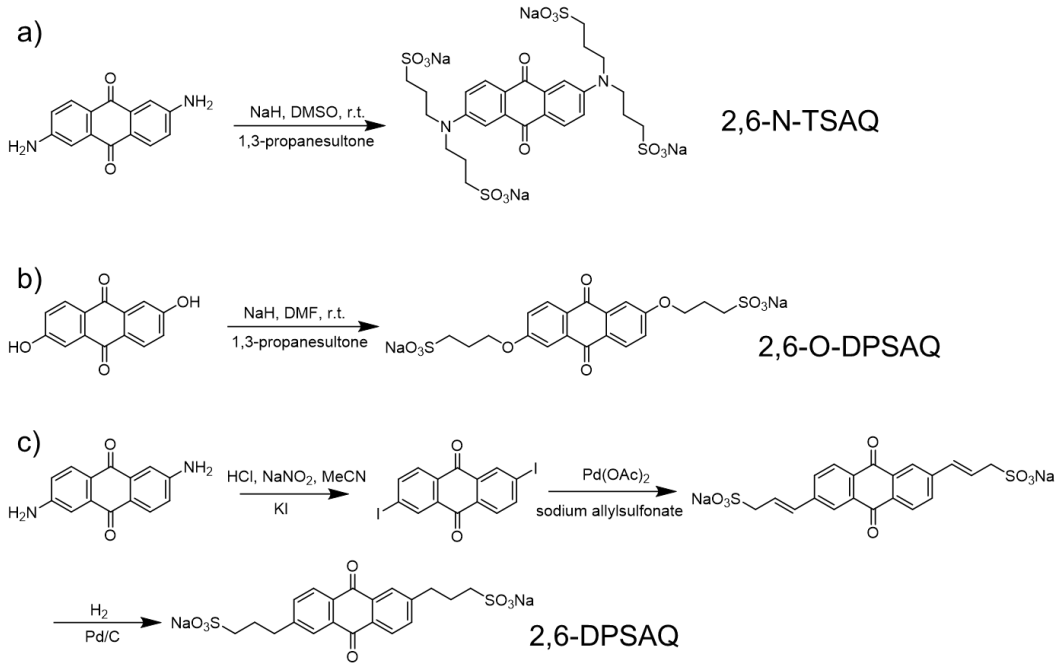

Figure 4.5 Synthetic routes for three different anthraquinones. a) 2,6-N-TSAQ; b) 2,6-O-DPSAQ; c) 2,6-DPSAQ.

Figure 4.6a exhibits the cyclic voltammograms (CV) of 2,6-DPSAQ, 2,6-O-DPSAQ, and 2,6-N-TSAQ. The reduction potential of 2,6-N-TSAQ is -0.62 V vs. SHE in 1M NaCl, which is 120 mV and 170 mV lower than that of 2,6-O-DPSAQ and 2,6-DPSAQ in 1M NaCl, respectively. The low redox potential of 2,6-N-TSAQ is attributed to the strong electron donating effect of N-alkyl group. It contributes to form a high working voltage and high power density flow battery. The water solubilities of 2,6-DPSAQ, 2,6-O-DPSAQ, and 2,6-N-TSAQ were shown in Figure 4.6b. Surprisingly, 2,6-O-DPSAQ exhibited an extremely low solubility of 10 mM in deionized water and 1 M lithium chloride, and an

even lower solubility of less than 5 mM in 1 M sodium chloride. The water solubility of 2,6-DPSAQ and 2,6-N-TSAQ are 0.3 M and 0.45 M, respectively. The solubility of 2,6-N-TSAQ could be boosted to 0.65 M with ammonium ion exchange. The ammonium cation, however, sacrifices the redox potential of 2,6-N-TSAQ as the local pH is always lower than the pKa2 of 9,10-dihydroxyanthracene, which is also observed in the reported 9,10-anthraquinone-2,7-disulfonic diammonium salt.[123]

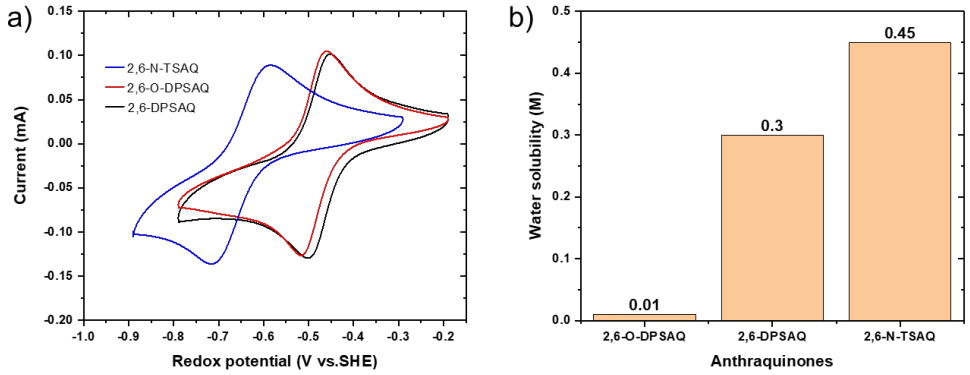

Figure 4.6 Electrochemical and physical properties of three different anthraquinones 2,6-DPSAQ, 2,6-N-TSAQ, and 2,6-O-DPSAQ. a) Cyclic voltammograms of 5 mM 2,6-N-TSAQ, 5 mM 2,6-DPSAQ in 1 M sodium chloride and 5 mM 2,6-O-TSAQ in 1 M lithium chloride with a scan rate of 100 mV/s; b) Water solubility comparison for 2,6-N-TSAQ, 2,6-O-DPSAQ and 2,6-DPSAQ.

Given the higher water solubility, lower redox potential and possible lower synthetic cost, 2,6-N-TSAQ was selected for further electrochemical study. The advantage of 2,6-N-TSAQ over other low redox potential anthraquinones[60, 120] is that it has four negative charges, thus the intramolecular Coulomb repulsion is very large so that its collison factor is low. Based on Marcus theory,[124] the disproportionation reaction that is known to cause the capacity decay in anthraquinone species[80, 85] is suppressed. The multiple negative

charges also decrease the molecular permeability across the cation exchange membrane, increasing the cell lifetime. The Pourbaix diagram of 2,6-N-TSAQ, as shown in Figure 4.7, indicates the molecule undergoes a two-proton/two-electron process below pH 10, a one-proton/two-electron process between pH 10–12, and it becomes pH independent at high pH (pH > 12) with a redox potential around -0.62 V vs. SHE. The pH in the Pourbaix diagram represents the local pH of anthraquinone molecules. In an unbuffered case, e.g., 1 M NaCl, though the initial pH is 7, reduction consumes two protons per anthraquinone molecule, immediately increasing the local pH, exhibiting a formal potential -0.62 V for 2,6-N-TSAQ which is equal to the redox potential in the high pH region. Based on the Pourbaix diagram, the pKa1 and pKa2 of reduced 2,6-N-TSAQ are calculated to be around 10 and 12, respectively, which are slightly higher than those of high redox potential anthraquinones.[58, 65, 66, 85] This is attributed to the strong electron donating effect of N-alkyl group decreasing the acidity of the hydroxy groups of the 9,10-dihydroxyanthracene (reduced state of anthraquinone).

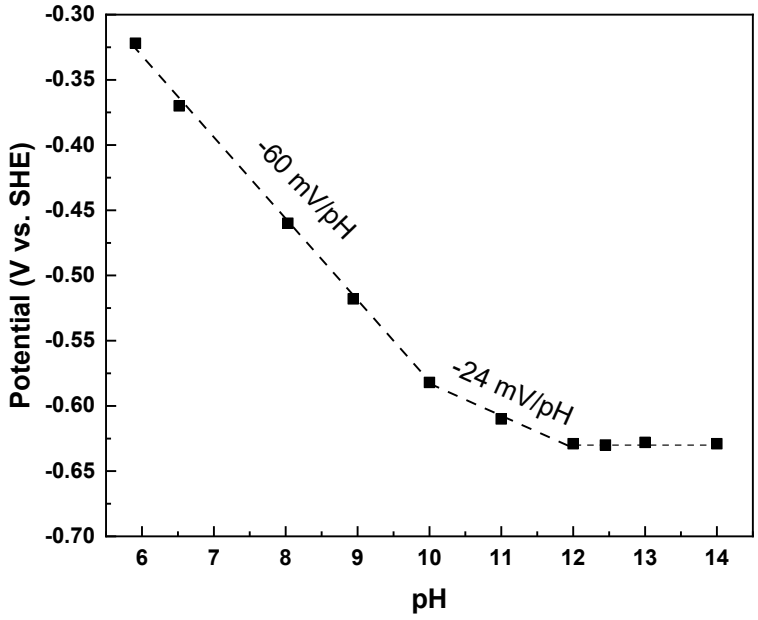

Figure 4.7 Pourbaix diagram of 2,6-N-TSAQ.

Polarization experiments of a 0.1 M 2,6-N-TSAQ/ferrocyanide full cell at pH 14 were performed at various states of charge. The negolyte comprised 5 mL of 0.1 M 2,6-N-TSAQ at pH 14 and posolyte contained 30 mL of 0.1 M potassium ferrocyanide and 0.02 M potassium ferricyanide at pH 14 to ensure that the negolyte was always the capacity limiting side. The cell was constructed from graphite flow plates and AvCarb carbon electrodes, separated by a Nafion 212 membrane pretreated in 1 M KOH. To access the full capacity, the cell was charged and discharged to 1.4 V and 0.6 V, respectively, with a potential hold until the current dropped to 2 mA/cm^2. The open-circuit voltage (OCV) increases from 0.8 V to 1.31 V as the state of charge (SOC) increases from ~0% to ~100% (Figure 4.8a). The OCV at 1%, 20%, 50% and 90% SOC are around 1.02 V, 1.11 V, 1.14 V

and 1.18 V, respectively. The OCV increase of 0.2 V from ~0 to 1% SOC, and of only 0.08 V from 10% to 90% SOC, indicate the full utilization of 2,6-N-TSAQ under the operating conditions and that the redox potential of 2,6-N-TSAQ is a constant during cycling, in qualitative consistency with the Nernst equation. The OCV at 50% SOC is similar to the cell voltage expected from the CV result. The peak galvanic power density at 10% SOC was 0.15 W cm^{-2}, increasing to 0.18 W cm^{-2} at 90% SOC (Figure 4.8b), which is higher than that of many other redox organics.[40, 66, 68, 79, 89, 98, 101, 106] The power density is mainly limited by the high-frequency area-specific resistance, which is dominated by the membrane resistance (Figure 4.8a) with a value around 1.6 $\Omega \cdot cm^2$. Therefore, the power density is expected to be improved with a lower resistance membrane.

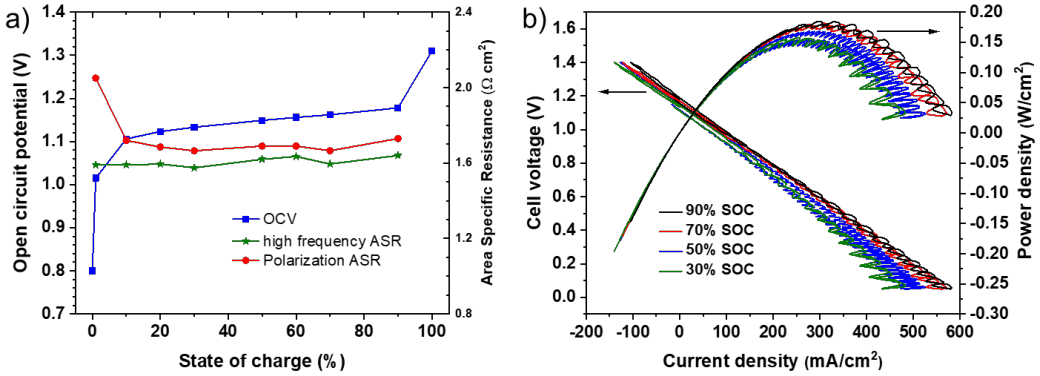

Figure 4.8 Polarization experiments of 2,6-N-TSAQ. a) open circuit voltage of 0.1 M 2,6-N-TSAQ/0.1 M potassium ferrocyanide + 0.02 M potassium ferricyanide full cell at pH 14; b) cell voltage and power density versus current density at room temperature at 10%, 30%, 50%, 70%, and 90% SOC. Cell configuration: 5 mL of 0.1 M 2,6-N-TSAQ pH 14 | 30 mL of 0.1 M $K_4Fe(CN)_6$, 0.02 M $K_3Fe(CN)_6$, pH 14. Nafion^{TM} 212 was used as the ion-selective membrane between the AvCarb electrodes.

Long-term cycling testing of 0.1 M 2,6-N-TSAQ/ferrocyanide was performed with the same cell. The cell was cycled at 40 mA cm^{-2} with potential holds at 1.4 V for charging and 0.6 V for discharging until the current density dropped to 2 mA cm^{-2}. The initial discharge capacity was 4.764 Ah L^{-1}, corresponding to a capacity utilization of 88.9% of the theoretical value. However, the OCV at different SOC values in Figure 4.8a and the typical voltage profile in Figure 4.9c indicates it accesses the complete capacity of 2,6-N-TSAQ under such conditions. The differences between the actual capacity and the theoretical value could come from non-redox active impurities such as water or salts in the sample. After 9 days of full SOC range cycling, the discharge capacity decreased to 4.754 Ah/L, corresponding to a temporal capacity fade rate of 0.025%/day or a cycle-denominated capacity fade rate of 0.00024%/cycle. The average coulombic efficiency was determined

to be above 99.9%. The voltage vs. capacity profile at different cycles in Figure 4c are almost invariant, indicating the ultra-stable cell performance of 2,6-N-TSAQ at pH 14. These results stand out as among the most stable electrolytes for AORFBs ever reported.[67]

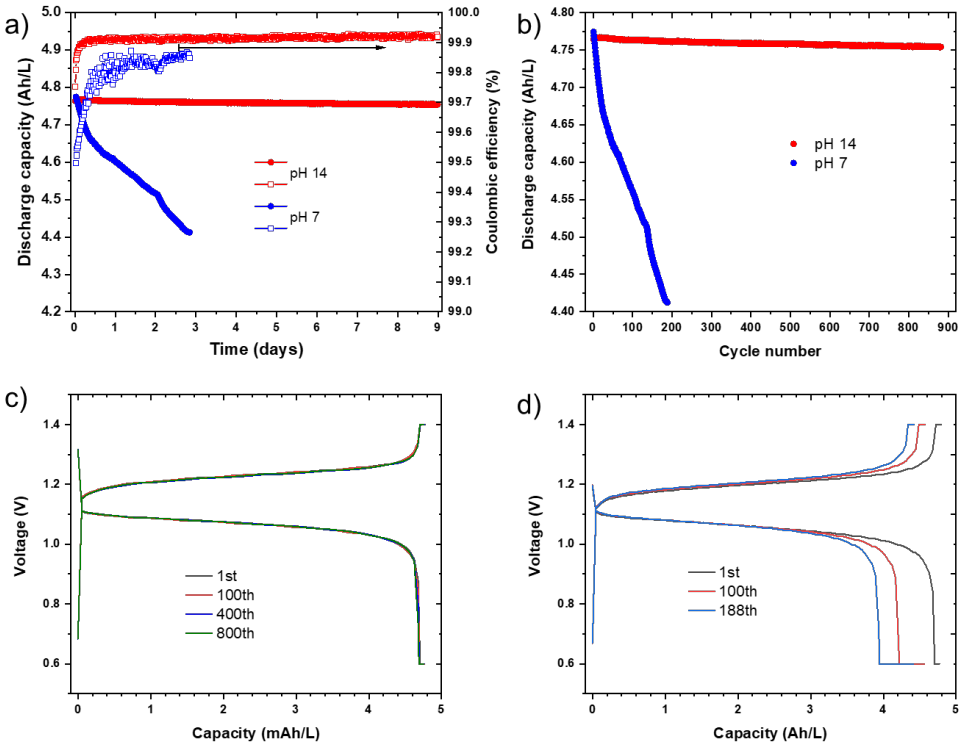

Figure 4.9 Cell performance of 0.1 M 2,6-N-TSAQ/ferrocyanide cell, 2,6-N-TSAQ as the capacity limiting side. a) Discharge capacity and Coulombic efficiency versus cycle time at pH 7 and 14; b) Discharge capacity and Coulombic efficiency versus cycle number at pH 7 and 14; c) Charge-discharge voltage profile of 2,6-N-TSAQ from selected cycles at pH 14 in Figure 4.9b; d) Charge-discharge voltage profile of 2,6-N-TSAQ from selected cycles at pH 7 in Figure 4.9b.

For comparison, the long-term cycling of the 0.1 M 2,6-N-TSAQ/ferrocyanide cell was operated at neutral condition (1 M sodium chloride) but, otherwise, the same conditions. The initial volumetric capacity was 4.774 Ah L^{-1}, which is similar to that at pH 14. After 2.84 days cycling, the discharge capacity dropped to 4.412 Ah/L, corresponding

to a capacity fade rate of 2.6%/day, which is around 2 orders magnitude higher than that at pH 14. And the coulombic efficiency is around 99.8% over the whole cycling process, which is slightly lower than that at pH 14. Furthermore, the discharge capacity contribution from potential at the discharge voltage limit of 0.6 V increases, and energy efficiency decreases, with cycling, as shown in Figure 4.10, further illustrating the instability of 2,6-N-TSAQ at neutral condition. To investigate the origin of instability of 2,6-N-TSAQ at neutral condition, both oxidized and reduced forms of 2,6-N-TSAQ were stored in 1 M NaCl at 65 °C for 8 days. As shown in Figure 4.11, no apparent decomposition was found in the ^{1}H NMR of the oxidized state, indicating the excellent stability of 2,6-N-TSAQ in its oxidize state. In contrast, the reduced sample 2,6-N-TSAQ shows a large quantity of decomposition after 8 days treatment. Our working hypothesis to interpret these results is that the reduced 2,6-N-TSAQ undergoes the disproportionation reaction that is known in anthraquinone.[80, 85]

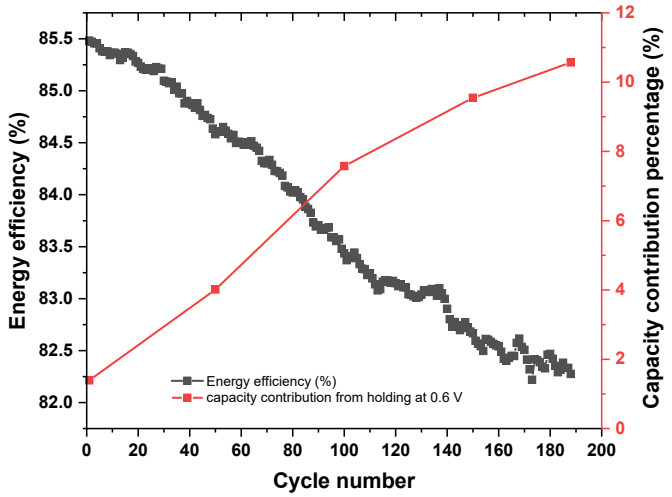

Figure 4.10 Energy efficiency and capacity contribution percentage at discharge voltage limit of 0.6 V versus cycle number of the 2,6-N-TSAQ/ferrocyanide cell in 1 M NaCl solution.

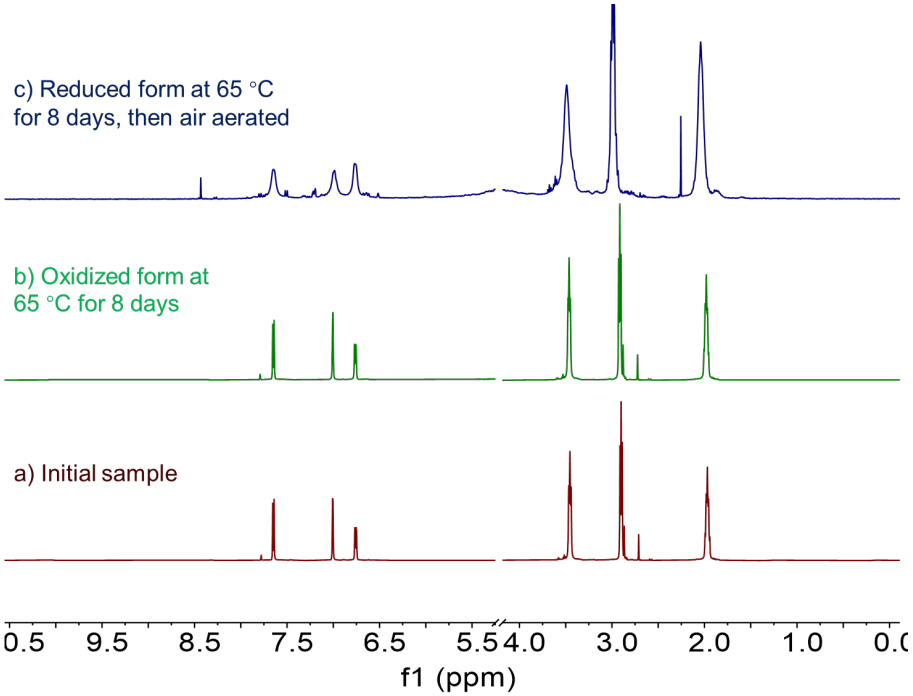

Figure 4.11 ^{1}H NMR spectra (500 MHz) of 2,6-N-TSAQ in D_2O solvent. (a) initial 2,6-N-TSAQ; (b) 0.1 M 2,6-N-TSAQ held at 65 °C for 8 days in 1 M sodium chloride; (c) 0.1 M reduced state of 2,6-N-TSAQ held at 65 °C for 8 days in 1 M sodium chloride.

The substantial difference in the stability of reduced anthraquinone at pH 7 and 14 could be explained by the following thermodynamic arguments. As shown in Figure 4.12, the disproportionation reaction of reduced anthraquinone (r-AQ) was intrinsically the overall reaction of the two half reactions: anthraquinone/r-AQ and r-AQ/anthrone. The Gibbs free energy change $\Delta G^{\circ\prime}$ at a quasi-standard condition could be expressed as $\Delta G^{\circ\prime} = -2 \times F \times (E_2 - E_1)$, quasi standard condition represents a state that similar to the standard condition except the pH is fixed at a certain value, and E_1 and E_2 are the electrode redox potential of the two half-reactions at quasi standard condition. The Pourbaix diagram of anthraquinone, r-AQ and anthrone are shown in Figure 4.12. The redox reaction of anthraquinone/r-AQ and r-AQ/anthrone are proton-coupled electron transfer reaction. When the local pH < pKa1 of r-AQ, both redox pairs anthraquinone/r-AQ and r-AQ/anthrone undergo a two-proton/two-electron process. When the local pH is between pKa1 of r-AQ and pKa of anthrone, anthraquinone/r-AQ undergoes one-proton/two-electron process, and r-AQ/anthrone undergoes three-proton/two-electron reaction. When the local pH increased to pKa ~ pKa2 region, anthraquinone/r-AQ still experiences one-proton/two-electron process, while r-AQ/anthrone undertakes two-proton/two-electron process. When pH is above pKa2 of r-AQ, the redox reaction of anthraquinone/r-AQ becomes pH independent, and r-AQ/anthrone undergoes three-proton/two-electron reaction. The Gibbs free energy difference of one molar anthrone formation at pH 14 and 12, as shown in Figure 4.12b is around

$$\Delta G = -2 \times 96485 \text{ C/mol} \times (-89.5 \text{ mV/pH} \times 2 \text{ pH}) \times 1 \text{ V} / (1000 \text{ mV}) = 34.54 \text{ kJ/mol}$$

Similarly, the Gibbs free energy difference of one molar anthrone formation at pH 14 and 10 could be as large as 46.13~57.70 kJ/mol depending on the pKa1, pKa and pKa2 values, indicating that anthrone formation is greatly suppressed at pH 14 than that at lower pH values. Consequently, anthraquinone-based flow batteries for which anthrone formation is the dominant loss mechanism exhibit much better cycling performance at high pH than that at a lower pH. Furthermore, the Gibbs free energy change for anthrone formation reaction at a 100% SOC state (no anthrone, no anthraquinone, and 100% 9,10-dihydroxyanthracene) is always negative, indicating that for any given anthraquinone, the disproportionation reaction at full SOC state is always thermodynamically favorable. Additionally, the redox potential E1 for anthraquinone reduction at quasi standard condition is equal to that of anthraquinone reduction at 50% SOC cycling. When the state of charge of anthraquinone increases from 90% to 99%, the Δ G for anthrone formation decreases around $8.314 \text{ J/mol/K} \times 298.15 \text{ K} \times (\ln \frac{0.1}{0.9^2} - \ln \frac{0.01}{0.99^2}) = 6.18 \text{ kJ/mol kJ/mol}$ if assume the change of anthrone concentration is negligible. And if the state of charge of anthraquinone cycling increases from 90% to 99.9%, the Gibbs free energy change for anthrone formation decreases around 11.93 kJ/mol. Therefore, to suppress anthrone formation, charging to high SOC should be avoided, e.g., it is desired not to conduct a potential hold at high potential. However, to accurately measure a capacity fade rate, achieving high SOC is necessary. In this case, one could do a potential hold cycle after, say, every 30 cycles of galvanostatic

cycling. And since the increase of ΔG for anthrone formation is more significant for pH tuning than control SOC and also the beneficial time per cycle for SOC management (only high SOC time e.g., 90%~99% SOC) is far shorter than that of pH tuning (whole cycle time, e.g., 1%~99% SOC), SOC management is less effective than strong pH method to improve anthraquinone cycling stability. Similarly, we could conclude that the capacity fade rate will decrease as time passed if avoid anthrone oxidation because ΔG for anthrone formation increase as the accumulation of anthrone. And since the entropy change is positive for the disproportionation reaction, it is suggested to avoid both the full SOC state and high temperature operation.

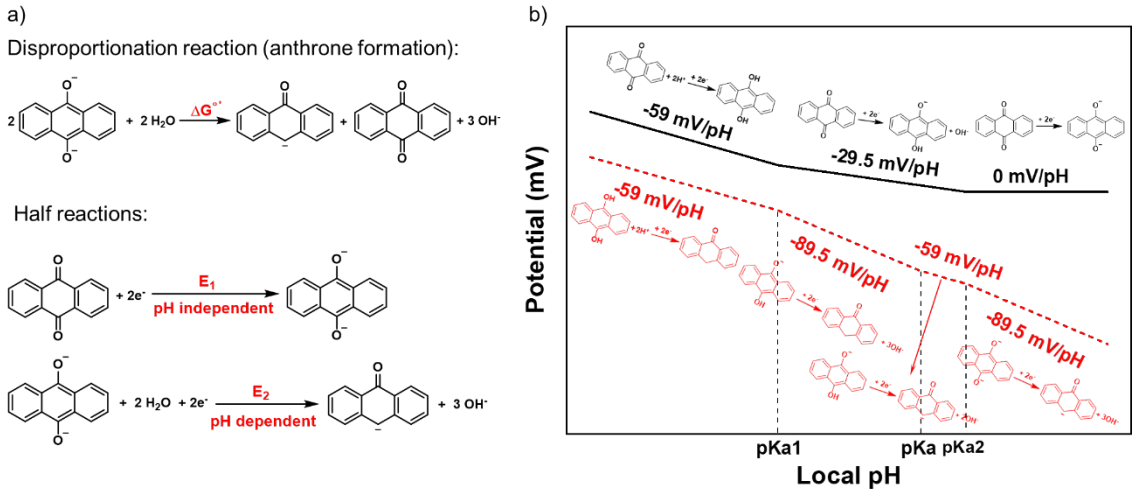

Figure 4.12 Thermodynamic analysis of anthraquinone disproportionation reaction. a) Disproportionation reaction of r-AQ at pH above its pKa2 and the corresponding two half reactions; b) Representative Pourbaix diagram of anthraquinone, r-AQ, and anthrone. The pKa1 and pKa2 belong to r-AQ, and pKa (around 10) belongs to anthrone.[125] The water molecules in the half reactions were neglected in Figure 4.12b due to the room limitation.

4.4 Conclusion

In summary, we synthesized three anthraquinone derivatives, carbon-linked, nitrogen-linked and oxygen-linked anthraquinones. The nitrogen-linked anthraquinone showed the lowest redox potential due to its strongest electron donating effect. It's synthesized from inexpensive precursors with a one-step *N*-alkylation method; therefore, the mass production cost might be very low. Although with four negative charges and high coulombic repulsion, its cycling performance is bad at neutral condition with a capacity fade rate of 2.6%/day. The capacity fade rate decreased by two orders of magnitude at pH 14, making it to be one of the most stable redox organics ever reported. The great difference in anthraquinone cycling stability at different pH values is explained by considering the thermodynamics of the numerous chemical and electrochemical reactions available to the system. This work shows the significant improvements that can be made with a better understanding of the capacity fade mechanism and its thermodynamics, and it shows the great potential of organics synthesis towards low-cost and stable electrolytes for AORFBs.

References

1. Severinghaus, J. P.; Brook, E. J., Abrupt climate change at the end of the last glacial period inferred from trapped air in polar ice. *Science* **1999,** *286* (5441), 930-934.

2. Ramaswamy, V.; Schwarzkopf, M. D.; Randel, W. J.; Santer, B. D.; Soden, B. J.; Stenchikov, G. L., Anthropogenic and natural influences in the evolution of lower stratospheric cooling. *Science* **2006,** *311* (5764), 1138-1141.

3. National Oceanic and Atmospheric Administration, Trends in atmospheric carbon dioxide. https://www.esrl.noaa.gov/gmd/ccgg/trends/, accessed in April **2021**.

4. US energy information administration, Electricity generation, capacity, and sales in the United States. https://www.eia.gov/energyexplained/electricity/electricity-in-the-us-generation-capacity-and-sales.php, accessed in April **2021**.

5. Rugolo, J.; Aziz, M. J., Electricity storage for intermittent renewable sources. *Energy Environ. Sci.* **2012,** *5* (5), 7151-7160.

6. Dunn, B.; Kamath, H.; Tarascon, J. M., Electrical energy storage for the grid: a battery of choices. *Science* **2011,** *334* (6058), 928-35.

7. Uría-Martínez. R.; Johnson, M. M.; Shan, R., U.S. hydropower market report. January **2021**.

8. Al Shaqsi, A. Z.; Sopian, K.; Al-Hinai, A., Review of energy storage services, applications, limitations, and benefits. *Energy Rep.* **2020,** *6*, 288-306.

9. Battery storage power station. *Wikipedia* accessed in April **2021**.

10. Yang, Z.; Zhang, J.; Kintner-Meyer, M. C.; Lu, X.; Choi, D.; Lemmon, J. P.;

Liu, J., Electrochemical energy storage for green grid. *Chem. Rev.* **2011,** *111* (5), 3577-613.

11. Darling, R. M.; Gallagher, K. G.; Kowalski, J. A.; Ha, S.; Brushett, F. R., Pathways to low-cost electrochemical energy storage: a comparison of aqueous and nonaqueous flow batteries. *Energy Environ. Sci.* **2014,** *7* (11), 3459-3477.

12. Soloveichik, G. L., Flow batteries: current status and trends. *Chem. Rev.* **2015,** *115* (20), 11533-58.

13. Goulet, M.-A.; Aziz, M. J., Flow battery molecular reactant stability determined by symmetric cell cycling methods. *J. Electrochem. Soc.* **2018,** *165* (7), A1466-A1477.

14. Kowalski, J. A.; Neyhouse, B. J.; Brushett, F. R., The impact of bulk electrolysis cycling conditions on the perceived stability of redox active materials. *Electrochem. Commun.* **2020,** *111*, 106625.

15. Li, Z.; Pan, M. S.; Su, L.; Tsai, P. C.; Badel, A. F.; Valle, J. M.; Eiler, S. L.; Xiang, K.; Brushett, F. R.; Chiang, Y. M., Air-breathing aqueous sulfur flow battery for ultralow-cost long-duration electrical storage. *Joule* **2017,** *1* (2), 306-327.

16. Rychick, M., Skyllas-Kazacos, M., Characteristics of a new all-vanadium redox flow battery. *J. Power Sources* **1988,** *22*, 9.

17. Li, L. Y.; Kim, S.; Wang, W.; Vijayakumar, M.; Nie, Z. M.; Chen, B. W.; Zhang, J. L.; Xia, G. G.; Hu, J. Z.; Graff, G.; Liu, J.; Yang, Z. G., A stable vanadium redox-flow battery with high energy density for large-scale energy storage. *Adv. Energy Mater.* **2011,** *1* (3), 394-400.

18. Zhang, Y.; Liu, L.; Xi, J.; Wu, Z.; Qiu, X., The benefits and limitations of electrolyte mixing in vanadium flow batteries. *Appl. Energy* **2017,** *204*, 373-381.

19. Vijayakumar, M.; Bhuvaneswari, M.; Nachimuthu, P.; Schwenzer, B.; Kim, S.; Yang, Z.; Liu, J.; Graff, G. L.; Thevuthasan, S.; Hu, J., Spectroscopic investigations of the fouling process on Nafion membranes in vanadium redox flow batteries. *J. membrane sci.* **2011,** *366* (1-2), 325-334.

20. El Hage, R.; Chauvet, F.; Biscans, B.; Cassayre, L.; Maurice, L.; Tzedakis, T., Kinetic study of the dissolution of vanadyl sulfate and vanadium pentoxide in sulfuric acid aqueous solution. *Chem. Eng. Sci.* **2019,** *199*, 123-136.

21. Mongird, K.; Viswanathan, V.; Alam, J.; Vartanian, C.; Sprenkle, V., 2020 grid energy storage technology cost and performance assessment. **2020**.

22. Luo, J. A.; Hu, B.; Hu, M. W.; Zhao, Y.; Liu, T. L., Status and prospects of organic redox flow batteries toward sustainable energy storage. *ACS Energy Lett.* **2019,** *4* (9), 2220-2240.

23. G. Ciprios, W. E., Jr., and P. G. Grimes, Redox bulk energy storage system study. *NASA Rep. CR-135206* **1977,** *Feb. 10, 1977*.

24. EPRI, N., BEWAG, in Proc. 2nd Int. Conf. Batteries utility energy storage, Newport, CA, USA, 1989. **1989**.

25. Gahn, R. F.; Hagedorn, N. H.; Johnson, J. A., Cycling performance of the iron-chromium redox energy storage system. National Aeronautics and Space Administration:

1985.

26. Cheng, D. S.; Hollax, E., The influence of thallium on the redox reaction Cr^{3+}/Cr^{2+}. *J. Electrochem. Soc.* **1985,** *132* (2), 269-273.

27. Wu, C. D.; Scherson, D. A.; Calvo, E. J.; Yeager, E. B.; Reid, M. A., A bismuth-based electrocatalyst for the chromous-chromic couple in acid electrolytes. *J. Electrochem. Soc.* **1986,** *133* (10), 2109-2112.

28. Zeng, Y. K.; Zhao, T. S.; An, L.; Zhou, X. L.; Wei, L., A comparative study of all-vanadium and iron-chromium redox flow batteries for large-scale energy storage. *J. Power Sources* **2015,** *300*, 438-443.

29. Bae, C. H.; Roberts, E. P. L.; Dryfe, R. A. W., Chromium redox couples for application to redox flow batteries. *Electrochim. Acta* **2002,** *48* (3), 279-287.

30. Modiba, P.; Matoetoe, M.; Crouch, A. M., Kinetics study of transition metal complexes (Ce–DTPA, Cr–DTPA and V–DTPA) for redox flow battery applications. *Electrochim. Acta* **2013,** *94*, 336-343.

31. Bae*, C.; Roberts, E. P. L.; Chakrabarti, M. H.; Saleem, M., All-chromium redox flow battery for renewable energy storage. *Int. J. Green Energy* **2011,** *8* (2), 248-264.

32. Ogino, H.; Nagata, T.; Ogino, K., Redox potentials and related thermodynamic parameters of (diaminopolycarboxylato)metal(III/II) redox couples. *Inorganic Chemistry* **1989,** *28* (19), 3656-3659.

33. Robb, B. H.; Farrell, J. M.; Marshak, M. P., Chelated chromium electrolyte enabling

high-voltage aqueous flow batteries. *Joule* **2019,** *3* (10), 2503-2512.

34. Gong, K.; Xu, F.; Grunewald, J. B.; Ma, X. Y.; Zhao, Y.; Gu, S.; Yan, Y. S., All-soluble all-iron aqueous redox-flow battery. *ACS Energy Lett.* **2016,** *1* (1), 89-93.

35. Luo, J.; Hu, B.; Debruler, C.; Bi, Y. J.; Zhao, Y.; Yuan, B.; Hu, M. W.; Wu, W. D.; Liu, T. L., Unprecedented capacity and stability of ammonium ferrocyanide catholyte in ph neutral aqueous redox flow batteries. *Joule* **2019,** *3* (1), 149-163.

36. Esswein, A. J.; Goeltz, J.; Amadeo, D. High solubility iron hexacyanides. Application 2014/0051003 A1, 2/20/2014, **2014**.

37. Luo, J.; Sam, A.; Hu, B.; DeBruler, C.; Wei, X. L.; Wang, W.; Liu, T. L., Unraveling pH dependent cycling stability of ferricyanide/ferrocyanide in redox flow batteries. *Nano Energy* **2017,** *42*, 215-221.

38. Páez, T.; Martínez-Cuezva, A.; Palma, J.; Ventosa, E., Revisiting the cycling stability of ferrocyanide in alkaline media for redox flow batteries. *J. Power Sources* **2020,** *471*, 228453.

39. Hu, B.; DeBruler, C.; Rhodes, Z.; Liu, T. L., Long-cycling aqueous organic redox flow battery (aorfb) toward sustainable and safe energy storage. *J. Am. Chem. Soc.* **2017,** *139* (3), 1207-1214.

40. Beh, E. S.; De Porcellinis, D.; Gracia, R. L.; Xia, K. T.; Gordon, R. G.; Aziz, M. J., A neutral ph aqueous organic-organometallic redox flow battery with extremely high capacity retention. *ACS Energy Lett.* **2017,** *2* (3), 639-644.

41. Yu, J.; Salla, M.; Zhang, H.; Ji, Y.; Zhang, F.; Zhou, M.; Wang, Q., A robust anionic sulfonated ferrocene derivative for pH-neutral aqueous flow battery. *Energy Storage Mater.* **2020,** *29*, 216-222.

42. Tang, B.; Shan, L.; Liang, S.; Zhou, J., Issues and opportunities facing aqueous zinc-ion batteries. *Energy Environ. Sci.* **2019,** *12* (11), 3288-3304.

43. Yuan, Z.; Yin, Y.; Xie, C.; Zhang, H.; Yao, Y.; Li, X., Advanced materials for zinc-based flow battery: development and challenge. *Adv. Mater.* **2019,** *31* (50), 1902025.

44. Li, Z.; Lu, Y. C., Material design of aqueous redox flow batteries: fundamental challenges and mitigation strategies. *Adv. Mater.* **2020,** *32* (47), 2002132.

45. Zhang, J.; Jiang, G. P.; Xu, P.; Kashkooli, A. G.; Mousavi, M.; Yu, A. P.; Chen, Z. W., An all-aqueous redox flow battery with unprecedented energy density. *Energy Environ. Sci.* **2018,** *11* (8), 2010-2015.

46. Gong, K.; Ma, X. Y.; Conforti, K. M.; Kuttler, K. J.; Grunewald, J. B.; Yeager, K. L.; Bazant, M. Z.; Gu, S.; Yan, Y. S., A zinc-iron redox-flow battery under $100 per kW h of system capital cost. *Energy Environ. Sci.* **2015,** *8* (10), 2941-2945.

47. Yuan, Z.; Duan, Y.; Liu, T.; Zhang, H.; Li, X., Toward a low-cost alkaline zinc-iron flow battery with a polybenzimidazole custom membrane for stationary energy storage. *iScience* **2018,** *3*, 40-49.

48. Yuan, Z.; Liu, X.; Xu, W.; Duan, Y.; Zhang, H.; Li, X., Negatively charged nanoporous membrane for a dendrite-free alkaline zinc-based flow battery with long cycle

life. *Nat. Commun.* **2018,** *9* (1), 3731.

49. Park, M.; Beh, E. S.; Fell, E. M.; Jing, Y.; Kerr, E. F.; De Porcellinis, D.; Goulet, M. A.; Ryu, J.; Wong, A. A.; Gordon, R. G.; Cho, J.; Aziz, M. J., A high voltage aqueous zinc-organic hybrid flow battery. *Adv. Energy Mater.* **2019,** *9* (25), 1900694.

50. Xie, C.; Zhang, H.; Xu, W.; Wang, W.; Li, X., A long cycle life, self-healing zinc-iodine flow battery with high power density. *Angew. Chem. Int. Ed.* **2018,** *57* (35), 11171-11176.

51. Zhang, S.; Guo, W.; Yang, F.; Zheng, P.; Qiao, R.; Li, Z., Recent progress in polysulfide redox-flow batteries. *Batteries & Supercaps* **2019,** *2* (7), 627-637.

52. Wei, X.; Xia, G.-G.; Kirby, B.; Thomsen, E.; Li, B.; Nie, Z.; Graff, G. G.; Liu, J.; Sprenkle, V.; Wang, W., An aqueous redox flow battery based on neutral alkali metal ferri/ferrocyanide and polysulfide electrolytes. *J. Electrochem. Soc.* **2015,** *163* (1), A5150-A5153.

53. Su, L.; Badel, A. F.; Cao, C.; Hinricher, J. J.; Brushett, F. R., Toward an inexpensive aqueous polysulfide–polyiodide redox flow battery. *Ind. Eng. Chem. Res.* **2017,** *56* (35), 9783-9792.

54. Ma, D.; Hu, B.; Wu, W.; Liu, X.; Zai, J.; Shu, C.; Tadesse Tsega, T.; Chen, L.; Qian, X.; Liu, T. L., Highly active nanostructured CoS_2/CoS heterojunction electrocatalysts for aqueous polysulfide/iodide redox flow batteries. *Nat. Commun.* **2019,**

10 (1), 3367.

55. Wang, L.; Wang, X.; Liu, J.; Yang, H.; Fu, C.; Xia, Y.; Liu, T., A rechargeable metal-free full-liquid sulfur–bromine battery for sustainable energy storage. *J. Mater. Chem. A* **2018,** *6* (42), 20737-20745.

56. Li, Z.; Lu, Y.-C., Polysulfide-based redox flow batteries with long life and low levelized cost enabled by charge-reinforced ion-selective membranes. *Nat. Energy* **2021**, https://doi.org/10.1038/s41560-021-00804-x.

57. Konyratbekova, S. S.; Baikonurova, A.; Ussoltseva, G. A.; Erust, C.; Akcil, A., Thermodynamic and kinetic of iodine–iodide leaching in gold hydrometallurgy. *Trans. Nonferrous Met. Soc. China* **2015,** *25* (11), 3774-3783.

58. Huskinson, B. T.; Marshak, M. P.; Suh, C.; Er, S.; Gerhardt, M. R.; Galvin, C. J.; Chen, X.; Aspuru-Guzik, A.; Gordon, R. G.; Aziz, M. J., A metal-free organic-inorganic aqueous flow battery. *Nature* **2014,** *505* (7482), 195-8.

59. Yang, B.; Hoober-Burkhardt, L.; Wang, F.; Surya Prakash, G. K.; Narayanan, S. R., An inexpensive aqueous flow battery for large-scale electrical energy storage based on water-soluble organic redox couples. *J. Electrochem. Soc.* **2014,** *161* (9), A1371-A1380.

60. Lin, K.; Chen, Q.; Gerhardt, M. R.; Tong, L.; Kim, S. B.; Eisenach, L.; Valle, A. W.; Hardee, D.; Gordon, R. G.; Aziz, M. J.; Marshak, M. P., Alkaline quinone flow battery. *Science* **2015,** *349* (6255), 1529-32.

61. Lin, K.; Gomez-Bombarelli, R.; Beh, E. S.; Tong, L.; Chen, Q.; Valle, A.;

Aspuru-Guzik, A.; Aziz, M. J.; Gordon, R. G., A redox-flow battery with an alloxazine-based organic electrolyte. *Nat. Energy* **2016,** *1* (9), 16102.

62. Yang, Z.; Tong, L.; Tabor, D. P.; Beh, E. S.; Goulet, M. A.; De Porcellinis, D.; Aspuru-Guzik, A.; Gordon, R. G.; Aziz, M. J., Alkaline benzoquinone aqueous flow battery for large-scale storage of electrical energy. *Adv. Energy Mater.* **2018,** *8* (8), 1702056.

63. Hollas, A.; Wei, X. L.; Murugesan, V.; Nie, Z. M.; Li, B.; Reed, D.; Liu, J.; Sprenkle, V.; Wang, W., A biomimetic high-capacity phenazine-based anolyte for aqueous organic redox flow batteries. *Nat. Energy* **2018,** *3* (6), 508-514.

64. DeBruler, C.; Hu, B.; Moss, J.; Liu, X. A.; Luo, J. A.; Sun, Y. J.; Liu, T. L., Designer two-electron storage viologen anolyte materials for neutral aqueous organic redox flow batteries. *Chem* **2017,** *3* (6), 961-978.

65. Kwabi, D. G.; Lin, K.; Ji, Y.; Kerr, E. F.; Goulet, M.-A.; De Porcellinis, D.; Tabor, D. P.; Pollack, D. A.; Aspuru-Guzik, A.; Gordon, R. G.; Aziz, M. J., Alkaline quinone flow battery with long lifetime at pH 12. *Joule* **2018,** *2* (9), 1907-1908.

66. Ji, Y.; Goulet, M. A.; Pollack, D. A.; Kwabi, D. G.; Jin, S.; Porcellinis, D.; Kerr, E. F.; Gordon, R. G.; Aziz, M. J., A phosphonate-functionalized quinone redox flow battery at near-neutral ph with record capacity retention rate. *Adv. Energy Mater.* **2019,** *9* (12), 1900039.

67. Kwabi, D. G.; Ji, Y.; Aziz, M. J., Electrolyte lifetime in aqueous organic redox flow batteries: A critical review. *Chem. Rev.* **2020,** *120* (14), 6467–6489.

68. Jin, S.; Jing, Y.; Kwabi, D. G.; Ji, Y.; Tong, L.; De Porcellinis, D.; Goulet, M. A.; Pollack, D. A.; Gordon, R. G.; Aziz, M. J., A water-miscible quinone flow battery with high volumetric capacity and energy density. *ACS Energy Lett.* **2019,** *4* (6), 1342-1348.

69. Hall, J.; Perkin, A. G., Reduction products of the hydroxyanthraquinones Part II. *J. Chem. Soc.* **1923,** *123*, 2029-2037.

70. Shimizu, A.; Takenaka, K.; Handa, N.; Nokami, T.; Itoh, T.; Yoshida, J. I., Liquid quinones for solvent-free redox flow batteries. *Adv. Mater.* **2017,** *29* (41), 1606592.

71. Kuimov, V. A.; Gusarova, N. K.; Malysheva, S. F.; Trofimov, B. A., Transition metal-free regioselective access to 9,10-dihydroanthracenes via the reaction of anthracenes with elemental phosphorus in the KOH/DMSO system. *Tetrahedron Lett.* **2018,** *59* (52), 4533-4536.

72. Dieterich, V.; Milshtein, J. D.; Barton, J. L.; Carney, T. J.; Darling, R. M.; Brushett, F. R., Estimating the cost of organic battery active materials: a case study on anthraquinone disulfonic acid. *Translational Materials Research* **2018,** *5* (3), 034001.

73. Das, C. K.; Das, N. S., Oxidation of anthracene to anthraquinone in liquid-phase with an air/oxygen/nitric acid system. *J. Chem. Technol. Biotechnol.* **1982,** *32* (6), 643-649.

74. Rodríguez, F.; Blanco, M. D.; Adrados, L. F.; Burillo, J.; Tijero, J. F., Selective oxidation of anthracene to anthraquinone in acetic acid with air in presence of nitric acid. *Tetrahedron lett.* **1989,** *30* (18), 2417-2420.

75. Tandon, P. K.; Baboo, R.; Singh, A. K., Simple and economical conversion of organic compounds with H_2O_2 catalyzed by ruthenium (III) chloride. *Appl. Organomet. Chem.* **2006,** *20* (1), 20-23.

76. Hall, J.; Perkin, A. G., CCXXIV.—Reduction products of the hydroxyanthraquinones. Part II. *J. Chem. Soc., Trans.* **1923,** *123* (0), 2029-2037.

77. Kestin, J.; Khalifa, H. E.; Correia, R. J., Tables of the dynamic and kinematic viscosity of aqueous KCl solutions in the temperature range 25–150 °C and the pressure range 0.1–35 MPa. *J. Phys. Chem. Ref. Data* **1981,** *10* (1), 57-70.

78. Weber, A. Z.; Mench, M. M.; Meyers, J. P.; Ross, P. N.; Gostick, J. T.; Liu, Q. H., Redox flow batteries: a review. *J. Appl. Electrochem.* **2011,** *41* (10), 1137-1164.

79. Hu, B.; Luo, J.; Hu, M.; Yuan, B.; Liu, T. L., A pH-neutral, metal-free aqueous organic redox flow battery employing an ammonium anthraquinone anolyte. *Angew. Chem. Int. Ed.* **2019,** *58* (46), 16629-16636.

80. Goulet, M.-A.; Tong, L.; Pollack, D. A.; Tabor, D. P.; Odom, S. A.; Aspuru-Guzik, A.; Kwan, E. E.; Gordon, R. G.; Aziz, M. J., Extending the lifetime of organic flow batteries via redox state management. *J. Am. Chem. Soc.* **2019,** *141* (20), 8014-8019.

81. McCann, G. M.; McDonnell, C. M.; Magris, L.; O'Ferrall, R. A. M., Enol–keto tautomerism of 9-anthrol and hydrolysis of its methyl ether. *J. Chem. Soc., Perkin Trans. 2* **2002,** 784-795.

82. Spotnitz, R. M.; Kreh, R. P.; Lundquist, J. T.; Press, P. J., Mediated electrosynthesis

with cerium (Iv) in methanesulphonic acid. *J. Appl. Electrochem.* **1990,** *20* (2), 209-215.

83. Kreh, R. P.; Spotnitz, R. M.; Lundquist, J. T., Mediated electrochemical synthesis of aromatic aldehydes, ketones, and quinones using ceric methanesulfonate. *J. Org. Chem.* **1988,** *54*.

84. Zurilla, R. W.; Sen, R. K.; Yeager, E., The kinetics of the oxygen reduction reaction on gold in alkaline solution. *J. Electrochem. Soc.* **1978,** *125*, 7.

85. Wu, M.; Jing, Y.; Wong, A. A.; Fell, E. M.; Jin, S.; Tang, Z.; Gordon, R. G.; Aziz, M. J., Extremely stable anthraquinone negolytes synthesized from common precursors. *Chem* **2020,** *6*, 1432.

86. Wei, X. L.; Pan, W. X.; Duan, W. T.; Hollas, A.; Yang, Z.; Li, B.; Nie, Z. M.; Liu, J.; Reed, D.; Wang, W.; Sprenkle, V., Materials and systems for organic redox flow batteries: status and challenges. *ACS Energy Lett.* **2017,** *2* (9), 2187-2204.

87. Brushett, F. R.; Aziz, M. J.; Rodby, K. E., On lifetime and cost of redox-active organics for aqueous flow batteries. *ACS Energy Lett.* **2020,** *5*, 879-884.

88. Gerhardt, M. R.; Tong, L.; Gomez-Bombarelli, R.; Chen, Q.; Marshak, M. P.; Galvin, C. J.; Aspuru-Guzik, A.; Gordon, R. G.; Aziz, M. J., Anthraquinone derivatives in aqueous flow batteries. *Adv. Energy Mater.* **2017,** *7* (8), 1601488.

89. Cao, J. Y.; Tao, M.; Chen, H. P.; Xu, J.; Chen, Z. D., A highly reversible anthraquinone-based anolyte for alkaline aqueous redox flow batteries. *J. Power Sources* **2018,** *386*, 40-46.

90. Tong, L.; Goulet, M.-A.; Tabor, D. P.; Kerr, E. F.; De Porcellinis, D.; Fell, E. M.; Aspuru-Guzik, A.; Gordon, R. G.; Aziz, M. J., Molecular engineering of an alkaline naphthoquinone flow battery. *ACS Energy Lett.* **2019,** *4* (8), 1880-1887.

91. Jing, Y.; Wu, M.; Wong, A. A.; Fell, E. M.; Jin, S.; Pollack, D. A.; Kerr, E. F.; Gordon, R. G.; Aziz, M. J., In situ electrosynthesis of anthraquinone electrolytes in aqueous flow batteries. *Green Chem.* **2020,** *22* (18), 6084-6092.

92. Liu, T. B.; Wei, X. L.; Nie, Z. M.; Sprenkle, V.; Wang, W., A total organic aqueous redox flow battery employing a low cost and sustainable methyl viologen anolyte and 4-HO-TEMPO catholyte. *Adv. Energy Mater.* **2015,** *6* (3), 1501449.

93. Janoschka, T.; Morgenstern, S.; Hiller, H.; Friebe, C.; Wolkersdorfer, K.; Haupler, B.; Hager, M. D.; Schubert, U. S., Synthesis and characterization of TEMPO- and viologen-polymers for water-based redox-flow batteries. *Polym. Chem.* **2015,** *6* (45), 7801-7811.

94. Luo, J.; Hu, B.; Debruler, C.; Liu, T. L., A pi-conjugation extended viologen as a two-electron storage anolyte for total organic aqueous redox flow batteries. *Angew. Chem. Int. Ed.* **2018,** *57* (1), 231-235.

95. DeBruler, C.; Hu, B.; Moss, J.; Luo, J.; Liu, T. L., A sulfonate-functionalized viologen enabling neutral cation exchange, aqueous organic redox flow batteries toward renewable energy storage. *ACS Energy Lett.* **2018,** *3* (3), 663-668.

96. Liu, W.; Liu, Y.; Zhang, H.; Xie, C.; Shi, L.; Zhou, Y. G.; Li, X., A highly

stable neutral viologen/bromine aqueous flow battery with high energy and power density. *Chem. Commun.* **2019,** *55* (33), 4801-4804.

97. Ohira, A.; Funaki, T.; Ishida, E.; Kim, J.-D.; Sato, Y., Redox-flow battery operating in neutral and acidic environments with multielectron-transfer-type viologen molecular assembly. *ACS Appl. Energy Mater.* **2020,** *3* (5), 4377-4383.

98. Jin, S.; Fell, E. M.; Vina-Lopez, L.; Jing, Y.; Michalak, P. W.; Gordon, R. G.; Aziz, M. J., Near neutral ph redox flow battery with low permeability and long‐lifetime phosphonated viologen active species. *Adv. Energy Mater.* **2020,** *10* (20).

99. Winsberg, J.; Stolze, C.; Muench, S.; Liedl, F.; Hager, M. D.; Schubert, U. S., TEMPO/phenazine combi-molecule: A redox-active material for symmetric aqueous redox-flow batteries. *ACS Energy Lett.* **2016,** *1* (5), 976-980.

100. Wang, C.; Li, X.; Yu, B.; Wang, Y.; Yang, Z.; Wang, H.; Lin, H.; Ma, J.; Li, G.; Jin, Z., molecular design of fused-ring phenazine derivatives for long-cycling alkaline redox flow batteries. *ACS Energy Lett.* **2020,** *5* (2), 411-417.

101. Pang, S.; Wang, X.; Wang, P.; Ji, Y., Biomimetic amino acid functionalized phenazine flow batteries with long lifetime at near-neutral pH. *Angew. Chem. Int. Ed.* **2021,** *60*, 5289 –5298

102. Janoschka, T.; Martin, N.; Martin, U.; Friebe, C.; Morgenstern, S.; Hiller, H.; Hager, M. D.; Schubert, U. S., An aqueous, polymer-based redox-flow battery using non-corrosive, safe, and low-cost materials. *Nature* **2015,** *527* (7576), 78-81.

103. Winsberg, J.; Janoschka, T.; Morgenstern, S.; Hagemann, T.; Muench, S.; Hauffman, G.; Gohy, J. F.; Hager, M. D.; Schubert, U. S., Poly(TEMPO)/zinc hybrid-flow battery: a novel, "green," high voltage, and safe energy storage system. *Adv. Mater.* **2016,** *28* (11), 2238-43.

104. Chang, Z.; Henkensmeier, D.; Chen, R., One-step cationic grafting of 4-hydroxy-tempo and its application in a hybrid redox flow battery with a crosslinked pbi membrane. *ChemSusChem* **2017,** *10* (16), 3193-3197.

105. Winsberg, J.; Stolze, C.; Schwenke, A.; Muench, S.; Hager, M. D.; Schubert, U. S., Aqueous 2,2,6,6-Tetramethylpiperidine-N-oxyl catholytes for a high-capacity and high current density oxygen-insensitive hybrid-flow battery. *ACS Energy Lett.* **2017,** *2* (2), 411-416.

106. Liu, Y. H.; Goulet, M. A.; Tong, L. C.; Liu, Y. Z.; Ji, Y. L.; Wu, L.; Gordon, R. G.; Aziz, M. J.; Yang, Z. J.; Xu, T. W., A long-lifetime all-organic aqueous flow battery utilizing TMAP-TEMPO radical. *Chem* **2019,** *5* (7), 1861-1870.

107. Hu, B.; Tang, Y.; Luo, J.; Grove, G.; Guo, Y.; Liu, T. L., Improved radical stability of viologen anolytes in aqueous organic redox flow batteries. *Chem. Commun.* **2018,** *54* (50), 6871-6874.

108. Gharagheizi, F., Determination of diffusion coefficient of organic compounds in water using a simple molecular-based method. *Ind. Eng. Chem. Res.* **2012,** *51* (6), 2797-2803.

109. Chen, Q.; Gerhardt, M. R.; Aziz, M. J., Dissection of the voltage losses of an acidic quinone redox flow battery. *J. Electrochem. Soc.* **2017,** *164* (6), A1126-A1132.

110. Wong, A. A.; Aziz, M. J., Method for comparing porous carbon electrode performance in redox flow batteries. *J. Electrochem. Soc* **2020,** *167* (11), 110542.

111. Chen, Q.; Eisenach, L.; Aziz, M. J., Cycling Analysis of a Quinone-Bromide Redox Flow Battery. *J. Electrochem. Soc.* **2016,** *163* (1), A5057-A5063.

112. Bien, H.-S.; Stawitz, J.; Wunderlich, K., Anthraquinone dyes and intermediates. In *Ullmann's Encyclopedia of Industrial Chemistry*, **2000**.

113. Mattioda, G.; Christidis, Y., Glyoxylic acid. In *Ullmann's Encyclopedia of Industrial Chemistry*, **2000**.

114. Ulaganathan, M.; Aravindan, V.; Yan, Q.; Madhavi, S.; Skyllas-Kazacos, M.; Lim, T. M., Recent advancements in all-vanadium redox flow batteries. *Adv. Mater. Interfaces* **2016,** *3* (1), 1500309.

115. Winsberg, J.; Hagemann, T.; Janoschka, T.; Hager, M. D.; Schubert, U. S., Redox-flow batteries: from metals to organic redox-active materials. *Angew. Chem. Int. Ed.* **2017,** *56* (3), 686-711.

116. Wang, C. X.; Yang, Z.; Wang, Y. R.; Zhao, P. Y.; Yan, W.; Zhu, G. Y.; Ma, L. B.; Yu, B.; Wang, L.; Li, G. G.; Liu, J.; Jin, Z., High-performance alkaline organic redox flow batteries based on 2-hydroxy-3-carboxy-1,4-naphthoquinone. *ACS Energy Lett.* **2018,** *3* (10), 2404-2409.

117. Liu, Y.; Li, Y.; Zuo, P.; Chen, Q.; Tang, G.; Sun, P.; Yang, Z.; Xu, T., Screening viologen derivatives for neutral aqueous organic redox flow batteries. *ChemSusChem* **2020**, *13*, 2245 –2249.

118. Zhao, Z.; Zhang, B.; Schrage, B. R.; Ziegler, C. J.; Boika, A., Investigations Into Aqueous Redox Flow Batteries Based on Ferrocene Bisulfonate. *ACS Appl. Energy Mater.* **2020,** *3* (10), 10270-10277.

119. Li, Y.; Xu, Z.; Liu, Y.; Jin, S.; Fell, E. M.; Wang, B.; Gordon, R. G.; Aziz, M. J.; Yang, Z.; Xu, T., Functioning water-insoluble ferrocenes for aqueous organic flow battery via host-guest inclusion. *ChemSusChem* **2020**, *14*, 745-752.

120. Wang, C.; Yu, B.; Liu, Y.; Wang, H.; Zhang, Z.; Xie, C.; Li, X.; Zhang, H.; Jin, Z., N-alkyl-carboxylate-functionalized anthraquinone for long-cycling aqueous redox flow batteries. *Energy Storage Mater.* **2021,** *36*, 417-426.

121. Liang, S.; Subrahmanyam, A. V.; Khadem, M.; Zhao, Y.; Adronov, A., Selective dispersion of single-walled carbon nanotubes with electron-rich fluorene-based copolymers. *RSC Adv.* **2016,** *6* (31), 25733-25740.

122. Bard, A. J.; Faulkner, L. R., *Electrochemical methods: fundamentals and applications*. Wiley: New York, **2001**.

123. Hu, B.; Luo, J.; Hu, M.; Yuan, B.; Liu, T. L., A pH-neutral, metal-free aqueous organic redox flow battery employing an ammonium anthraquinone anolyte. *Angew. Chem. Int. Ed.* **2019,** *58* (46), 16629-16636.

124. Petit, Y. K.; Mourad, E.; Prehal, C.; Leypold, C.; Windischbacher, A.; Mijailovic, D.; Slugovc, C.; Borisov, S. M.; Zojer, E.; Brutti, S.; Fontaine, O.; Freunberger, S. A., Mechanism of mediated alkali peroxide oxidation and triplet versus singlet oxygen formation. *Nat. Chem.* **2021**, *13*, 465-471.

125. McCann, G. M.; McDonnell, C. M.; Magris, L.; More O'Ferrall, R. A., Enol–keto tautomerism of 9-anthrol and hydrolysis of its methyl ether. *J. Chem. Soc., Perkin Trans. 2*, **2002,** (4), 784-795.